Investigation of Transpiration Cooling Film Protection for Gas Turbine Engine Combustion Liner Application

Mathieu Hinse

Thesis submitted to the University of Ottawa
in partial fulfilment of the requirements for the degree of

MASTER OF APPLIED SCIENCE

in Mechanical Engineering

Ottawa-Carleton Institute for Mechanical and Aerospace Engineering
University of Ottawa
Ottawa, Canada

July 2021

© Mathieu Hinse, Ottawa, Canada, 2021

Abstract

Transpiration cooling as potential replacement of multi-hole effusion cooling for gas turbine engines combustion liner application is investigated by comparing their cooling film effectiveness based on the mass transfer analogy (CFE_M). Pressure sensitive paint was used to measure CFE_M over PM surfaces which was found to be on average 40% higher than multi-hole effusion cooling. High porosity PM with low resistance to flow movement were found to offer uneven distribution of exiting coolant, with large amounts leaving the trailing edge, leading to lopsided CFE_M. Design of anisotropic PM based on PM properties (porosity, permeability, and inertia coefficient) were investigated using numerical models to obtain more uniform CFE_M. Heat transfer analysis of different PM showed that anisotropic samples offered better thermal protection over isotropic PM for the same porosity. Comparison between cooling film effectiveness obtained from temperatures CFE_T against CFE_M revealed large differences in the predicted protection. This is attributed to the assumptions made to apply CFE_M, nonetheless, CFE_M remains a good proxy to study and improve transpiration cooling. A method for creating a CAD model of designed PM is proposed based on critical characteristics of transpiration cooling for future use in 3D printing manufacturing.

Acknowledgements

I want to thank Bertrand Jodoin, my thesis supervisor, for his guidance during these past two years. You were always positive about the project and during the weekly meetings. It was a pleasure to work with you.

I want to thank Zekai Hong, senior research officer at the National Research Council of Canada, for your involvement in the project. You always pushed me to improve as a professional researcher and showed you cared about the project and my success.

I want to thank Patrick Richer, assistant professor, for giving me the opportunity to pursue this project. The suggestions and ideas you brought were always top notch and guided me in the right directions for the project.

I want to give great thanks to my girlfriend Dominique, who always supported and cared for me throughout this journey, especially as I am writing this thesis. I was not able to spend as much time with you as I would have liked, and I am ever grateful for your understanding and patience.

I want to thank my parents, my brothers, and my sisters for their support in pursuing my master's degree. Your words of encouragement helped me greatly in finishing my degree.

I want to thank everyone in the lab for their help. You were always quick in answering my questions or lending me a hand whenever I needed help, even though my research is very different than yours. I have enjoyed the time we have worked together.

Finally, I want to thank my friends, especially those with whom I shared the difficulties of a master's degree: Marchi, Frank, and Scrote. Even though we were not able to spend much time in person due to the extraordinary circumstances of the pandemic, we were able to relax playing video games or speaking to each other online.

Table of Contents

List of Figures

List of Tables

Nomenclature

Latin Letters:

A	Area $[m^2]$	$\dot{m}$	Mass flow rate $\left[\frac{kg}{s}\right]$
a_{sf}	Specific surface area $[m^{-1}]$	Nu	Nusselt number
c	Specific heat capacity $\left[\frac{J}{kg \cdot K}\right]$	P	Pressure $[Pa]$
d	Diameter	Pr	Prandtl number
f	Inertia coefficient	R	Ideal gas constant
g	Gravitational force	Re	Reynolds number
h	Convective heat transfer coefficient $\left[\frac{W}{m^2 \cdot K}\right]$	St	Stanton number
h_s	Enthalpy	T	Temperature $[K]$
K	Permeability $[m^2]$	t	Time $[s]$
k	Conductivity coefficient $\left[\frac{W}{m \cdot K}\right]$	V	Fluid velocity $\left[\frac{m}{s}\right]$
M	Mach number	X	Mole fraction

Greek Letters:

α_{CFE}	Minimum and maximum CFE ratio	η'	Thermal effectiveness
ϵ	Porosity	ρ	Density $\left[\frac{kg}{m^3}\right]$
μ	Dynamic viscosity $\left[\frac{kg}{m \cdot s}\right]$	σ	Surface porosity
η	Cooling film effectiveness	τ_{CFE}	CFE uniformity ratio

Subscripts:

c	Coolant	O	Zero-blowing condition
ci	Coolant inlet	O_2	Oxygen
ce	Coolant exit	p	Pore
DH	In a pipe/Hydraulic diameter	R	Resistance
f	Fluid or fiber or inertia coefficient (depending on context)	s	Solid
fe	Fluid effective	se	Solid effective
$film$	Cooling film in contact with the porous media	sf	Solid-fluid
FS	Full surface	t	Turbulent
ge	Effective hot gas	T	Temperature
HG	Hot gas	TE	Trailing edge
i	Interfacial	v	Volumetric
K	Permeability	w	Porous media wall
LE	Leading edge	ϵ	Porosity
M	Mass transfer analogy		

Glossary

AM	Additive Manufacturing	OPR	Overall Pressure Ratio
BR	Blowing Ratio	PM	Porous Media
CAD	Computer Aided Design	PPI	Pores Per Inch
CFE	Cooling Film Effectiveness	PSP	Pressure Sensitive Paint
FVM	Finite-Volume Method	SLMS	Selective Laser Metal Sintering
HGP	Hot Gas Path	TIT	Turbine Inlet Temperature
LNTE	Local Non-Thermal Equilibrium	UDF	User-Defined Function
NRC	National Research Council of Canada		

1 Introduction

1.1 Background

The environmental crisis currently facing humanity is likely to be one of the defining features of the 21st century. The road to changing the course of history lies in the reduction of greenhouse gas emissions such as methane and carbon dioxide, to name the main culprits. Most of the legwork will come from transitioning our energy sources from coal, gasoline, and natural gas to "cleaner" energy sources such as: wind, hydroelectric, nuclear, solar, hydrogen fuel cells and fission, if science advances enough. Of course, virtually all industries and sectors, such as our modes of transportation, will also have to transition to electricity. Electric cars are already commercially available and readily accessible, and it remains a question of time before a full transition occurs. These transitions are inevitable, but the rate at which they do is crucial. Ultimately, the speed at which we transcend into a sustainable future fall in the hands of societies around the world to put pressure on the leaders they elect, or inherit.

One transition which is likely to take much more time is in the aviation sector, where powerful air-breathing gas turbine engines run on jet fuel (such as Kerosene) to produce the thrust required to fly. Kerosene is considered to have a relatively high energy density, with a specific energy of $43\frac{MJ}{kg}$ [1]. In comparison, the best batteries currently available have a specific energy of approximately $260\frac{Wh}{kg}$ or $0.94\frac{MJ}{kg}$, far lower than kerosene [2]. Installing more batteries to compensate for the energy gap increases the weight of the plane, thus requiring even more thrust to be generated to lift the plane. Practically, this imposes a limit on the maximum size an electric plane could reach. Consequently, the best way the aviation sector can currently reduce its greenhouse gas emissions is by increasing the efficiency of the planes. Furthermore, from an economic standpoint, the increase in efficiency decreases the specific fuel consumption, and therefore the operational cost of the plane.

Raising overall pressure ratios (OPR) and turbine inlet temperatures (TIT) enable modern gas turbine engines to achieve thermodynamic efficiency gains, thus reducing specific fuel consumptions. However, cooling gas turbine's hot gas path (HGP) components becomes particularly challenging due to high OPR and high thermal loads caused by elevated TIT.

Effective cooling strategies are therefore essential to protect HGP components from premature thermal damages.

Multi-hole effusion cooling is widely adopted to protect the gas turbine combustion liner. A portion of the compressor discharge air is blown through spanwise slits or rows of holes, forming a protective cooling film over the inner part of the combustion chamber liner [3]–[8], as shown in Figure 1.1. Although effusion cooling is a simple and reliable technique, it is not ideal as it does not provide uniform cooling film protection and is also limited by the amount of coolant that can be introduced: excessive coolant flow rates and velocities through the holes can produce lift-off of the coolant jets [9], reducing overall cooling film protection.

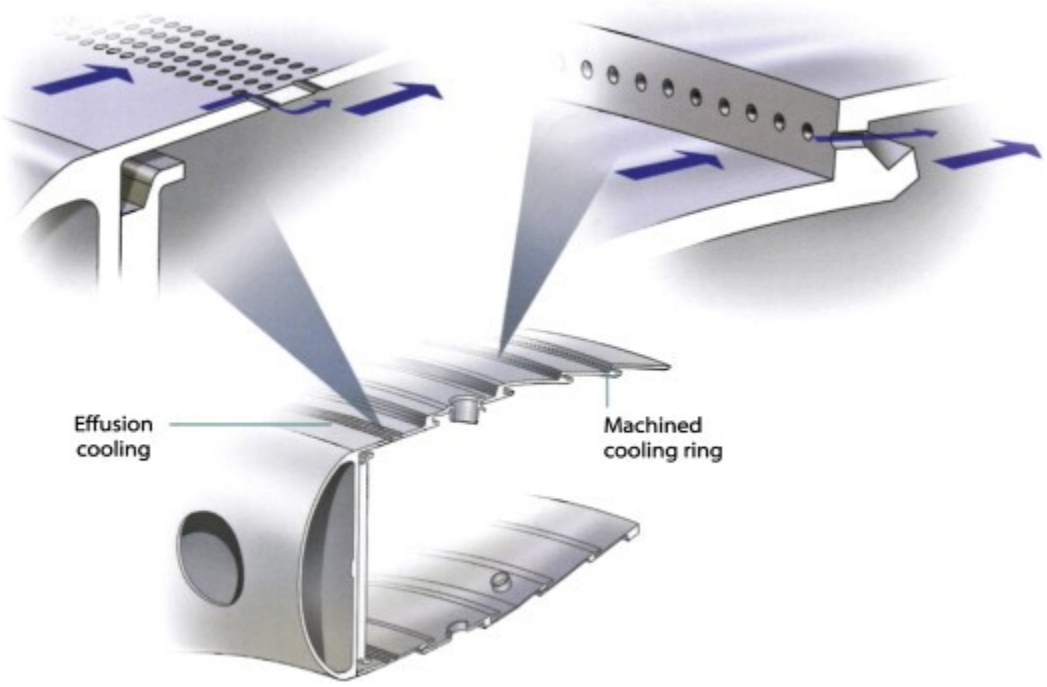

Figure 1.1 Schematic of effusion cooling in gas turbine combustors [10]**.**[1]

The ideal scenario is a method that would provide a constant and uniform cooling film. Transpiration cooling, where cooling is achieved by passing a fluid through a porous medium and creating a protective film over it when exiting, could potentially offer this type of protection. A schematic is presented in Figure 1.2.

[1] Reprinted from Elsevier Books, Second Edition , C. Soares, "Gas Turbines – A handbook of Air, Land and Sea Applications", 173-254, Copyright 2015, with permission from Elsevier.

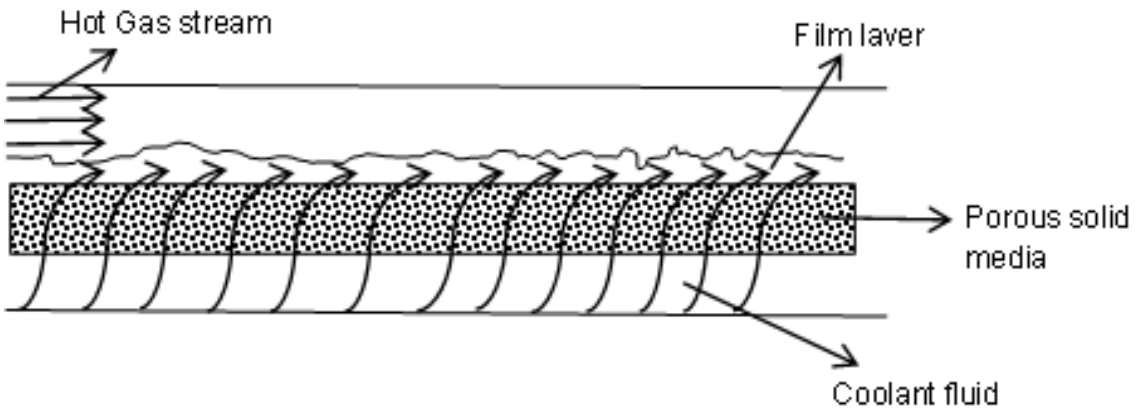

Figure 1.2 Schematic of transpiration cooling [11]. [2]

This work aims to study the potential benefits of transpiration cooling using porous media (PM) and earlier preliminary experimental data to validate a numerical model. The experimental approach is part of earlier work carried out by Mr. Kivanc Yildiz as part of an undergraduate Thesis submitted in April 2019 in which I assisted for some of the experimental setup and data acquisition [12]. It is summarized in Chapter 4 due to its importance for the development and validation of the numerical model. The experiments involved visualization of the cooling film over the PM surface: pressure sensitive paint (PSP) was applied to determine cooling film effectiveness of transpiration cooling by using the heat/mass transfer analogy (CFE_M). The PSP responds to the partial pressure of molecular oxygen over the painted surface, modifying its fluorescence intensity upon ultraviolet (UV) excitation. Once calibrated, the change in fluorescence intensity from PSP allowed determining the main stream air fraction being replaced by nitrogen, which acted as a proxy for cooling air passing through the PM and forming a protective film over its surface.

The numerical model developed in this work uses a commercially available CFD tool (Ansys Fluent) to simulate a 2D representation of the experimental set-up, with the aim of gaining insights into transpiration cooling by replicating Kivanc's experimental results. PM are then designed by profiling the porosity, permeability, and inertia coefficient using a square root function to achieve ideal CFE_M, i.e., an even and uniform concentration of coolant over

[2] Reprinted by permission from Springer Nature: Springer Nature, *Heat and Mass Transfer,* [11], Copyright © 2018 Springer Nature. All rights reserved.

the whole PM surface. Numerical heat transfer analysis of these PM is later performed to compare the CFE_M to the cooling film effectiveness obtained from temperatures (CFE_T).

Finally, a method for creating CAD models of profiled PM for manufacturing using 3D printing is made based on important characteristics such as: structural integrity, high specific surface area, limited possibility of fouling, repeatability, and ease of manufacturing. This work was performed in collaboration with the Gas Turbine Laboratory of the National Research Council of Canada (NRC), Ottawa, Ontario.

1.2 Research Aims

Investigation and observation of the cooling film in transpiration cooling has not been widely reported. The aim of this thesis was to gain fundamental insight of the cooling film over PM and investigate possible improvements. The influence of PM properties, i.e., porosity, permeability, and inertia coefficient on the CFE_M, was investigated to ascertain if designed PM can improve CFE_M over non-designed samples.

1.3 Thesis Content

The following thesis is arranged into ten chapters. The content of each chapter is summarized in this subsection.

Chapter 1 is an introduction on the subject matter of this thesis and presents the motivations for the work covered in subsequent chapters.

Chapter 2 reviews the literature for previous and relevant work surrounding the transpiration cooling method and the use of PM.

Chapter 3 establishes the research objectives undertaken to achieve the research aims.

Chapter 4 contains the experimental work by Mr.Kivanc Yildiz in his undergraduate thesis on the CFE_M of aluminum metal foams performed at the NRC [12]. Results are compared to multi-hole effusion cooling from the literature which demonstrated the superior protection of the

transpiration cooling method. It is included due to its importance in developing the numerical model used for the rest of the present thesis.

Chapter 5 presents the numerical setup using Ansys Fluent to simulate the flow of a fluid through a channel and a PM. The chapter includes details on the domain, governing equations, discretization methods, turbulence model, and mesh analysis.

Chapter 6 compares the results between the numerical simulations and experiments. A sensitivity analysis of PM properties i.e., permeability and inertia coefficient is performed, indicating a relation between the CFE_M and the aforementioned properties.

Chapter 7 uses the findings on the effects of PM properties on the CFE_M to design samples which offer uniform film protection. More specifically, these properties are profiled using a square root function to redistribute coolant exiting the PM.

Chapter 8 establishes the numerical heat transfer model and validates it based on experimental data found in the literature. Adaptation of this model to the problems and conditions of this project is outlined, allowing comparison between CFE_T to CFE_M obtained in prior chapters.

Chapter 9 presents a CAD model created in SolidWorks of a profiled PM for use in additive manufacturing based on important design criteria in transpiration cooling.

Chapter 10 concludes the findings of this thesis, followed by recommendations on future work that should be performed to further the development and understanding of transpiration cooling. A list of references and the appendices follow this chapter.

2 Literature Review

2.1 Gas Turbine Engine

Gas turbine engines are a type of internal combustion engine where chemical energy from the combustion of fuel is converted into kinetic energy to rotate a shaft and/or produce thrust from the exhaust gases. The shaft can be attached to a mechanism and make use of this energy, for example: turning an electric motor (turboshaft), powering helicopter blades (turboprop), powering a giant fan for propulsion (turbofan).

The theoretical efficiency of gas turbine engines is determined by the ideal Brayton cycle which is shown on a T-s diagram in Figure 2.1 for an open cycle. Evolution from 1-2 is the compression of the air by the compressor, 2-3 the combustion of fuel in the combustion chamber, and 3-4 the extraction of work through the turbine. The efficiency is calculated using Eq. (2-1) [13].

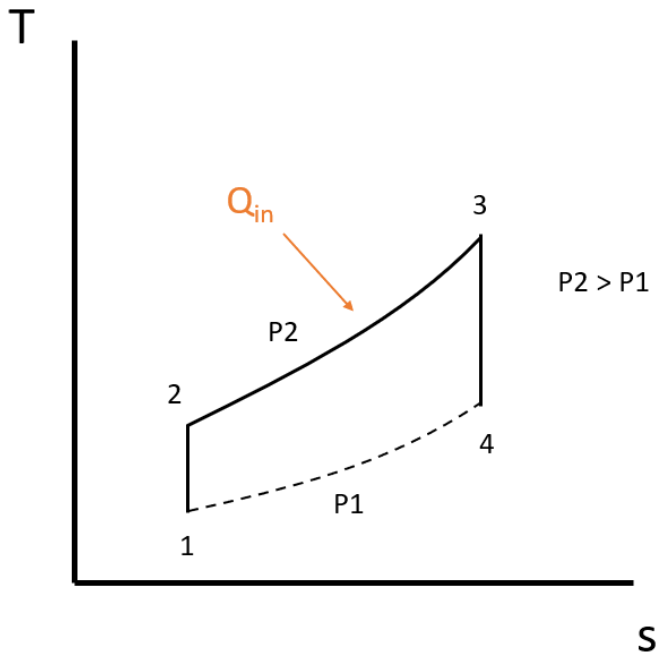

Figure 2.1 Temperature-entropy diagram of the Brayton cycle in an open cycle.

$$\eta_{th} = 1 - \frac{1}{\left(\frac{P_2}{P_1}^{\frac{(\gamma-1)}{\gamma}}\right)} = \frac{W_{net}}{Q_{in}} \quad \textbf{(2-1)}$$

where η_{th} is the theoretical thermodynamic efficiency of the engine, P is pressure, γ is the specific heat ratio of the air, W_{net} the net work produced by the engine, and Q_{in} the heat energy added to the system from combustion. Therefore, the theoretical efficiency is determined by the OPR of the engine.

The amount of work extracted by the turbine can be calculated by [13]:

$$W_{turbine} = Cp(T_3 - T_4) \quad \textbf{(2-2)}$$

where $W_{turbine}$ is the work extracted by the turbine and Cp the specific heat of the gas. Maximizing the TIT of T_3 allows the maximum amount of work to be extracted. However, this leads to high thermal loads on components in the HGP such as the combustion liner and turbine blades, thereby requiring active cooling.

The net work extracted by the engine equals the work produced by the turbine minus the work used by the compressor ($W_{compressor}$) [13]:

$$W_{net} = W_{turbine} - W_{compressor} \quad \textbf{(2-3)}$$

Therefore, by improving the cooling method used, lower amounts of coolant may be used to protect the liner resulting in higher T_3 temperatures due to reduced dilution between hot gas and coolant. Reduction in coolant usage lowers the amount of work required by the compressor, leading to higher efficiency.

2.2 Gas Turbine Engine Cooling

In this section, an overview of the evolution of cooling techniques of gas turbine engines HGP components is presented. Such examples of HGP components include, but are not limited to: high-pressure turbine, combustor, heat exchangers, casings, bores, compressor and turbine disks, bearings and gears, exhaust nozzles, de-icing, and fire suppression. A schematic of these components are presented in Figure 2.2 [14]. Most of the research has gone into cooling of high-pressure turbines, summarized in [14], and combustors, the latter being of concern for the present thesis.

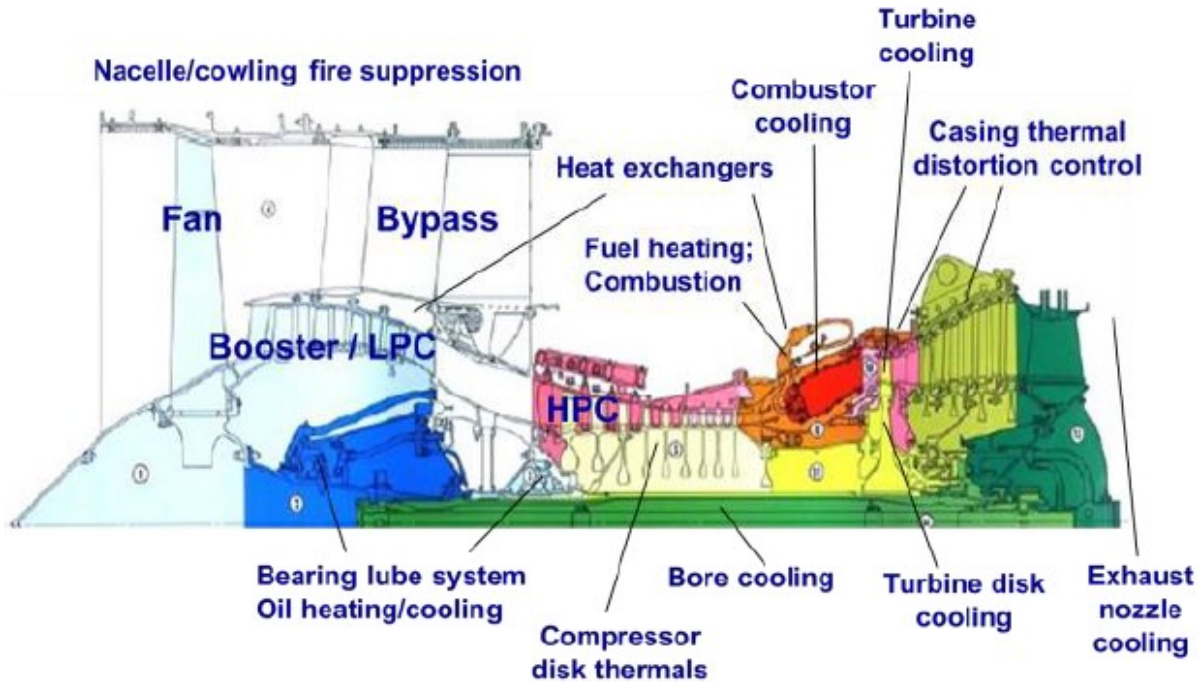

Figure 2.2 Cross-section of Gas turbine engine components [14]**.**

The motivations for advancements in cooling technologies of gas turbine engines HGP components stem from the thermodynamic Brayton cycle which describes the workings of airbreathing jet engines and was described in the previous subsection.

Advances in cooling and accompanying manufacturing methods have led to increases in thermal cooling film effectiveness (CFE_T) from 0.1 to 0.7 over the past 50 years or so [14]. The CFE_T defined in this case as the ability of the coolant to bring the temperature of a component closer to the cooling fluid temperature versus the hot gas temperature [14], more on the CFE_T in subsection 2.2.2. These increases in CFE_T over time have been achieved in

conjunction to reductions in coolant usages by up to 50%, even though TIT have also increased [14], as presented in Figure 2.3. This figure is quite outdated now but does show the improvements made since the 1940's to 2000.

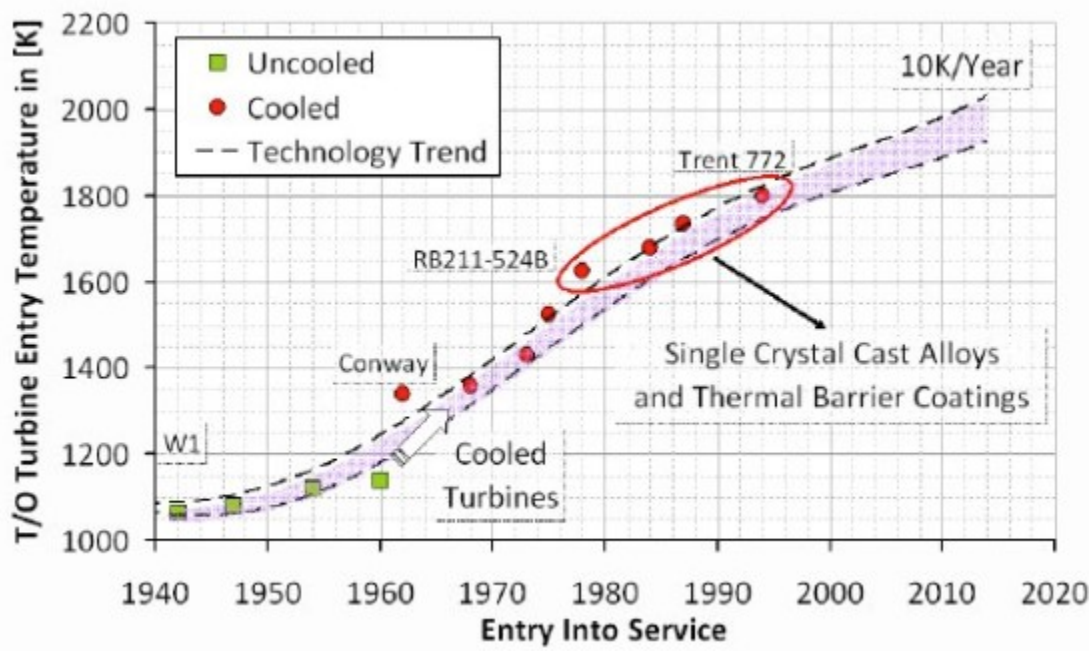

Figure 2.3 Evolution of turbine inlet temperature over time with introduction of new technologies [15]**.**

2.2.1 Main cooling methods

Current cooling technologies employed in gas turbine engines use a form of film cooling, consisting of injecting a cool fluid over the surface of the component to be protected, creating a protective film, and reducing heat transfer from hot gas stream. Several methods exist to achieve film cooling, with varying protection and complexity: the main ones are presented in Figure 2.4.

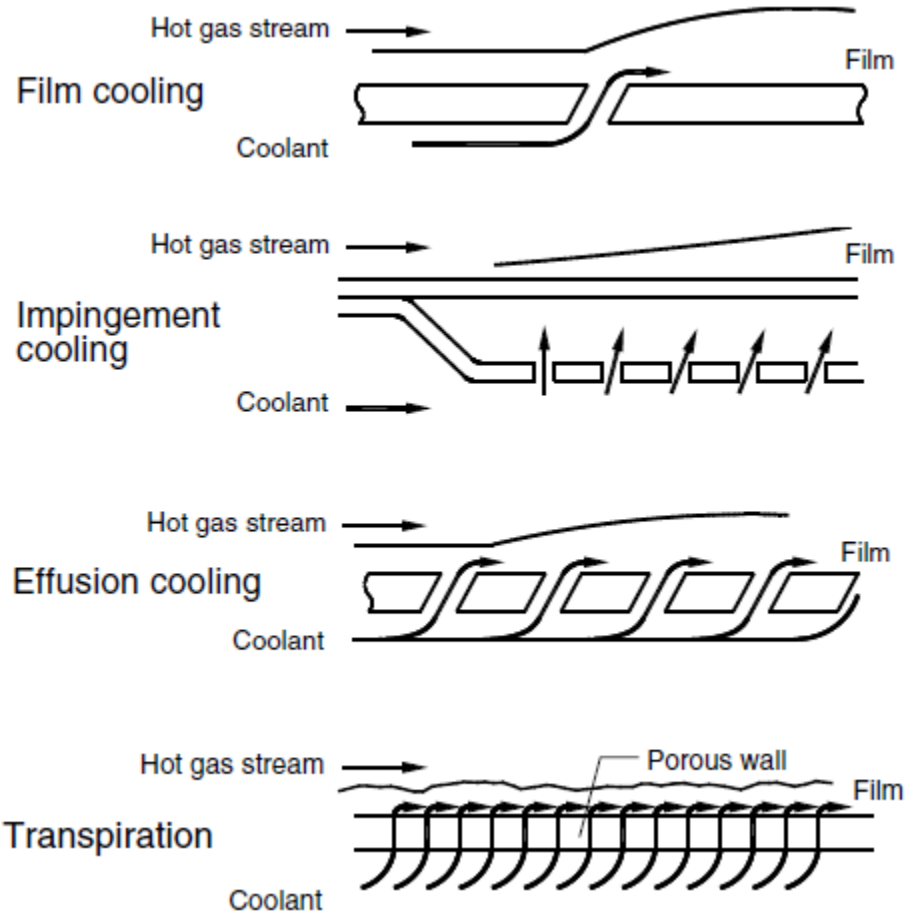

Figure 2.4 Main cooling methods for gas turbine engines [16].[3]

Film cooling is the simplest method, utilizing large slits to introduce coolant thus requiring large amount of coolant to achieve adequate cooling. Impingement cooling blows high velocity jets of coolant on the back side of a surface, creating high heat transfer, and cooling the wall in the process. It, however, does not make use of film protection on the wall surface in contact with the hot gas stream. Effusion cooling is the main cooling scheme used in modern gas turbines. Cooling is achieved by use of a perforated wall which distributes coolant more evenly than basic film cooling, thus making better use of coolant. Multiple variations were developed over the years such as Transply® and Lamilloy® in the eighties, and later Poroform®, see Figure 2.5. More information on such techniques can be found in [16].

[3] Reprinted from Journal of Applied Thermal Engineering, Vol. 27, Cerri, G, Giovannelli, A, Battisti, L, Fedrizzi, R, "Advances in effusive cooling techniques of gas turbines", Pg. 692-698., Copyright 2007, with permission from Elsevier.

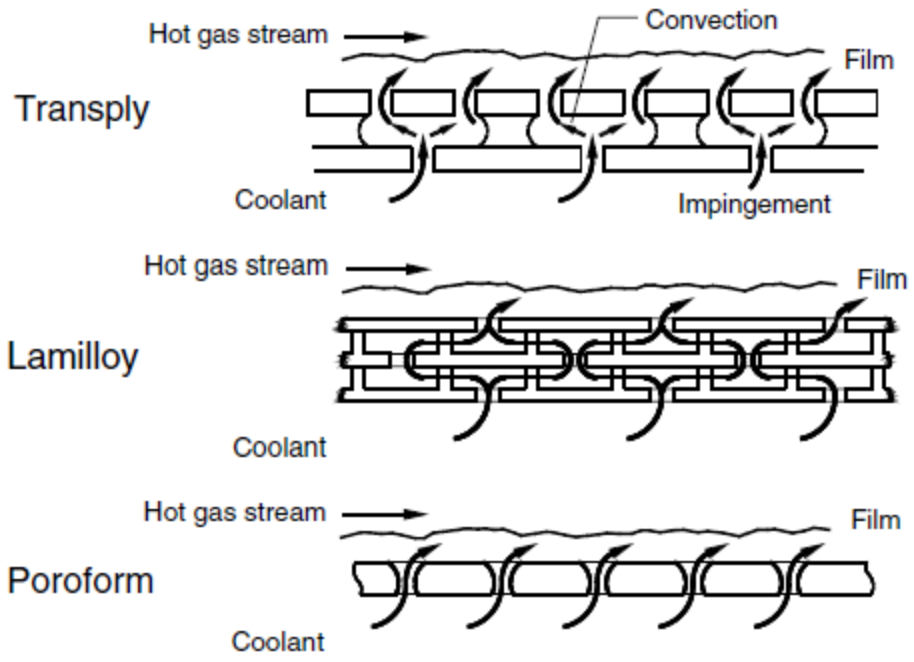

Figure 2.5 Variations in effusion cooling methods [16].[4]

Finally, transpiration cooling makes use of a PM to create a uniform protective film on the surface and offers large heat transfer inside the PM. More details on transpiration cooling are presented in the following subsections.

Cooling methods in gas turbine engines have typically been limited by the following factors: pressure losses, material temperatures, component stresses, geometry and volume, aerodynamics, fouling, and coolant conditions [14]. These engineering problems have determined which cooling methods were used historically. As more problems were solved, the complexity of methods utilized increased, from film cooling to effusion cooling, and transpiration cooling projected as the next leap forward. Component stresses and manufacturing methods have been the major holdbacks of transpiration cooling, as discussed further in subsection 2.3.4.

[4] Reprinted from Journal of Applied Thermal Engineering, Vol. 27, Cerri, G, Giovannelli, A, Battisti, L, Fedrizzi, R, "Advances in effusive cooling techniques of gas turbines", Pg. 692-698., Copyright 2007, with permission from Elsevier.

2.2.2 Film cooling parameters

Various methods are used to quantify the effectiveness of film cooling techniques. Important ones are presented here. First, to enable comparison between different experiments with varied channel and cooling surface dimensions, and cooling methods, the blowing ratio (BR), or sometimes called injection ratio, is used. It is defined as the ratio of coolant mass flux to hot gas mass flux, such as Eq. (2-4).

$$\mathrm{BR} = \frac{\rho_c V_c}{\rho_{HG} V_{HG}} \tag{2-4}$$

where ρ is density, V is velocity, subscript c is the coolant and HG is the hot gas.

CFE_T denoted by variable η, defines the effectiveness of the coolant to bring the wall temperature closer to the coolant inlet temperature. A value of one indicates the highest possible cooling as the wall temperature equals the inlet coolant temperature and a value of zero indicate the poorest possible cooling as the wall temperature equals the hot gas temperature. CFE_T is calculated by Eq. (2-5) [14], [17].

$$\eta = \frac{T_{HG} - T_w}{T_{HG} - T_{ci}} \tag{2-5}$$

where T is the temperature, subscript w the surface PM wall and ci the inlet coolant. The CFE_M, which is the CFE measured from mass analogy is presented in chapter 4. The thermal effectiveness η′, defines the effectiveness at which the coolants heat capacity is utilized. A value of one indicates the coolant has absorbed the maximum amount of heat it can as the wall and exiting coolant have the same temperature. A value closer to zero indicates the coolant was unable to absorb much heat as the exiting coolant has a much lower temperature than the wall. The thermal effectiveness is as presented in Eq. (2-6) [17].

$$\eta' = \frac{T_{ce} - T_{ci}}{T_w - T_{ci}} \tag{2-6}$$

where subscript ce denotes the coolant exiting the PM.

2.3 Transpiration Cooling

Transpiration cooling is the process of passing a fluid through a PM to create a protective film on the surface, reducing convective heat transfer of a passing warmer gas, while simultaneously cooling the interior structure. The reduction in convective heat transfer from the hot gas occurs due to the thermal blowing effect when coolant is injected in the boundary layer. See Figure 1.1 or Figure 2.4 for schematics of transpiration cooling.

A background on some of the first studies on transpiration cooling is presented first; followed by the mechanisms of transpiration cooling; a review of recent numerical, experimental, and analytical studies; additive manufacturing (AM) as the future manufacturing method of PM for transpiration cooling; and finally, PM characterization and general relationships.

2.3.1 Early Development

Transpiration cooling is not a new concept, with research going as far back as the 1950's, such as Eckert et Al. [18] (1954) which showed transpiration cooling to be more effective than film cooling methods like effusion cooling. Most early research into transpiration cooling appeared to be motivated by the cold war and the ensuing space race, as supported by the following papers: Luikov et Al. (1962) in the late USSR [19], investigated the reduction in convective coefficient between a zero-blowing condition of coolant to transpiration cooling of capillary-porous bodies. Librizzi et Al. (1964) [20] experimentally investigated transpiration cooling of a turbulent boundary layer in an axisymmetric nozzle, showing a decrease in heat transfer with an increase in mass injection, helium being more effective for the same mass flow rate than nitrogen. Walton et Al. (1964) [21] performed free-flight investigations of subliming ablators and transpiration cooling at hypersonic velocity, evidently for atmosphere re-entry of spacecrafts.

Research on transpiration cooling for gas turbine engines date from the 1960's such as in a publication by Lombardo et Al. (1967) [22] performing experimental investigation of transpiration cooled turbine blades in a gas turbine engine with TIT of 2500F^{o} for 150 hours. Throughout the experiment, no structural failures of the blades were encountered, they established some characteristics of transpiration cooled blades, notably: high cooling effectiveness and very high cycle temperature capability.

2.3.2 Mechanisms of transpiration cooling

Direct numerical simulations (DNS) was performed by Christopher et Al. [23], where they investigated the boundary layer in transpiration cooling for a turbulent flat-plate. Two mechanisms are determined to be responsible for the reduction of heat transfer from the hot gas to the wall. First is the reduction in average fluid temperature in the boundary layer due to the injection of coolant. The second mechanism is heat advection away from the wall, which they suggest being the dominant heat-transfer mechanism. Some theoretical models have been proposed to predict this effect [17], [24]–[26], they will be discussed later in subsection 8.1.3. These references are from the 1950's to 1970's, no recent theoretical investigations of this mechanism have been found by the author, indicating a potential area of research.

2.3.3 Investigations of transpiration cooling

Analyses of heat transfer in PM has been extensively performed in the literature, however, simulations and experiments of transpiration cooling in the condition of combustion chambers are uncommon. Most papers involving research of heat transfer in PM focus on their potential as heat exchangers, but do not usually investigate the transpiration cooling effect. Research papers on transpiration cooling can be put into two categories based on their primary aim of study: heat transfer or fluid flow. References on heat transfer are presented first, followed by fluid flow.

2.3.3.1 Heat transfer in transpiration cooling

Andoh et. Al [27] performed a simplified 1D numerical prediction of porous walls under transpiration cooling based on an analytical model. It is the earliest numerical simulation of transpiration cooling found by the author in the literature. Von Wolfersdorf [28] studied double layered PM with a bottom metal PM layer acting as good mechanical strength and a top ceramic PM acting as a thermal barrier. The influence of volumetric heat transfer coefficient and the thermal conductivity on the top ceramic layer was investigated, indicating this structure can be applied to the cooling of gas turbine combustor liners. Shi et. Al [29] used an intelligent genetic algorithm to optimize a two layer PM for transpiration cooling and proposed optimization factors such as the composition, porosity and thickness of each layer for the structural design. However, the last two references used analytical solutions of a simplified 1D problem, which

ignores the important effects of thermal dissipation inside the solid matrix and the complexity of the boundary conditions. Liu et. Al [30] modeled in FLUENT 6.3 a two layered structural PM in 2D and analyzed the wall temperature distribution for transpiration cooling under various porosities and thermal conductivities. Their results indicate both the porosity and thermal conductivity variations have substantial effect on the temperature distribution. The effects of an obstruction due to fouling was also modeled, creating a large increase in surface temperature due to the blockage. However, their model did not simulate the hot gas flow in the channel above the PM, therefore heat flux due to the interaction between the hot gas and coolant was not modeled, instead, a constant heat flux was applied. Dahmen et. Al [31][32] developed a coupled 2D CFD code of the PM and the channel to solve the heat transfer in PM for rocket combustion liners. They performed experiments and compared the temperature distributions of the samples with simulations, achieving decent prediction of the temperature distribution inside the samples but slightly overpredicting at low BR and more significantly at larger BR. Kilic [11] performed experimental and numerical investigations of transpiration cooling using water as coolant. The RNG $k-\epsilon$ turbulence model gave good approximation to the experimental temperature profile of the surface of the porous plate. It was determined that increasing the Reynolds number causes an increase on surface temperature and decrease on CFE_T. Huang et Al. [33] performed numerical heat transfer simulations using Ansys Fluent on bio-inspired porous structures, notably earth-worms skin. The standard $k-\epsilon$ turbulence model was found to achieve good agreement with experimental data. Their study showed improvement using bio-inspired non-smooth surfaces over smooth surface transpiration cooling. AM is a technology being considered to manufacture and study more of these bio-inspired PM.

The studies summarized above present various approaches to predict temperature distributions of transpiration cooling. Ansys Fluent has shown its ability to fulfill this task. However, there seems to be a lack of studies simulating transpiration cooling along with the convection caused by the channel hot gas stream. This thesis will attempt to simulate such conditions.

2.3.3.2 Fluid flow in transpiration cooling

Xiao. et Al [34] performed large eddy simulations (LES) of fluid flow in the case of transpiration cooling. They simulated flow inside a channel and in the PM, which sat at the bottom, the surface flush with the main channel wall. This constitutes the typical setup used to perform experiments on transpiration cooling. The Darcy-Forchheimer momentum equation was used to describe the flow inside the PM. The periodic appearance of a three-vortex system for $BR = 0.01$ was obtained, matching experimental results. It was found that the mass flux inside the PM fluctuates periodically. Efstathiou et Al. [35] performed measurements of turbulent boundary layer over open-cell porous foams with varying pore size and thickness, but constant porosity ($\epsilon \sim 97\%$). They found the turbulent boundary layer structure transitions from a smooth wall to the PM rapidly, approximately <10δ, δ being the film thickness. Slip velocities are observed, the slip velocities being >0.3U_e where U_e is the free stream velocity. Ali et Al. [36] performed experimental measurements of turbulent boundary layer over permeable walls for use as passive treatments for flow control and suppression of aerodynamic noise. The study has shown penetration of the boundary layer flow into the highly permeable PM, which can generate an internal hydrodynamic field.

Out of the studies presented, none attempted to investigate the concentration of coolant (mass analogy) on the surface of the PM as a mean of studying the CFE. This presents an opportunity in this thesis to add to the literature.

2.3.3.3 Analytical solutions

Analytical models have been developed by various authors for the purpose of performing numerical simulations as mentioned in subsection 2.3.3.1. However, they generally oversimplify the problem, thereby losing accuracy. Typically, analytical models need to be solved in 1D or very simplified 2D problems to be solvable. For this reason, CFD modeling is required for problems with more complexity such as the ones involving the channel and PM flow, with the associated heat transfer interaction.

2.3.4 Transpiration cooling manufacturing and structural integrity

Even though transpiration cooling has been studied for many years and demonstrated its applicability for high cooling efficiency, problems occur when the components have to cope

with both thermal and mechanical stresses, as mentioned in subsection 2.2.1, which have limited the application of transpiration cooling to the turbomachinery field [16]. In addition, manufacturing difficulties and modelling complexities resulted in the adoption of effusion cooling as the preferred cooling method in combustion chambers of gas turbine engines [23].

2.3.4.1 Additive manufacturing

With recent advances in additive manufacturing (AM), a renewed interest in the potential application of transpiration cooling for gas turbine engines has risen. Furumoto et Al. [37] manufactured an injection-moulding die as a PM by use of selective laser metal sintering (SLMS): a form of AM. They investigated the permeability and strength of the samples which had very small porosities and permeabilities, approximately 6%-30%, and $10^{-14}m^2$, respectively. More on PM properties such as porosity and permeability in section 2.4. Tensile tests revealed gradual decrease in porous structures tensile strength when porosity exceeded 6%, attaining one third of the tensile strength of a non-porous structure made using SLMS at a porosity of 25%. This is largely attributed to the reduction in mass density caused by an increase in pore volume. Experimental heat transfer tests by Min et Al. [38] of three porous structures produced by SLMS were compared to effusion cooling with two different hole diameters and pitch parameters. The porous structures porosities varying between 10.73%-23.89% showed higher thermal CFE_T at BR of 2.4% and 3.6%, and all except for one at 1.2%. Larger CFE_T of transpiration cooling over effusion cooling at higher BR may be explained by film lift-off in effusion cooling. The peak in cooling effectiveness on the surface was found at the center area. This study showed that the superiority of transpiration cooling over effusion cooling remained true for manufactured PM using AM. CFE_T of porous plates and sintered PM produced by AM were numerically and experimentally investigated by Huang et Al. [39]. Good prediction of CFE_M was achieved numerically using ANSYS FLUENT compared to their experiments. Strain tests were performed on the samples. Porous plates with the least number of holes withstood the highest stress while the sintered PM was the weakest by a factor of ten compared to a solid Inconel piece made by selective laser melting method.

Porous media structures have also been investigated in other fields. Research in chromatography, a laboratory technique for the separation of a mixture, have for the first time successfully 3D printed packed beds, and monoliths with internal channels from CAD models

[40]. They found 3D printing manufacturing enables the creation of PM with precision, scalability, and versatility at low costs. Various other shapes have been investigated and produced using 3D printing such as more packed bed shapes by Nawada et Al. [41], silicon PM based on 3D printed ABS mold by Munro et Al. [42], and structured metal for pool boiling by Wong et Al. [43]. Comparison between CAD theoretical porosities and actual 3D printed samples porosities were compared in [42] which revealed variation percentages of 2.6% to 4.14%, i.e. achieving a porosity of 61.56% when expecting 60%, indicating the possibility of good transfer from CAD to 3D printed samples.

2.4 Porous Media

In this section, PM are defined and the governing equations for flow movement are presented.

2.4.1 Background

A PM is defined as a material consisting of a solid matrix with an interconnected void [44]. The interconnection of the void, typically referred as pores, allows the flow of fluid through the material. PM occur naturally in nature, common examples are beach sand, sandstone, limestone, bread, and wood. They tend to have irregular pore sizes and shapes. Man-made examples are ceramics, composite materials, and high porosity metal foams. Figure 2.6 shows different kinds of porous media.

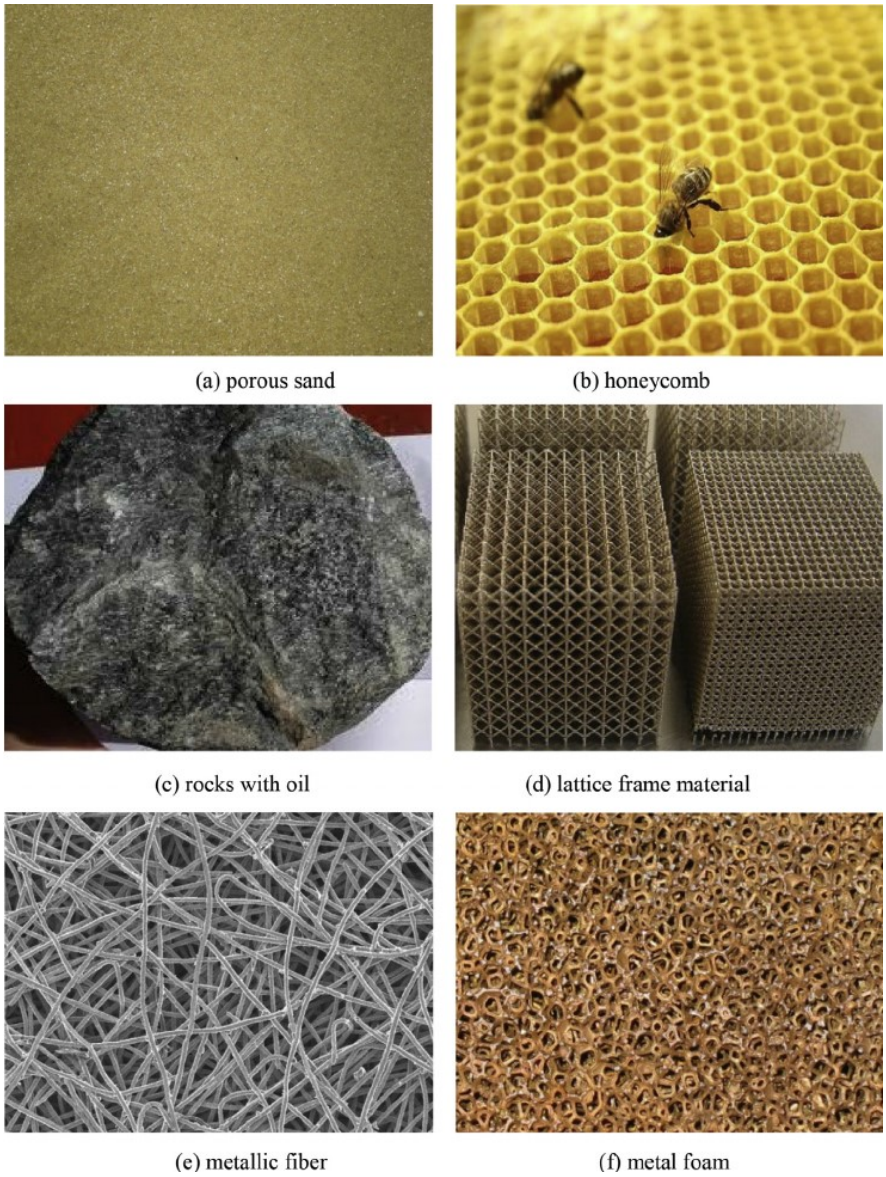

Figure 2.6 Different kinds of PM [45].[5]

On the scale of the pores, the flow quantities i.e., velocity, pressure, density, etc., vary in an irregular manner, however, over multiple pore lengths, fluid behaviors become predictable, therefore predictions through mathematical models are possible. The ratio of the volume of void to the total volume of the porous medium is defined as the porosity (ϵ) and calculated with Eq. (2-7). Thus $1-\epsilon$ defines the ratio of solid volume to total volume.

[5] Reproduced from *H.J. Xu. Analytical considerations of local thermal non-equilibrium conditions for thermal transport in metal foams. International Journal of Thermal Sciences; 2015; Vol. 95: Pg. 73-87*. Copyright © 2015 Elsevier Masson SAS. All rights reserved.

$$\epsilon = \frac{V_{void}}{V_{total}} \tag{2-7}$$

For natural PM, ϵ does not typically exceed 0.6 [44]. Man-made PM on the other hand can have porosities as high as >97%, such as metal foams [46].

2.4.2 Momentum equations

The momentum equations of flow inside PM, which are the PM analog forms of the Navier-Stokes equations, are presented in this subsection. Only the equations relevant to the flow regimes investigated in this study are presented. The body forces such as gravity are neglected here as they can be easily added later.

2.4.2.1 Darcy's law

Breakthrough work by Henry Darcy in 1856 on the water supply of Dijon enabled the development of the first relation between flow rate and the applied pressure difference, shown in Eq. (2-8), for an isotropic medium. Darcy's equation is applied for seepage velocities and represents the surface drag due to friction on particles or fibers [44].

$$\nabla P = -\frac{\mu}{K} v \tag{2-8}$$

where μ is the dynamic viscosity of the fluid, v the velocity of the fluid, ∇P is the pressure gradient, and K a geometric characteristic of the PM with dimensions L^2 called permeability for single-phase flow [44]. For some perspective, K can vary enormously, in $[m^2]$: clean gravel $10^{-7} - 10^{-9}$, clean sand $10^{-9} - 10^{-12}$, with other PM in between up to unweathered clay $10^{-16} - 10^{-20}$ [44]. Permeability of man-made PM can also vary significantly: high porosity metal foams (ϵ > 90%) around 10^{-7} [47], compressed metal foams ($40\% < \epsilon < 80\%$) $10^{-8} - 10^{-10}$ [48], and composite carbon/carbon material PM ($\epsilon \sim 10\%$) around 10^{-13} [31].

2.4.2.2 Quadratic drag: Forchheimer's equation

Darcy's equation (2-8) is valid only for sufficiently small v. The transition to nonlinear drag is smooth, defined by the Reynolds number Re_p of the flow in the range of 1-10, with a characteristic length based on an average particle or pore diameter $d_p\,[m]$ [44]. $Re_p$is calculated using Eq. (2-9).

$$Re_p = \frac{\rho v d_p}{\mu} \tag{2-9}$$

This transition is not one from laminar to turbulent, as at these small Reynolds number the flow in pores remains laminar [44]. In fact, the transition to turbulent flow inside PM typically occurs around Re_p of 300 [31] to 375 [49]. The break down in linearity is justified by the form drag around particles or fibers becoming similar in magnitude to surface drag due to friction. In this inertial regime, Eq. (2-10) is used to describe the flow through a PM, and is called the Darcy-Forchheimer equation [44].

$$\nabla P = -\frac{\mu}{K} v - \frac{\rho f}{\sqrt{K}} |v| v \tag{2-10}$$

where f is a dimensionless form-drag constant, called the inertia coefficient and varies with the structure and properties of the PM. This equation is typically used as a source term to the momentum equation to simulate the fluid flow through a PM in investigations of transpiration cooling.

3 Research Objectives

The motivation for this study stems on the possible improvement of the cooling film offered by transpiration cooling in the thermal protection of gas turbine HGP components such as the combustion liner. The following steps were taken to complete this objective:

1. Inspect the coolant flow inside the PM using numerical simulations based on experiments.
2. Determine the relationship between the CFE_M and governing variables of the Darcy-Forchheimer momentum equation, i.e., porosity, permeability, and inertia coefficient.
3. Design PM to improve the uniformity of the CFE_M by redistributing exiting coolant based on the understanding of the relationship between CFE_M and the governing variables of the Darcy-Forchheimer momentum equation.
4. Propose a heat transfer model and validate using experimental data found in the literature and compare the CFE_T to the CFE_M of designed PM and non-designed PM.
5. Propose a method for assembling a CAD model of designed PM for future production employing AM.

4 Experimental Investigation

Experimental investigation of CFE_M over high porosity PM was performed at the National Research Council of Canada and compared to CFE_M of multi-hole effusion cooling from the literature using the same methodology. It should be noted that the experiments were carried out by Mr. Kivanc Yildiz as part of an undergraduate Thesis submitted in April 2019 in which I assisted for part of both the experimental setup and data acquisition [12]. All other aspects presented in this chapter e.g., project preparation, data analysis, and figures were performed exclusively by Mr. Kivanc Yildiz.

As part of an ongoing research effort, the results from these experimental trials have been used extensively throughout the current work to facilitate model development and validation. Given the direct relevance and importance of these results to the present thesis, key findings have been included in this chapter for completeness. Furthermore, the work presented in Chapters 4 to 6 has been published in [50] as part of the proceedings of the AIAA Propulsion and Energy conference in August 2020, in which I was the primary author.

The goal of the experiments was to investigate the CFE_M of high porosity aluminum metal foams using PSP and compare the results to effusion cooling using the same technique. The experimental setup is described first, followed by the results and discussion.

4.1 Experimental Setup

4.1.1 Wind tunnel and test section

The experimental setup consists of a wind tunnel introducing air into a channel in which the PM to be studied is inserted with its top surface flush with the bottom wall. A reservoir beneath the PM introduces pure nitrogen as "coolant" proxy which flows through the porous media and into the channel. Pressure sensitive paint (PSP), which responds to the partial pressure of molecular oxygen with varying fluorescence intensities upon excitation from UV illumination, was applied to the samples surface. The PSP utilized in this study was a single-luminophore compound from Innovative Scientific Solutions, Inc., which is well suited for isothermal environments. The paint response time (750 ms) is sufficiently fast for steady-state measurements. Both the main stream air and pure nitrogen as coolant proxy were kept at room temperature. When the cooling film is present, nitrogen replaces the main stream air on the sample surface, thus significantly reducing the oxygen partial pressure which is detected through PSP response. The experimental setup is shown schematically in Figure 4.1.

The main stream air is delivered to the 10 cm x 10 cm test section at a velocity of 33 m/s (Reynolds number of approximately 256,000) by an open-loop wind tunnel, located at the Gas Turbines Laboratory of the National Research Council of Canada. Details on the wind tunnel can be found in [51]. Pure nitrogen passes through the porous samples to form a protective film over the top surface of the samples. Measuring the PSP response to UV excitation allows air partial pressures to be determined, that is between 100% on the surface (no coolant flow present) to 0% (air completely replaced by nitrogen/coolant). The PSP excitation is provided by a UV LED light source (model type LM2X-DM) from ISSI and captured by a CCD camera (LaVision ImagerProX 2M). The compressed air canister is only used during calibration tests. Main flow provided by the wind tunnel is 100% air.

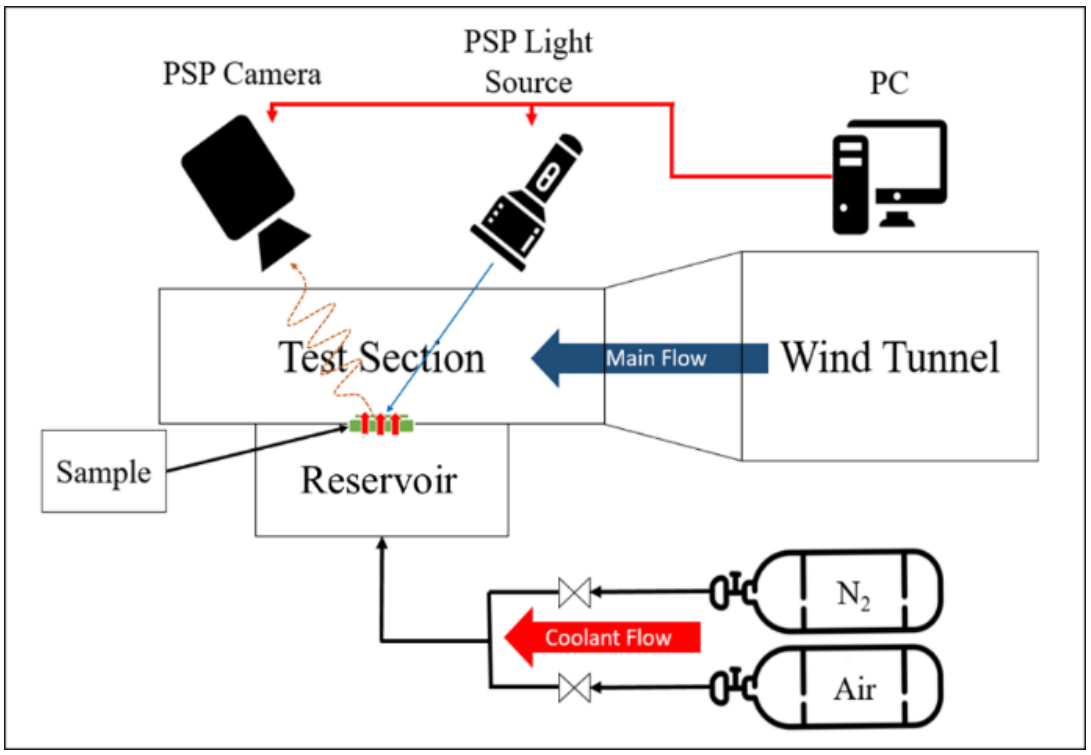

Figure 4.1 Schematic of the experimental setup for studying transpiration cooling using PSP [50]**.**

4.1.2 Porous media PSP application and calibration

Aluminum foams (Duocel®) were machined to 7.5 cm x 2.5 cm x 1.3 cm test coupons. Three samples of different pore sizes, 10, 20 and 40 PPI (pores per inch) were used to examine the effects of pore size on the CFE_M. Despite differences in pore sizes, the samples are of almost identical porosity between 92-94%. PSP was applied to the surface of the samples by applying a thin layer of paint to a flat piece of rubber, and then stamping the PM, thus minimizing the penetration, though some penetration to a maximum of ~1 mm was observed. Figure 4.2 shows the samples with PSP paint applied on their surface, which appears in pink.

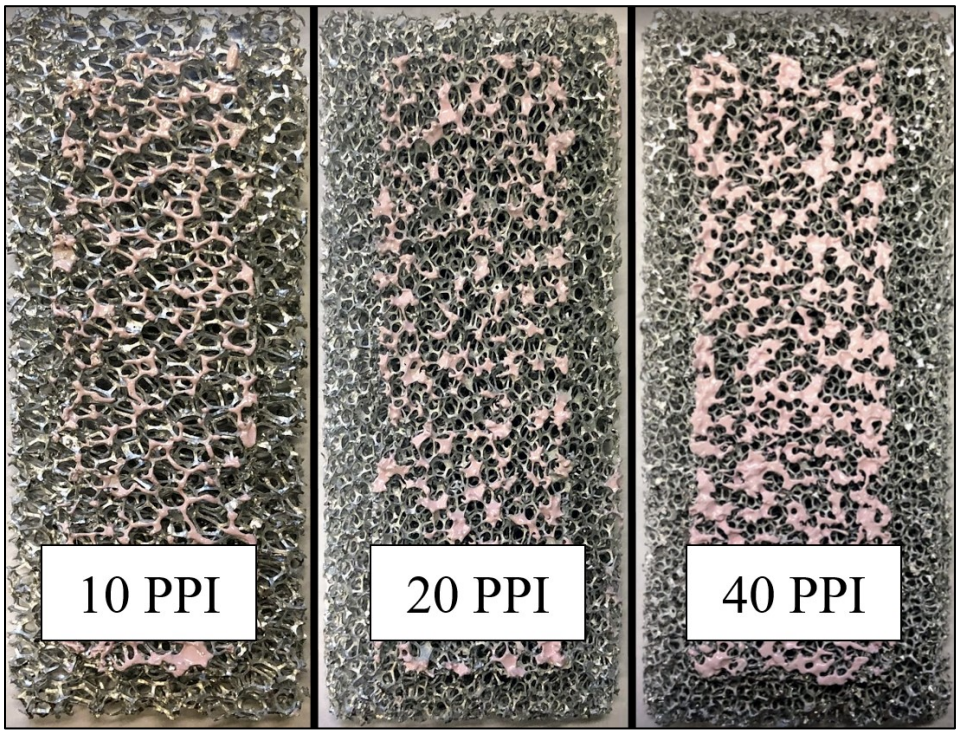

Figure 4.2 Duocel® porous aluminum materials used in the experimental study with applied PSP appearing in pink [50]**.**

To achieve accurate readings of the ratio between nitrogen coolant to air over the sample surfaces, calibrations were performed using captured images for a range of pre-determined ratios. An example set of PSP calibration data for the 20 PPI porous material sample is shown in Figure 4.3, with the test sample fully immersed in blends of air and pure nitrogen with specified nitrogen enrichment percentages between 0% (100% air) to 100% (pure nitrogen: air is fully replaced by nitrogen as coolant proxy). Fluorescence intensity maps at varying levels of nitrogen enrichment allow calibrations of PSP responses for each pixel for a particular test sample. The wind tunnel was not operated during calibration steps to ensure full coverage of known mixture ratios over the samples.

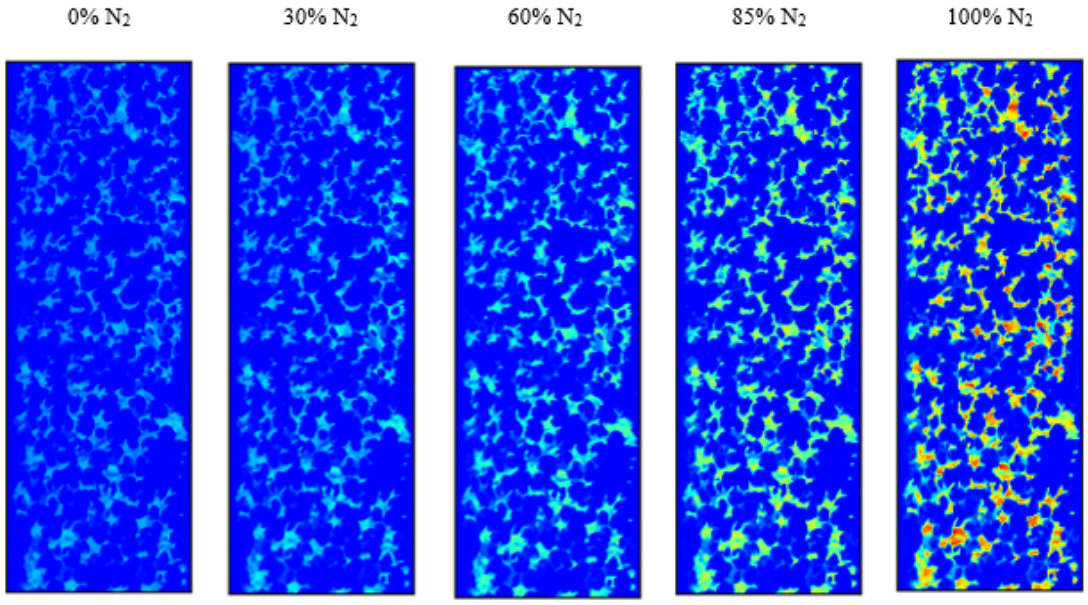

Figure 4.3 Using calibration data sets, second order polynomial regression of 2D PSP fluorescence intensity maps for calibrating a 20 PPI porous sample was performed. The N_2 percentage indicated at the top of the figures is the volumetric percentage of N_2 in the calibration gas blends, with air as the balance [50]**.**

Regressions were performed on every pixel for all samples. An example of the regression $Ax^2 + Bx + C = Light\ Intensity\ (LI)$ where x is N_2 enrichment in volumetric percentage in the calibration gas is shown in Figure 4.4 for the porous sample shown in Figure 4.3.

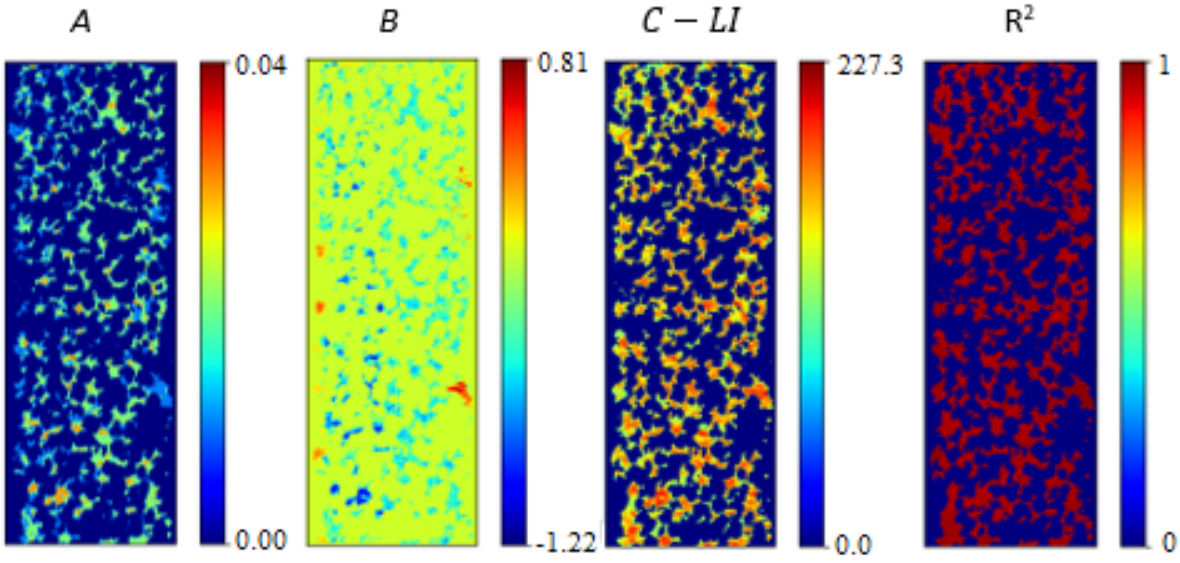

Figure 4.4 Second order polynomial regression performed on the calibration data sets for the 20 PPI porous sample shown in Figure 4.3 [50]**.**

Figure 4.4 shows the regression coefficients and the computed R^2 values. Open pores and aluminum ligaments can be distinguished in the R^2 map by 0 and 1, respectively, which is used for filtering and determining cross-section area A_c, defined as the open surface area of the PM.

4.1.3 Cooling film effectiveness measured by mass analogy

Figure 4.5 shows a set of typical experimental data from PSP transpiration cooling measurements. It was obtained using the 20 PPI sample, shown in Figure 4.3 and Figure 4.4. N_2 was supplied to the test coupon at a flow rate of 20 standard liters per minute (SLPM).

Figure 4.5a) is a 2D map of the CFE_M inferred from the PSP fluorescence image of the porous sample using the pixel-wise calibration curves, where the CFE (η) is defined in temperature terms by Eq. (2-5). By applying heat/mass transfer analogy, the CFE can be re-written using Eq. (4-1) by asserting molecular-oxygen concentration in the coolant proxy, $X_{O_2,C}$, to zero, which is the case since pure N_2 was used as "coolant".

$$\eta = \frac{T_{HG} - T_w}{T_{HG} - T_{ci}} \approx \frac{X_{O_2,Air} - X_{O_2,film}}{X_{O_2,Air} - X_{O_2,C}} = 1 - \frac{X_{O_2,film}}{X_{O_2,Air}} = 1 - X_{Air,film} = X_{C,film} \quad \textbf{(4-1)}$$

where $X_{O2,film}$ is the oxygen concentration in the film, adjacent to the PSP paint with the presence of foreign gas as coolant, $X_{O2,Air}$ is the oxygen concentration in air, $X_{C,film}$ the concentration of coolant in the film in contact with the wall. Substituting $X_{O2,film}$ with the product of $X_{Air,film}$ and $X_{O2,Air}$, it can be shown that the CFE_T can be directly linked to the concentration (by volume) of the oxygen-free coolant near the test sample surface $X_{C,film}$.

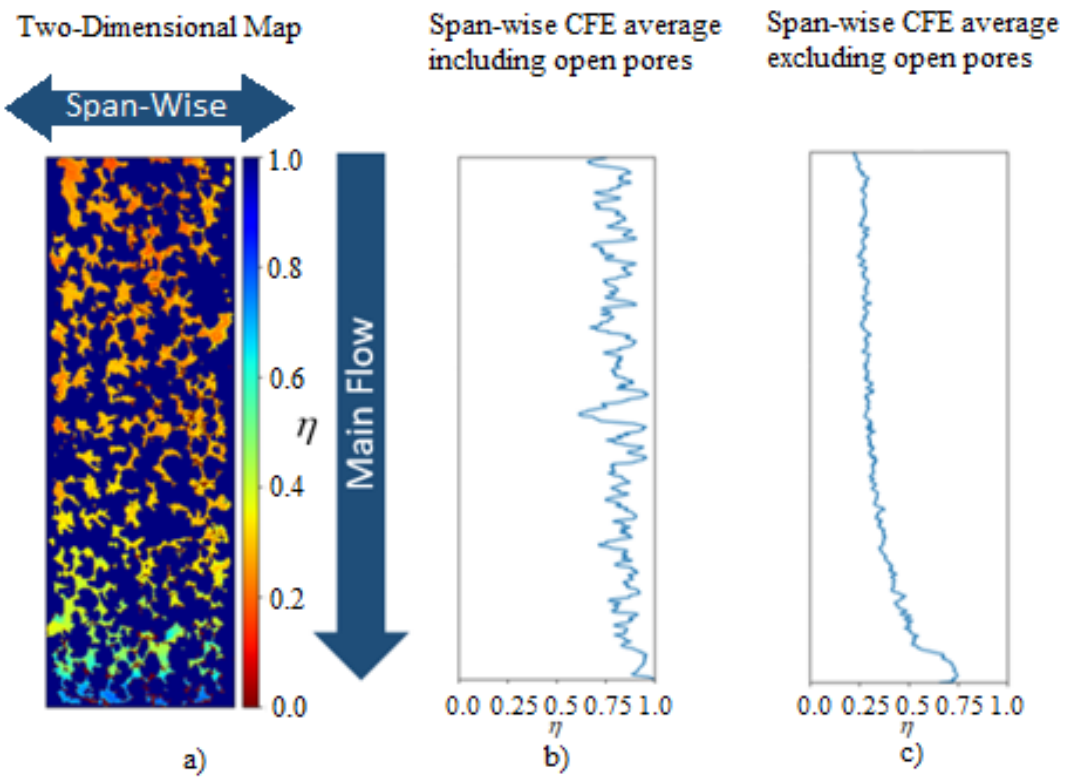

Figure 4.5 a) Shows the measured 2D distribution of CFE$_M$ η with blue being high CFE$_M$ and red low CFE$_M$, b) is the span-wise CFE$_M$ average including open pore areas, and c) shows the span-wise CFE$_M$ average excluding open pore areas. Experimental results for the 20 PPI, 20 SLPM case [50]**.**

The heat/mass transfer analogy was accepted by making four fundamental assumptions [52], [53]:

- Assumption 1: analogous boundary conditions: surfaces are considered adiabatic in heat transfer whereas they are impenetrable in mass transfer.
- Assumption 2: flow field is well turbulent. Reynold's number calculations (~256,000) show that flows are highly turbulent and satisfy this requirement.
- Assumption 3: the wall temperature is equal to the film temperature.
- Assumption 4: the heat transfer case would neglect radiative heat transfer.

For Assumption 1, it was apparent from the PSP application procedure that the paint was largely applied to the ligaments of the porous sample, where surface is impenetrable to mass transfer. Therefore, the given PSP measurements would result in adiabatic cooling efficiencies over the paint surface.

Assumption 3 causes the CFE_M reported to be the minimum possible CFE_T value. In effusion cooling the film temperature equals the wall temperature as no other heat transfer mechanisms than convection significantly influence the wall temperature, assuming no radiative heat transfer. However, in transpiration cooling conduction into the porous media combined with convective heat transfer inside the PM would reduce the wall temperature below the film temperature, increasing the CFE_T.

Even though a discrepancy exists between CFE_M and CFE_T, CFE_M is expected to be a good proxy to the CFE_T and improvement in CFE_M is anticipated to provide improvement in CFE_T.

A 2D map of measured CFE_M is presented in Figure 4.5a) for the 20 PPI – 20 SLPM case. A common color mapping was applied to all 2D maps presented in this study, with blue representing high CFE_M close to unity and red representing low CFE_M close to zero. The span-wise CFE_M averages with open pore areas included and excluded over the main flow direction are shown in Figure 4.5b) and Figure 4.5c) respectively. Open pore areas have unity CFE_M by definition as they represent no heat deposited on a solid surface of the PM. Therefore, the span-wise CFE_M averages with open pore areas included are very high due to the high porosity of porous materials. Both curves are of interest as the CFE_M average with open pore areas included represents reduction in total heat transfer deposited on the PM compared to a flat plate with no cooling. While the average with open pore areas excluded represents the cooling film protection on solid ligaments of the PM.

CFE_M for combinations of coolant flow rates and test sample pore sizes are summarized in Figure 4.6. As the coolant flow rate was increased, the CFE_M increased for all the cases. For the sample size investigated in this work, the CFE_M for the first three-quarters of the samples are relatively uniform but increase rapidly towards the trailing edge, indicating non-uniform CFE_M and coolant mass flow rate distribution.

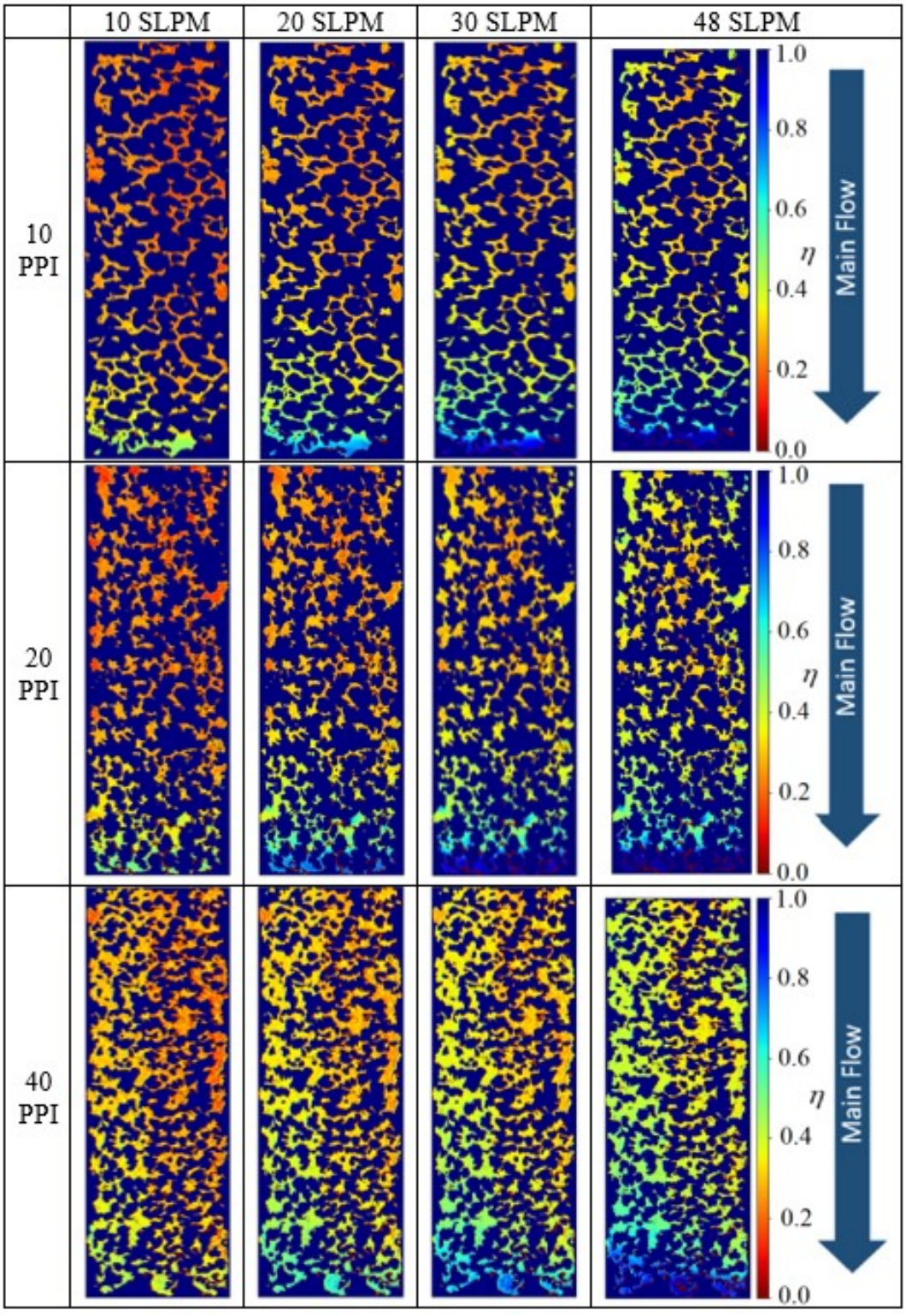

Figure 4.6 A summary of measured 2D distributions of CFE_M for a range of combinations of different pore sizes and coolant flow rates [50]**.**

4.2 Results and Discussion

The parameter for characterizing the momentum ratio between "coolant" and main stream flow can be adapted from the standard blowing ratio (BR) defined for conventional multi-hole effusion cooling using the cooling gas mass flux $\dot{m}_c$ as shown in Eq. (2-4).

In conventional effusion cooling, the cooling passage cross-section area A_c is defined as the sum of the surface area of all the effusion cooling holes and is typically small relative to the cooled surface, as seen in Figure 4.7b). The coolant exits the effusion cooling surface from these discrete cooling holes. However, A_c of the porous materials used in transpiration cooling is much larger relative to multi-hole effusion cooling for a similar cooled surface area as seen in Figure 4.7a).

As discussed earlier, A_c was determined using R^2 map as shown in Figure 4.4. A modified non-dimensional parameter was proposed to compare porous material transpiration cooling with multi-hole effusion cooling at comparable coolant consumption rates. Defined as the BR normalized over the full surface of a test coupon (BR_{FS}); BR values can be converted to BR_{FS} using Eq. (4-2):

$$BR_{FS} = BR \times \frac{A_c}{A_{FS}} = BR \times \sigma \tag{4-2}$$

Table 4-1 lists the conditions of all the transpiration cooling tests performed in the experimental study. For each porous test samples, the surface porosity σ can be defined as the ratio of open pore area at the test coupon surface A_c, and the total surface area of the coupon A_{FS}.

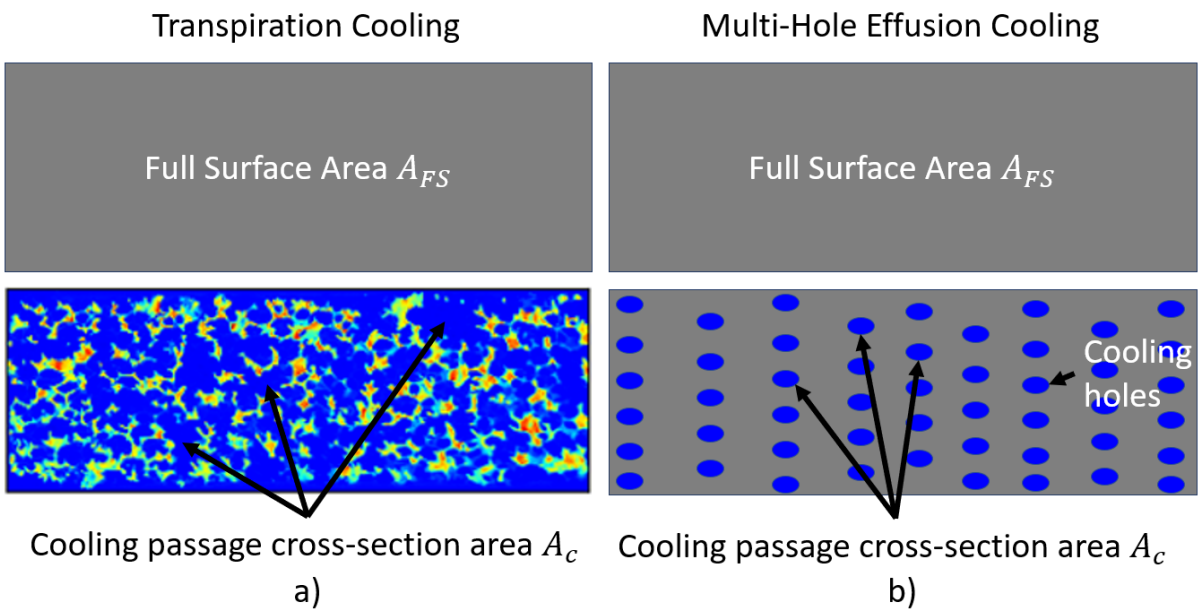

Figure 4.7 Schematic of full surface area A_{FS} and cooling passage cross-section area A_c for transpiration cooling (panel a) and multi-hole effusion cooling (panel b).

With surface porosity determined for each porous material coupon from calibrating runs, both BR and BR_{FS} can be calculated for all coolant flow rates using equations given in this section and are reported in Table 4-1.

Table 4-1 Matrix of test conditions of all PSP cooling tests performed [50]**.**

PPI	*SLPM*	$\boldsymbol{\sigma}$ *(%)*	$\boldsymbol{BR}$	$\boldsymbol{BR_{FS}}$
10	10	73.69	3.40E-03	2.51E-03
	20	73.69	6.81E-03	5.02E-03
	30	73.69	1.02E-02	7.53E-03
	48	73.69	1.63E-02	1.20E-02
20	10	68.97	3.63E-03	2.50E-03
	20	68.97	7.26E-03	5.01E-03
	30	68.97	1.09E-02	7.51E-03
	48	68.97	1.74E-02	1.20E-02
40	10	52.86	4.78E-03	2.53E-03
	20	52.86	9.56E-03	5.05E-03
	30	52.86	1.43E-02	7.58E-03
	48	52.86	2.29E-02	1.21E-02

For comparison, the *BR* values reported in a multi-hole effusion cooling study can be converted to BR_{FS} using cooling hole diameter and streamwise and spanwise hole array pitches [52], [53], as summarized in Table 4-2. CFE_M from transpiration cooling using all three porous samples are compared to those of multi-hole effusion cooling at comparable specific coolant consumptions [54], as shown in Figure 4.8.

Table 4-2 BR from a multi-hole effusion cooling study [54] **and corresponding BR_{FS}** [50]**.**

BR	BR_{FS}
0.4	3.52E-03
0.6	5.29E-03
0.8	7.05E-03
1.0	8.81E-03
2.0	1.76E-02

By comparing Table 4-1 and Table 4-2, two sets of data have comparable BR_{FS} values (within 10% of each other) and are presented in Figure 4.8: (a) effusion cooling with BR = 0.6 (BR_{FS} = 5.29E-03) vs. transpiration cooling at 20 SLPM coolant flow rate (BR_{FS} = 5.01E-03), (b) effusion cooling with BR = 0.8 (BR_{FS} = 7.05E-03) vs. transpiration cooling at 30 SLPM coolant flow rate (BR_{FS} = 7.51E-03). Figure 4.8c) compares multi-hole effusion cooling with a BR = 2.0 (BR_{FS} = 1.76E-02) to transpiration cooling with a mass flow rate of 48 SLPM (BR_{FS} = 1.21E-02), (approximately 30% lower BR_{FS}). The x-axis is the distance along the main flow direction.

Span-wise CFE_M averages with open pore areas included and excluded are presented in Figure 4.8 by thin and thick lines, respectively. The significance of CFE_M with open pore areas included are twofold: (1) the span-wise averages for multi-hole effusion cooling are reported in the literature [54] including cooling holes [52], [53], and (2) span-wise averages including open pore areas represent the reduction of total heat transfer deposited on the samples surface compared to a flat plate with no cooling. From the comparisons, a threefold enhancement in porous medium transpiration cooling CFE_M over that of the conventional effusion cooling is observed with the cooling holes or open pore areas included. It should be noted that the diameter of effusion cooling holes is not reported in the literature [54], therefore two representative effusion cooling hole diameters, 20 mil and 30 mil were assumed for comparison purposes. Also, CFE_M curves without cooling holes for multi-hole effusion cooling are not included in Figure 4.8 as data for CFE_M without cooling holes of effusion cooling were not available.

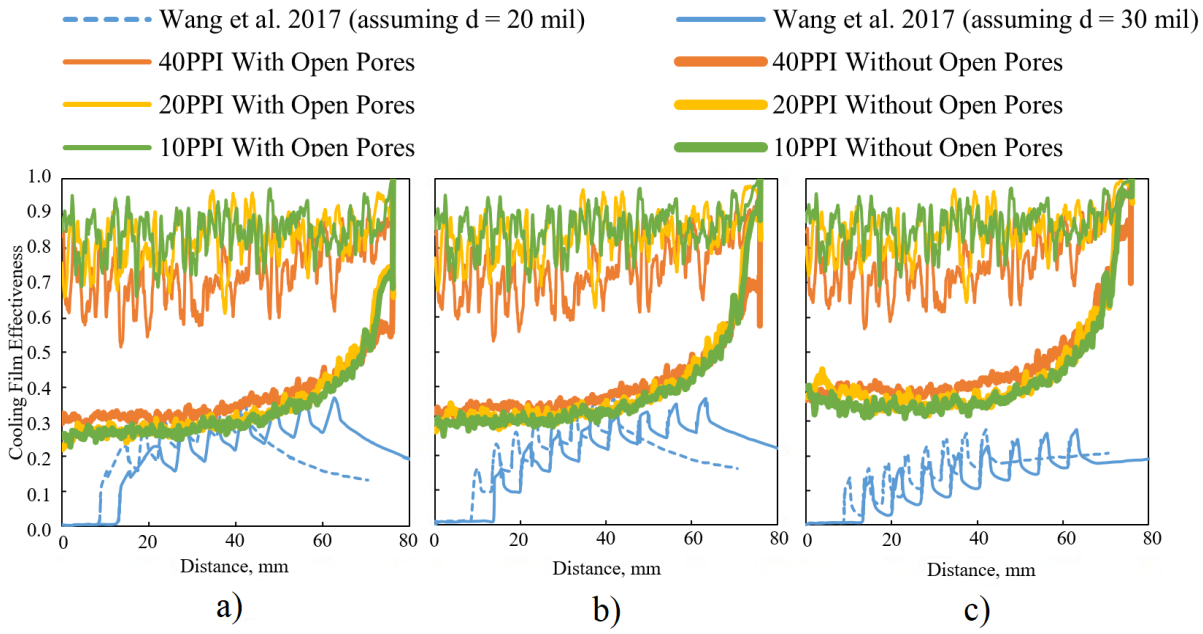

Figure 4.8 Comparisons of average span-wise CFE_M over main flow direction between multi-hole effusion cooling from Wang et Al. [54] **and transpiration cooling for three coolant flow rates: a) (*BR* = 0.6 or BR_{FS} = 5.29E-03) and 20 SLPM (BR_{FS} = 5.01E-03), b) (*BR* = 0.8 or BR_{FS} = 7.05E-03) and 30 SLPM (BR_{FS} = 7.51E-03), c) (*BR* = 2.0 or BR_{FS} = 1.76E-02) and 48 SLPM (BR_{FS} = 1.21E-02)** [50].

Furthermore, a more relevant criteria for assessing a film cooling technique is its ability in producing a cooling film that shields solid surfaces from hot main stream flow so that excessively high material temperatures can be avoided. Therefore, CFE_M averages without open pore areas are calculated and are subsequently compared to those representing multi-hole effusion cooling. As the averages for multi-hole effusion cooling include cooling holes, it is more accurate to ignore the spikes in multi-hole effusion cooling when comparing to transpiration cooling without open pore areas and instead to look at the valleys.

Transpiration cooling with open pore areas offer significantly higher CFE_M than multi-hole effusion cooling, meaning less total inward heat would have to be removed by coolant. As shown in Figure 4.8, when the cooling holes/open pore areas are excluded, transpiration cooling offers approximately 40% higher CFE_M compared to multi-hole effusion cooling at low BR_{FS} = 5.29E-03. The advantages of transpiration cooling are more pronounced at higher coolant flow rates: the enhancement to CFE_M is over 200% at high BR_{FS} = 1.21E-02 (Figure 4.8 panel C).

The experiments suggest that CFE_M values for transpiration cooling start off high at the leading edge of test coupons whereas those of multi-hole effusion cooling gradually increase before reaching their respective maximum values.

The boundary layer on the channel wall prior to the leading edge of the samples is turbulent due to a high Reynolds number of approximately 224,000. Upon interaction with the PM and transpired coolant, the no-slip condition is no longer valid as a substantial slip velocity (>0.3 U_e) occurs, U_e being the free-stream velocity [35]. This is largely due to open pores breaking the contact with solid surfaces. It is therefore expected with a free-stream velocity of $33\frac{m}{s}$ in the experiment for the viscous sublayer to disappear during the transition from the channel wall boundary layer to the PM boundary layer. Nonetheless, very thin viscous sublayers remain on ligaments but their influence on the surrounding flow is expected to be minimal. In turn, the nitrogen concentration captured by the experiment surrounding the paint is likely to be in the buffer layer, where mixing between nitrogen and air is expected due to small eddies. As a result, a gradual concentration gradient is expected. In contrary, a laminar sublayer would produce a sharp concentration gradient and higher measured CFE_M would be anticipated.

Transpiring coolant with low momentum into the boundary layer over the samples yields a steeper velocity gradient compared to the channel wall boundary layer [55]. The transition between flat plate turbulent boundary layers and PM boundary layers ensue over a length of approximately <10δ [35], δ being the thickness of the boundary layer over the PM.

Mixing over the length of the samples will reduce the concentration of coolant directly surrounding the PSP unless a constant flow of coolant transpires. However, as the boundary layer grows and coolant accumulates, a lower mass flux of coolant is required to maintain a constant concentration level. From this reasoning, it can be deduced that a slightly larger amount of coolant exits the leading edge than the center of the samples in the experiments as the CFE_M remains relatively constant or even reduces in the cases of 48 SLPM. This phenomenon is also observed and discussed in Chapter 6.

Overall, the addition of coolant into the turbulent boundary layer results in a thickening of the boundary layer over the length of the PM.

It should be noted that the two BR_{FS} in Figure 4.8c) do not match exactly, however it is interesting to compare as the cooling film of multi-hole effusion cooling is less effective compared to the ones in Figure 4.8a) and Figure 4.8b) despite there being more coolant

consumed in the last scenario. This reduction in CFE_M in the effusion cooling case can be explained by the lifting-off of cooling film from the wall, where high *BR*s lead to coolant jets overshooting and induce vortices that considerably reduce the CFE_M [7], only the far field is properly protected after the cooling film reattaches to the surface [8].

In contrast, micro coolant streams exiting the transpiration cooling surfaces do not overshoot into the main flow but remain within the boundary layer because of their lower momentum. This allows transpiration cooling to reduce inward heat flux to combustor liners by more than two times compared to an effusion-cooled plate as evidenced by a more uniform CFE_M. Therefore, increasing cooling flow rate for transpiration cooling within the *BR* window investigated by this work does not result in cooling film lift-off. Instead, it improves CFE_M by thickening the film despite marginal enhancements, as shown in Figure 4.9. The figure compares span-wise CFE_M averages without open pore areas for the 20 PPI sample at a range of coolant flow rates along the direction of the main flow, because averages excluding open pore areas show a clear trend of cooling film thickening as more coolant is supplied to the test coupons.

Small peaks on Figure 4.9 curves can be observed near the leading edge, followed by slight reductions in CFE_M as most pronounced in the 48SLPM case. The curves stay relatively constant before rapid increases and peaks towards the trailing edge of the samples, indicating a less-ideal, uneven cooling film coverage on the surfaces of the porous materials. A uniform CFE_M would indicate the most effective utilization of coolant for providing thermal protection over the entire surface of a test sample.

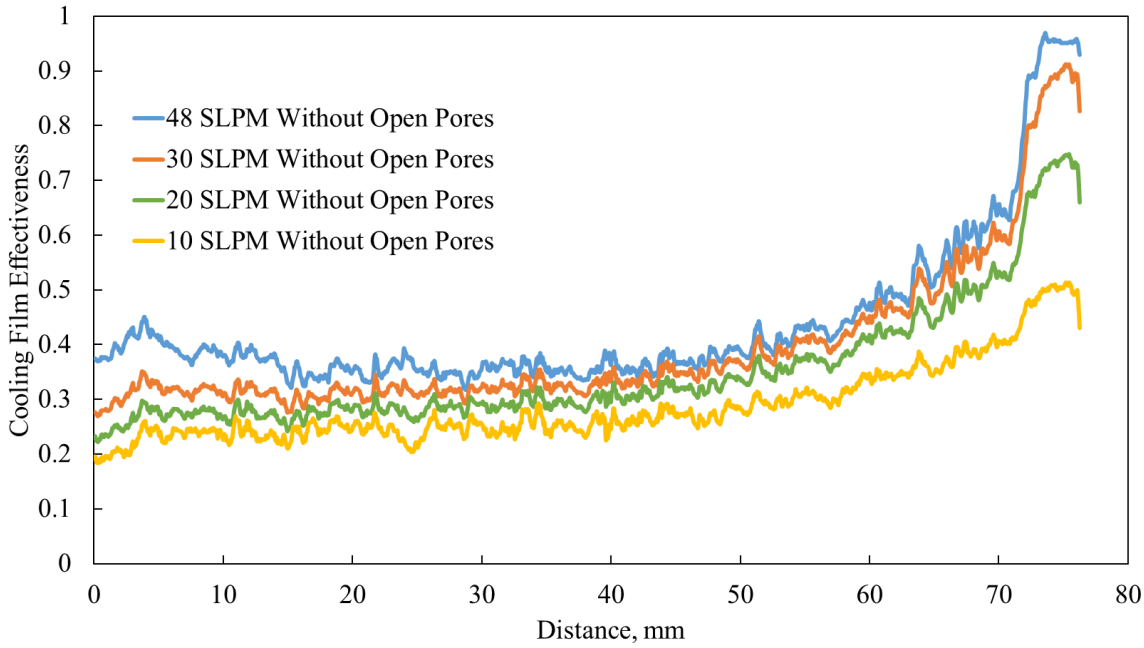

Figure 4.9 Span-wise CFE_M average without open pores along the direction of main flow over a range of coolant flow rates. The porous material coupon has a pore size of 20 PPI [50]**.**

Effects of pore size of porous materials on CFE_M are studied by comparing span-wise CFE_M averages with and without open pore areas for samples of different pore sizes at an identical cooling flow rate of 20 SLPM, as shown in Figure 4.10. Due to the stochastic nature of the porous materials studied, the curves including open pore areas show higher levels of fluctuation, masking the true differences among them. However, the curves excluding open pore areas clearly show that pore size has negligible effects on CFE_M, which can be attributed to the distributed nature of transpiration cooling. This is because samples are covered under continuous cooling film with minimal sensitivity to pore sizes as long as the pores are not too big to disrupt the continuity of cooling films. Good agreement among curves for samples of different pore sizes also highlights the good accuracy and repeatability of the experimental methodology. Matching results were observed at other coolant flow rates studied in this work.

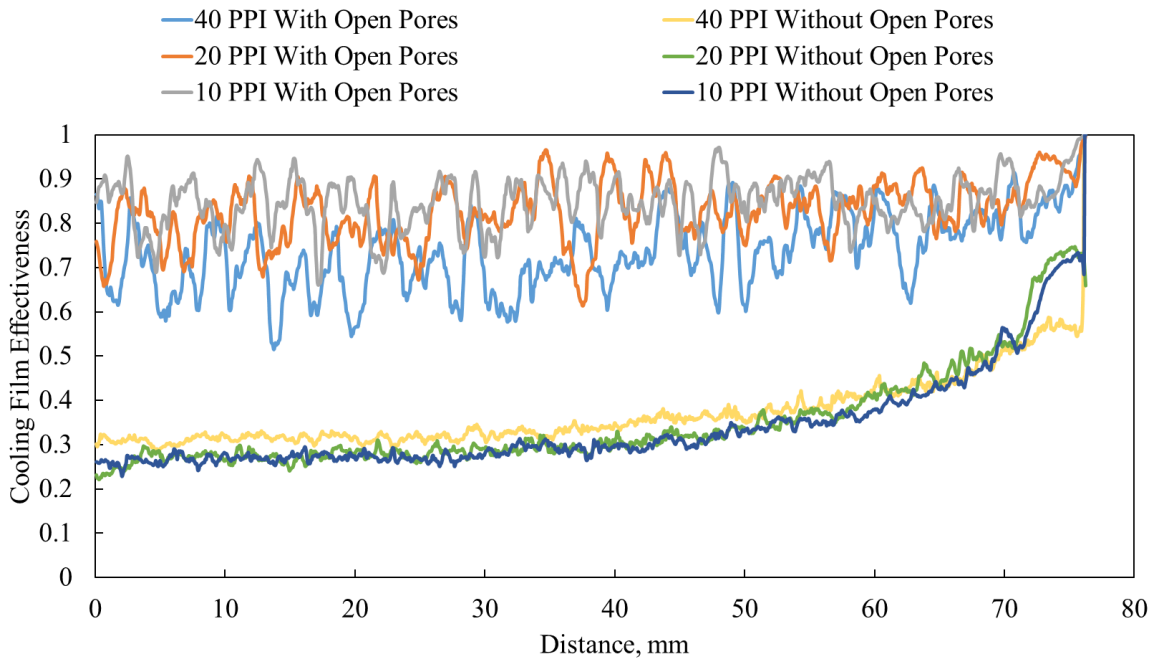

Figure 4.10 Comparison of span-wise averages of CFE_M with and without open pores for porous samples of all three pore sizes: 10 PPI, 20 PPI and 40 PPI. The coolant flow rate was fixed at 20 SLPM (BR_{FS} = 5.01E-03) [50]**.**

It should be noted that differences among averages including open pore areas can be largely attributed to variations in porosity among porous samples featuring different pore sizes (see Table 4-1). Larger PPI introduces a slight source of error as some paint penetration during application is inevitable as smaller average pore diameters result in more interior surface painted, reducing the percentage of open pores to solid surface thus reducing span-wise average CFE_M with open pores.

5 Numerical Model

In this Chapter, the numerical model used to simulate the experiments reported in Chapter 4 is presented. This includes: the domain; boundary conditions; physical models of the channel and PM, such as the governing equations, discretization, and turbulence models; convergence criteria; and mesh validation.

5.1 Domain

A 2D planar simplification of the experimental setup is adopted for numerical simulations as illustrated in Figure 5.1, with the PM (blue) separating the main flow channel (red and green) at the top and a coolant plenum (gray) at the bottom. The modeled channel domain has a height of 10 cm and length of 80 cm. The center of the PM sits at 58 cm from the entrance of the channel, as in the experimental setup. The PM is 7.5 cm x 1.3 cm x 2.5 cm (L x t x W) and the plenum is approximated to 17.5 cm x 10 cm (W x H). The applied mesh contains a total of 486,107 elements, largely quadrilaterals, with the highest resolution around the PM and the bottom wall of the channel having element sizes of 0.1 mm. The bottom wall of the channel has elements sizes of 0.1 mm for a 2 mm thickness, before transitioning to 1 mm elements size. Note that all zones are solved together, meaning all zones are part of the same domain.

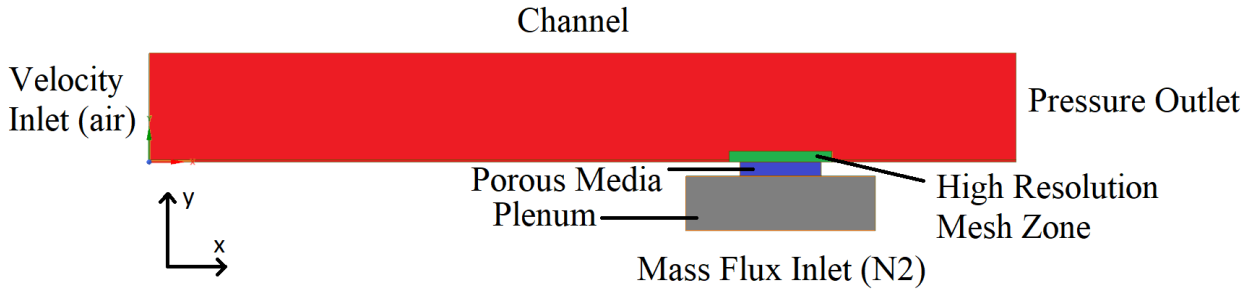

Figure 5.1 Simulation domain of the 2D version of the experimental setup [50].

5.2 Boundary Conditions

Main stream air is introduced into the simulation domain at a velocity of 33 m/s from the channel inlet (left) whereas the channel outlet (right) is at ambient pressure. According to an online resource on CFD, high-turbulence cases inside complex geometries typically have turbulence intensity between 5% and 20% [56]. Medium-turbulence cases with flow in not-so complex geometries such as large pipes typically have turbulence intensity between 1% and 5% [56]. A turbulence intensity of 15% was used for the main stream air inlet due to high turbulence of the flow but the not-so complex geometry of the problem may have warranted a lower turbulence intensity. CFE_M of simulations performed at 5% turbulence intensity and 15% turbulence intensity were compared and no difference was observed, thus the 15% turbulence intensity was kept. The hydraulic diameter of the inlet was set to 0.1 m. The plenum boundary condition is defined as an incoming mass flux of pure nitrogen at the bottom, matching the experimental coolant flow rate. Wall condition is applied to the rest of the boundaries. Both the main stream air and nitrogen inlets are set at ambient pressure and 300 K. The coolant mass flow rate and BR_{FS} are presented in Table 5-1 with BR_{FS} calculated using Eq. (4-2).

Table 5-1 Cooling inlet nitrogen mass flow rate and BR_{FS} per SLPM flow rate [50]**.**

SLPM	*Mass Flow Rate* $\left[\frac{kg}{s}\right]$	BR_{FS}
10	2.08E-04	2.86E-03
20	4.17E-04	5.73E-03
30	6.25E-04	8.58E-03
48	1.0E-03	1.37E-02

5.3 Numerical Method

Ansys FLUENT 2020 Academic version R2 was used to simulate the steady 2D planar flow problem where a pressure-based finite-volume (FV) solver using the Coupled algorithm was adopted. Species transport was solved to compute concentrations of air and coolant nitrogen for determining CFE_M. The gasses are treated as ideal gases.

5.3.1 Channel flow solver

The numerical method used to solve the flow inside the channel is presented in this subsection, beginning with the governing equations, followed by the discretization methods and turbulence model.

5.3.1.1 Governing equations

Fluent solves the conservation equations for mass, momentum, energy, and species transport in the channel with the following equations, respectively [57].

$$\frac{\partial p}{\partial t} + \nabla \cdot (\rho \vec{v}) = 0 \tag{5- 1}$$

$$\frac{\partial (\rho \vec{v})}{\partial t} + \nabla \cdot (\rho \vec{v} \vec{v}) = -\nabla P + \nabla \cdot \bar{\bar{\tau}} + \rho \vec{g} + \vec{F} \tag{5-2}$$

$$\frac{\partial (\rho E)}{\partial t} + \nabla \cdot (\vec{v}[\rho E + P]) = \nabla \cdot \left(k_{eff} \nabla T - \sum_j h_{s_j} \overrightarrow{J_j} + \left[\bar{\bar{\tau}} \cdot \vec{v} \right] \right) + S_h \tag{5-3}$$

$$\frac{\partial}{\partial t}(\rho Y_i) + \nabla \cdot (\rho \vec{v} Y_i) = -\nabla \cdot \overrightarrow{J_i} + R_i + S_i \tag{5-4}$$

where ρ is the density of the fluid, t is time, $\vec{v}$ is the velocity vector, P is the static pressure, μ is the dynamic viscosity of the fluid, I is the unit tensor, $\vec{g}$ is the directional gravitational force or other body accelerations, E is the energy term, k_{eff} is the effective conductivity, ∇T is the temperature gradient, h_s is the enthalpy, $\overrightarrow{J_J}$ represents the diffusion flux of species j, and $\bar{\bar{\tau}} \cdot \vec{v}$ is the viscous dissipation term. Since the equations are solved in steady-state, the terms with time variation are zero. Comparison of CFE_M from simulations with gravity and without gravity showed no difference, thus gravity was neglected. This is supported by large velocities and buoyancy forces that are expected to be small. The energy term E is shown here [57]:

$$E = h - \frac{P}{\rho} + \frac{v^2}{2} \tag{5-5}$$

where h is the sensible enthalpy of the fluid. The diffusion flux of species $\overrightarrow{J_J}$ is calculated for turbulent flows as follows [57]:

$$\overrightarrow{J_J} = -\left(\rho D_{i,m} \frac{\mu_t}{S_{c_t}}\right) \nabla Y_i - D_{T,i} \frac{\nabla T}{T} \tag{5-6}$$

where S_{c_t} is the turbulent Schmidt number ($\frac{\mu_t}{\rho D_t}$ where μ_t is the turbulent viscosity and D_t is the turbulent diffusivity), which measures the relative diffusion of momentum and mass due to turbulence. S_{c_t} is kept to the default value of 0.7. Fluent claims that due to the Schmidt number being an empirical constant that is relatively insensitive to the molecular fluid properties, there are little reason to alter the default value for any species [58].

5.3.1.2 Discretization

The pressure-velocity coupling scheme used was the Coupled algorithm, enforced when using species transport. This solves the conservation equations in a pseudo-transient mode. The Coupled algorithm offers a robust and efficient single phase implementation for steady-state flows, and better performance over the segregated solution schemes such as PISO or SIMPLE [57]. The momentum and pressure-based continuity equations are solved together, resulting in full implicit coupling.

The least-squares cell-based method was used to discretize the gradient between cells. It is comparable to the node-based green-gauss gradient and superior to the cell-based method, however it is less expensive to compute than the node-based method and was thus used [57]. Pressure was solved by second order central difference scheme. Density, momentum, turbulent kinetic energy, turbulent dissipation rate, species transport and energy are all discretized by a second order upwind scheme. The relaxation factor for the flow variables is kept at the default 0.25. The discretization schemes and the Coupled algorithm are also used for the PM.

5.3.1.3 Turbulence model

A comparison of $k-\epsilon$ Standard, Realizable, and RNG turbulence models is shown in Figure 5.2. The $k-\epsilon$ Realizable turbulence model with standard wall functions for near-wall treatment was adopted for the channel and plenum domains. It is a semi-empirical model based on the transport equations of the turbulence kinetic energy (k) and turbulence dissipation rate (ϵ) [57]. It has the benefit of more accurately predicting both planar and round jets, which is relevant with the injection of coolant into the channel [57]. The Realizable model is like the RNG in the first half but closer to the experimental results in the second half, thus acting as a good compromise between Standard and RNG.

The $k-\omega$ turbulence model was tested but was unable to converge, and thus, not considered as an option.

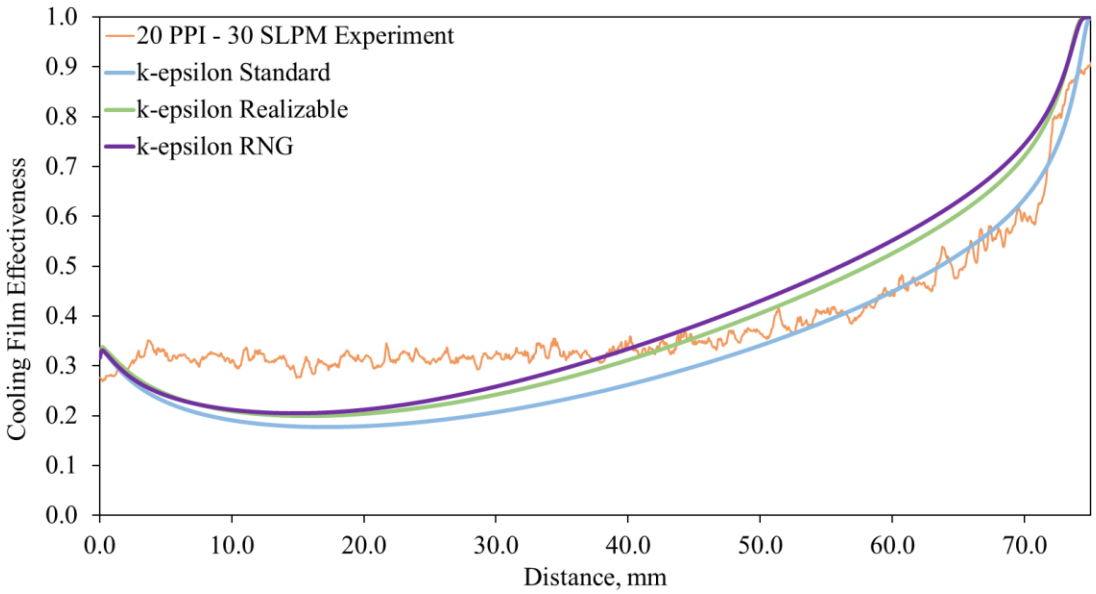

Figure 5.2 Turbulence model comparison between $k-\epsilon$ Standard, Realizable, and RNG, for the 30 SLPM 20 PPI case [50]**.**

5.3.2 Porous media solver

The aluminum foam is described by the porous zone option and defined by the samples' porosity, inertia coefficient, and permeability, which are taken from aluminum foams of similar porosity and PPI [46] and summarized in Table 5-2.

Table 5-2 List of sample porosity, permeability, and inertia coefficient values used in the numerical simulations of Chapter 6. The properties are based on similar aluminum metal foams used in the experiments of Chapter 4 [46][50]**.**

Sample ID	*PPI*	*Porosity* $\boldsymbol{\epsilon}$	*Permeability* $\boldsymbol{K}$ $(\boldsymbol{10^7 m^2})$	*Inertia coefficient* $\boldsymbol{f}$
1	10	0.949	1.49	0.099
2	20	0.9245	1.1	0.104
3	40	0.9272	0.61	0.089

5.3.2.1 Porous media governing equations

The conservation equations for the PM are the continuity and Darcy-Forhheimer (momentum) equations. The continuity equation is the same as Eq. (5- 1) except we must take into consideration the effect of porosity on the average velocity of fluid in a control volume. The Darcy velocity or superficial velocity i.e., the average velocity with respect to a volume element V_m comprising of both solid and fluid is related to the physical velocity of fluid in the void space by $\vec{u} = \epsilon\vec{v}$. Thus, Eq. (5- 1) becomes Eq. (5- 7).

$$\epsilon\frac{\partial \rho}{\partial t} + \nabla \cdot (\rho\vec{u}) = 0 \tag{5- 7}$$

The momentum equation is solved by adding the Darcy-Forchheimer equation as source term to Eq. (5-2) as shown in Eq. (5-8) [44], [46], [47], [59]. The Darcy-Forchheimer source term S_i can be calculated using Eq. (5-9) [60].

$$\frac{1}{\epsilon}\frac{\partial(\rho\vec{u})}{\partial t} + \nabla \cdot \left(\frac{\rho\vec{u}\vec{u}}{\epsilon^2}\right) = -\nabla P + \nabla \cdot \bar{\bar{\tau}} + \rho\vec{g} + S_i \tag{5-8}$$

$$S_i = -\left(\Sigma_{j=1}^{3} D_{ij}\mu u_j + \Sigma_{j=1}^{3} C_{ij}\frac{1}{2}\rho|u|u_j\right) \tag{5-9}$$

where $|u|$ is the magnitude of the superficial velocity, D and C are pre-determined coefficient matrices, and μ is the fluid dynamic viscosity. The first term on the right-hand side represents the Darcy viscous loss and the second term the Forchheimer inertia loss. In the case of a homogeneous PM as in the simulations, the equation reduces to a simplified form following:

$$S_i = -\left(\frac{\mu}{K}u_i + C_2\frac{1}{2}\rho|u|u_i\right) \tag{5-10}$$

where K is the permeability, C_2 is the inertia resistance factor, and ρ is the fluid density. For a steady-state Newtonian incompressible flow in a homogeneous, uniform, and isotropic porous medium with unidirectional pressure drop, the Darcy-Forchheimer source term can be further simplified [46]:

$$S = -\left(\frac{\mu}{K}u + \frac{\rho f}{\sqrt{K}}u^2\right) \quad \textbf{(5-11)}$$

Where f is the inertia coefficient and C_2 in Eq. (5-10) can be related to f by correlation $C_2 = \frac{2f}{\sqrt{K}}$. Parameters summarized in Table 5-2 are used for the porous zone properties of Fluent.

5.3.2.2 Porous media turbulence model

By default, Fluent solves the standard conservation equations for turbulence quantities in the porous medium, and it is treated as if the solid PM had no effect on the turbulence generation or dissipation rates. This implies that Fluent solves the turbulence as if it was an open space. However, the flow within the PM is assessed to be laminar. A laminar zone option was enabled for the PM, effectively setting turbulence viscosity μ_T to be zero, suppressing turbulence generation and dissipation rates. The assumption can be justified by estimating the Reynolds number inside the porous medium by two characteristic lengths, pore diameter Re_p, and permeability Re_K, following literature [44], [61]:

$$Re_p = \frac{\rho U d_p}{\mu} \quad \textbf{(5-12)}$$

where the mean pore diameter of the porous material d_p is given in literature [46] and, U is the coolant velocity.

$$Re_K = \frac{\rho U \sqrt{K}}{\mu} \quad \textbf{(5-13)}$$

The pore Reynolds number is calculated to be below the critical value $Re_p \approx 300$ [31] and the permeability Reynolds number below the critical value $R_K \approx 100$ [44] for safely assuming laminar flow inside PM.

5.3.3 Convergence criteria

Numerical solutions were accepted once the residuals passed below 10^{-6}. These residuals include the continuity, x-velocity, y-velocity, energy, k, ϵ, and species.

5.4 Mesh validation

Since an academic version of FLUENT was used, the maximum number of elements was limited to 512,000. However, this is not expected to be an issue as the simulations are performed in 2D with a small area of interest where mesh concentration was applied. The cells in the channel and the plenum were 1 mm in size, except for the high-resolution area above the PM and up to 2 mm above the bottom wall of the channel which were the same size as the cells inside the PM. In the mesh validation, the cells of interests in and above the PM are varied in three sizes: 0.5 mm, 0.3 mm, and 0.1 mm, the number of elements being 107,198; 143,365; and 486,107, respectively.

A mesh for the 0.1 mm element size using the bias feature is also presented. This feature adjusts the spacing ratio of nodes on an edge, allowing the concentration of elements around the surface of the PM in contact with the channel. A bias factor of 100 was applied below the PM and 10 in the high-resolution mesh zone above, which allows a higher definition of the transition between the PM and the channel. Equations (5-14) and (5-15), are used by Ansys for the bias feature [62].

$$L = \sum_{0}^{n} l_1 \cdot r^n \tag{5-14}$$

where L is the edge length, r is the growth rate, n is the number of divisions, and l_1 is the length of the first element. The bias factor is related to the growth rate and number of divisions with Eq. (5-15).

$$bf = r^{(n-1)} \tag{5-15}$$

where bf is the bias factor. The growth rate is set at the default value of 1.2. Figure 5.3 shows the mesh including the bias feature, for element sizes of 0.1 mm.

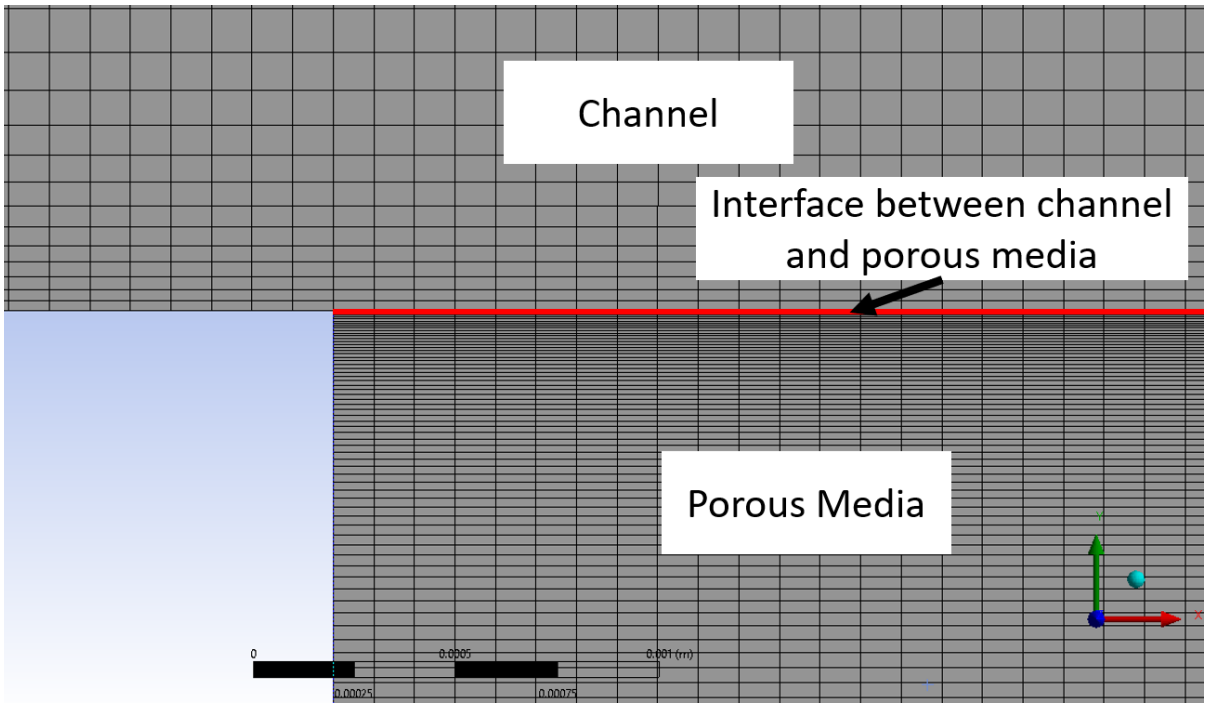

Figure 5.3 Mesh surrounding the surface of the PM in contact with the channel for element sizes of 0.1 mm with a bias factor of 100 applied in the PM and bias factor of 10 in the high resolution zone of the channel.

Figure 5.4a) shows the CFE_M results of the four meshes compared to the experiment. Figure 5.4b) shows the mass flux distribution (ρv) for 1mm below the surface of the PM using only the y-velocity to prevent the inclusion of penetrated air. The mass flux distributions are similar with slightly higher peaks at the trailing edge for finer meshes attributed to mesh refinement. This indicates the coolant flow distribution is converged for all meshes. Thus, the different CFE_M observed in Figure 5.4a) cannot be attributed to different distribution of exiting coolant.

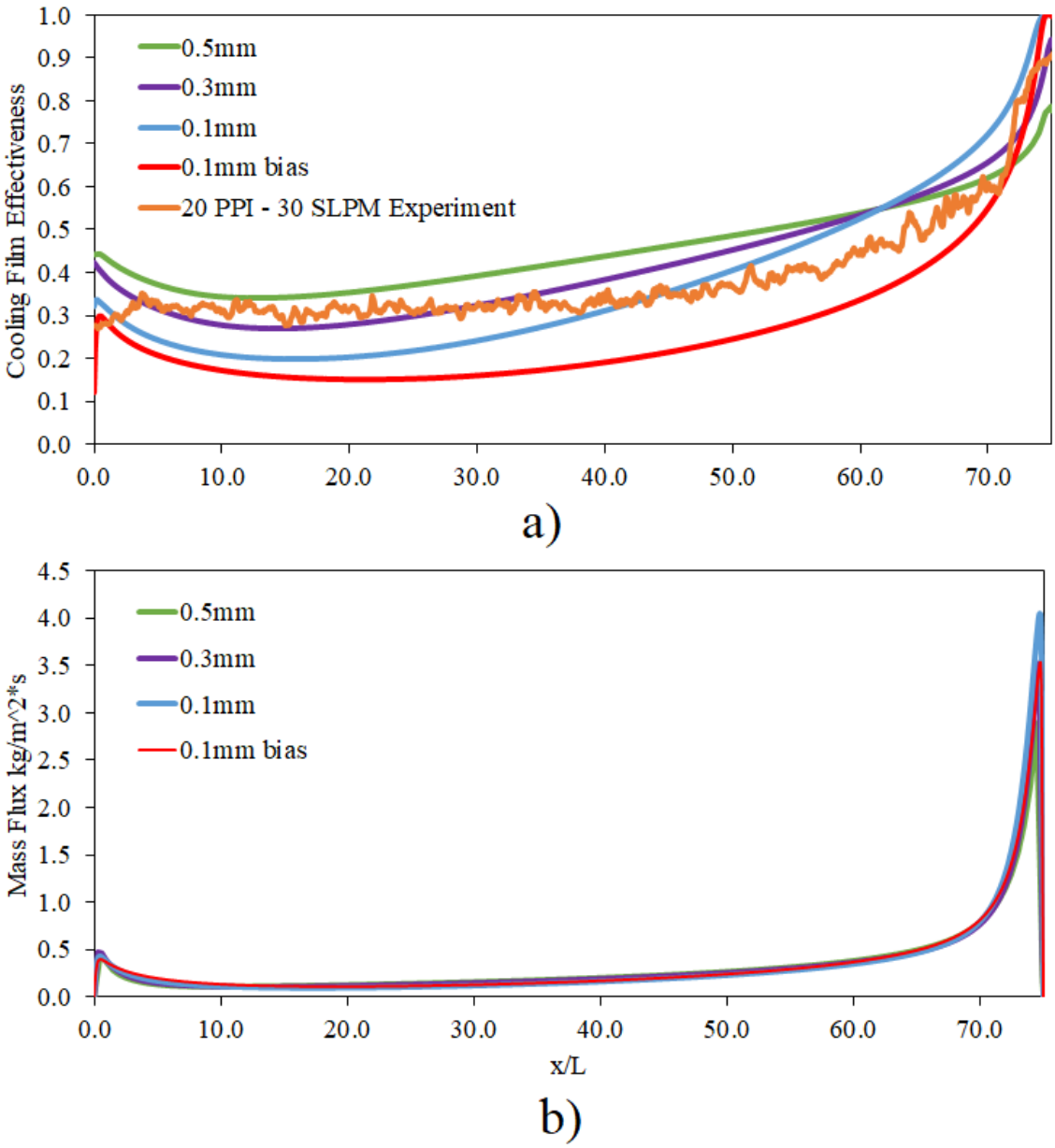

Figure 5.4 Mesh validation for three element sizes of 0.5 mm, 0.3 mm, 0.1 mm, and 0.1 mm with bias for the 20 PPI 30 SLPM case. a) shows the CFE_M and b) shows the mass flux distribution 1 mm below the surface.

CFE_M curves of the different meshes differ significantly, however, this can be explained by the method used to obtain the CFE_M value. The surface of the PM in contact with the channel is at the intersection of two elements, one in the PM and one in the channel, see Figure 5.5 where the mole fraction of nitrogen (CFE_M) is plotted up to 2 mm above and below the surface at 3.5 cm after the leading edge of the PM for the four meshes: 0.5 mm (green curve), 0.3 mm

(purple curve), 0.1 mm (blue curve), and 0.1 mm with bias (red curve). Representation to scale of the elements is also shown. The CFE_M value at the interface is obtained by the average between the two elements where values are saved at their center [63]. Thus, the smaller the element size, the smaller the area for the reported value and therefore different, and in this case lower, CFE_M values. And the values are different because of the non-linearity of the steep transition between the mole concentration of nitrogen inside the PM to the channel.

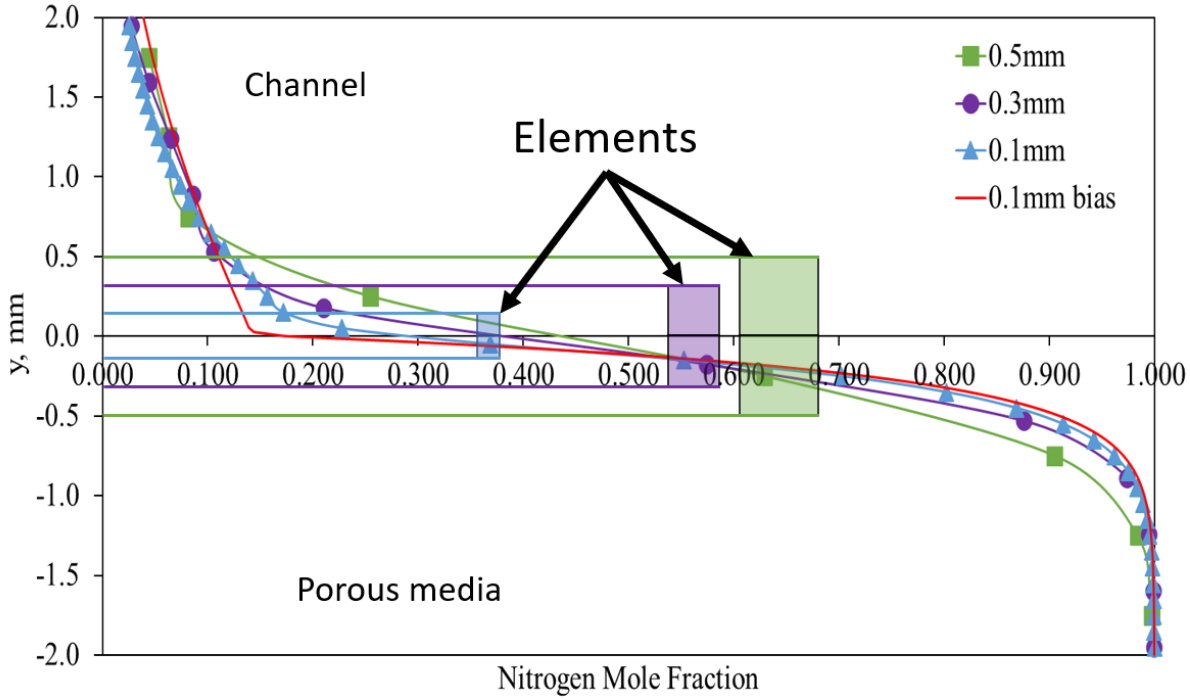

Figure 5.5 Cell values at 0.58 m from the channel inlet (35 mm from start of the PM) for 2 mm above and below of the PMs surface for the 20 PPI 30 SLPM case at element sizes of 0.5 mm (green curve), 0.3 mm (purple curve), 0.1 mm (blue curve), and 0.1 mm with bias factor (red). Element sizes shown for all three non-biased meshes.

It is assumed the mesh size of 0.1 mm with bias to be the correct CFE_M curve for the transition from the PM to the channel in Figure 5.5. With this assumption, comparisons between the different element mesh sizes can be made against the 0.1 mm with bias mesh for the same control area, as shown in Figure 5.6. For example, the 0.5 mm mesh provides the average CFE_M value for an area up to 0.5 mm above and below the surface of the PM in contact with the channel, this can be compared to the average CFE_M value of the 0.1mm mesh with bias for the same area. The comparisons result in similar values, supporting the argument that the CFE_M does not change with mesh size due to dependence on the mesh but rather because

the areas measured to approximate the surface value change. From these comparisons the CFE_M curves in Figure 5.4a) can be better interpreted as the range of CFE_M of different areas around the surface of the PM in contact with the channel.

From the understanding that the CFE_M measured represents a value from the area of the two cells above and below the surface of the PM, it is observed that the numerical curves encapsulate the experimental result in Figure 5.4a), meaning that the CFE_M of the larger area of the 0.5 mm mesh overestimates the CFE_M and the small area of the 0.1 mm with bias underestimates the CFE_M. It is also observed that the CFE_M curves of the different meshes all follow reasonably the shape of the experimental curve.

Thus, it can be reasoned that the CFE_M measured in the experiment can be approximated reasonably for a certain area around the surface of the PM. The 0.1 mm mesh with no bias was used for further simulations as it allows reasonable approximation of experimental results while retaining adequate definition of the transition from the PM to the channel. Although a case could have been made for using the mesh size of 0.3 mm or the 0.1 mm with bias and approximating to an appropriate area.

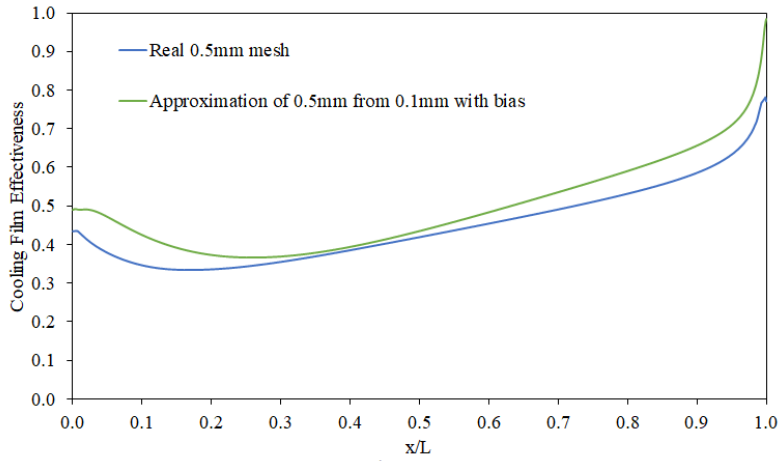

a)

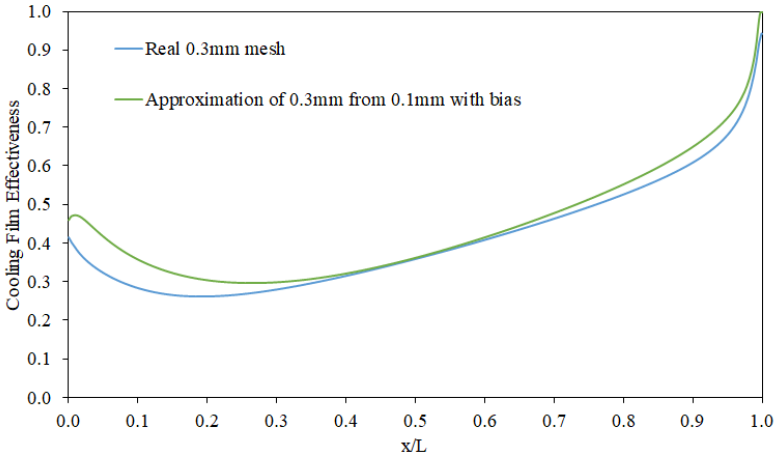

b)

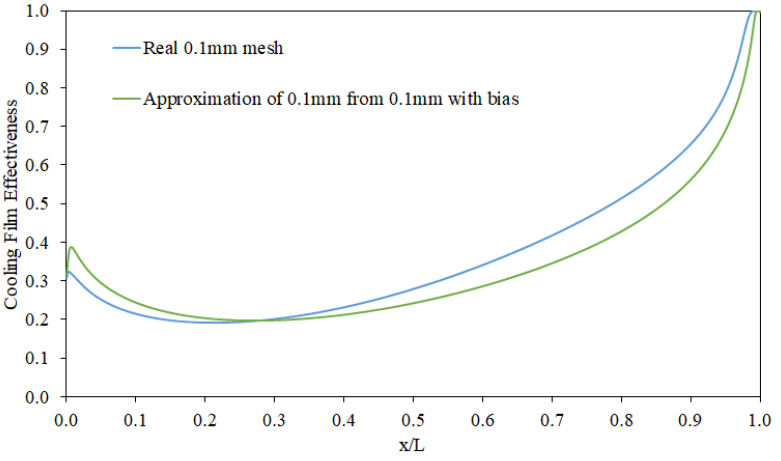

c)

Figure 5.6 CFE_M around the surface of the PM for different areas. A) compares the CFE_M from 0.5 mm above the surface of the PM to 0.5 mm below the surface of the PM from a mesh size of 0.5 mm with no bias to the mesh size of 0.1 mm with biases. B) compares the CFE_M from 0.3 mm above to 0.3 mm below the surface of the PM from a mesh size of 0.3 mm with no bias to the mesh size of 0.1 mm with biases. C) compares the CFE_M from 0.1 mm above to 0.1 mm below the surface of the PM from a mesh size of 0.1 mm with no bias to the mesh size of 0.1 mm with biases.

6 Results and Discussion

In this chapter, the numerical results based on the experimental conditions used in Chapter 4 are presented. First, a look at an example of typical numerical results and the flow inside the PM reveals the effect of high porosity on CFE_M. Followed by comparison of numerical results to the experiments, and finally, a sensitivity analysis is performed to understand the effects of permeability and inertia coefficient on CFE_M.

6.1 A Representative Case

A simulated case that is typical to this study is presented first, with a 20 PPI porous material sample at a flow rate of 48 SLPM or a BR_{FS} of 1.20E-02 as defined in section 4.2.

Figure 6.1 presents the steady-state mole fraction of coolant proxy (nitrogen) and main stream air with red representing 100% air and blue representing pure nitrogen "coolant". A nitrogen layer (cooling film) builds over the length of the sample with varying degrees of mixing with the main stream air. The most interesting part of this figure is a "bubble" of pure nitrogen located at the trailing edge of the sample, a phenomenon also observed in the experiments (Figure 4.9). This indicates that a substantial amount of nitrogen exits towards the trailing edge of the sample, highlighting the non-uniformity of cooling flow exiting the surface of the PM.

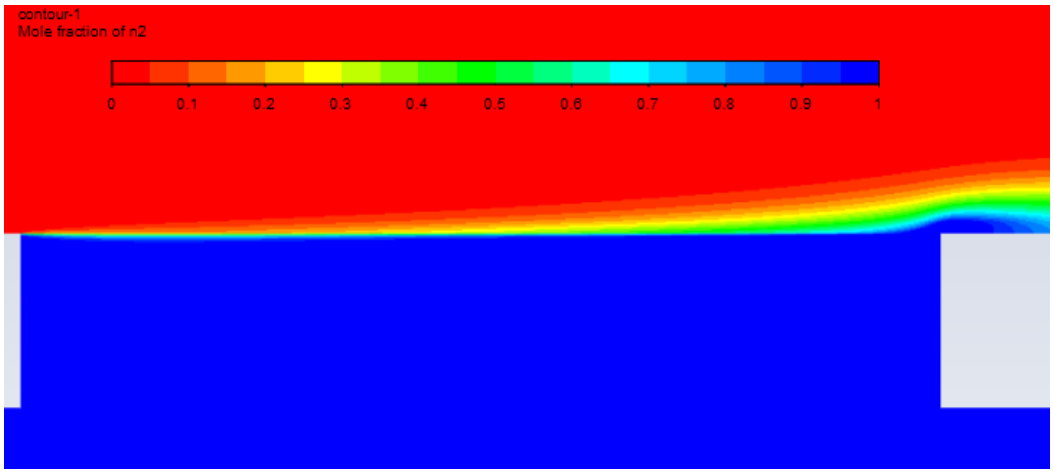

Figure 6.1 Simulated mole fraction of nitrogen inside and over the 20 PPI porous sample with a coolant flow rate of 48 SLPM - BR_{FS} of 1.37E-02 [50]**.**

Mass flux distribution of coolant exiting the PM clearly demonstrates the nonuniformity, as presented in Figure 6.2. This phenomenon was mentioned in section 4.2 and observed experimentally: slightly more coolant exits the leading edge than the center section with an overwhelming amount exiting at the trailing edge.

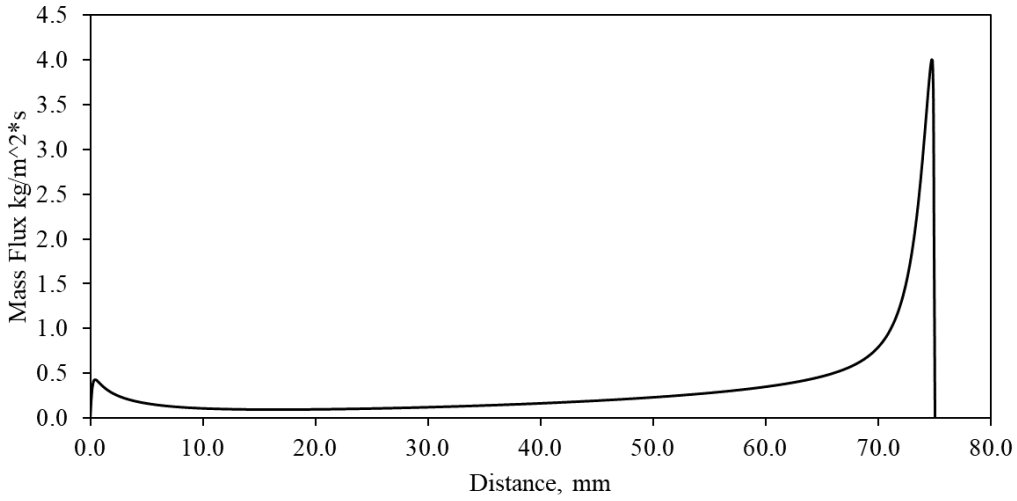

Figure 6.2 Simulation coolant mass flux distribution at 1 mm below the surface of the 20 PPI sample at 30 SLPM - BR_{FS} of 8.58E-02 [50]**.**

Figure 6.3 displays a vector plot illustrating the flow field inside the porous sample. This figure reveals the surge in nitrogen near the trailing edge of the porous sample. As the main stream air moves at 33 m/s over the samples surface, the coolant is entrained by viscous effect, inducing lateral flow motion inside the sample, similar to the lid-driven cavity problem [64]. Lateral motion being along the x-direction of the coordinate system in Figure 5.1, or from the left of the figure to right of the figure in Figure 6.3. The lateral movement of coolant inside the porous medium is stopped by the end wall at the trailing edge of the sample and is redirected upwards into the channel. The lateral flow motion inside the PM also creates a low-pressure zone near the leading edge that is indicated by the reverse flow of coolant. An occurrence also seen in the lid-driven cavity problem on PM [64].

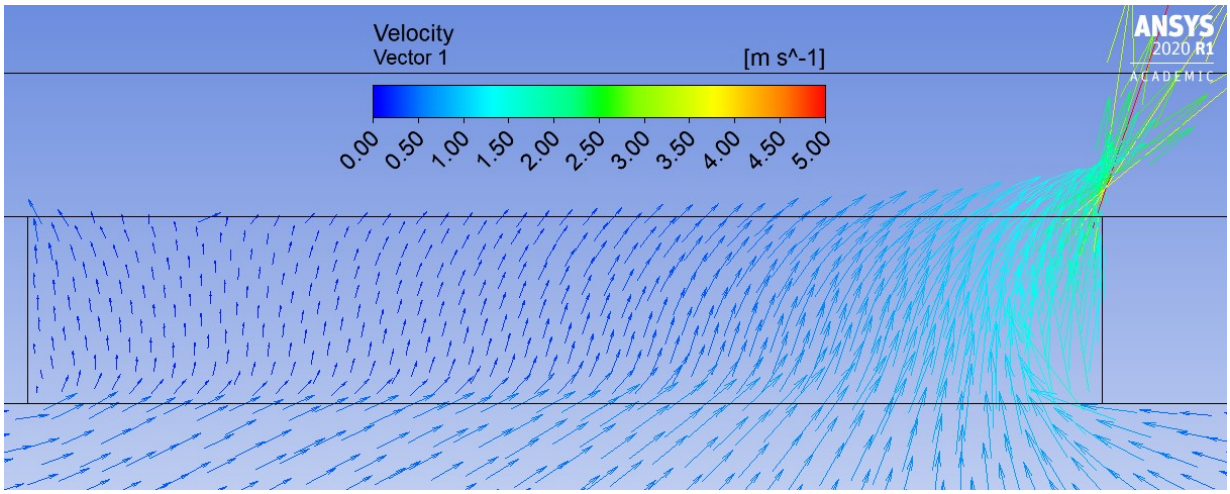

Figure 6.3 Velocity vector field inside the PM for a 20 PPI sample and 48 SLPM - BR_{FS} of 1.37E-02 coolant flow rate [50]**.**

The flow field inside the PM is predominately controlled by pressure gradient and momentum loss as described by the Darcy-Forchheimer term in Eq. (5-11). Properties of porous samples, including porosity, permeability, and inertia coefficient, determine the magnitude of momentum sink terms, also known as flow resistance of the PM. This flow resistance is relatively small for a material of high porosity, high permeability, and low inertia coefficient, allowing fluid to flow through the sample with small pressure drops. High porosity aluminum metal foams, as the ones investigated in this study, are such examples. Alternatively, porous samples featuring low porosity, low permeability, and high inertia coefficient are associated with a dominant Darcy-Forchheimer term and high resistance to flow movement. Assuming isotropic porous samples featuring relatively small Darcy-Forchheimer term, the lateral motion i.e., in the direction parallel to the main stream/hot gas flow, of coolant flow inside the porous sample is induced by the main stream due to viscosity. The explanation is supported by the lack of lateral flow motion in comparison simulations where porous materials are assigned high flow resistances and demonstrated later in Chapter 7.

Lateral motion of coolant inside porous samples is not ideal for transpiration cooling as one of the effects of lateral motion is a non-uniform concentration of coolant (CFE_M) over the surface of the porous samples. If a material of high porosity is used for transpiration cooling, more coolant should be supplied to the leading edge of the samples to generate a more uniform and effective cooling film. Alternatively, a more uniform cooling film could be achieved by

suppressing the lateral flow motion inside the porous sample material with an anisotropic porous medium featuring high flow resistances.

6.2 Cooling film effectiveness as a function of coolant mass flow rate

A comparison of simulated nitrogen mole fraction at the surface of the 20 PPI porous sample at all four coolant flow rates is shown in Figure 6.4. It has been shown in Chapter 4 that the nitrogen mole fraction is identical to the minimum theoretical CFE_T by the design of the experiment. For each simulated case, CFE_M decreases initially before rising and finishing at close to 100%. Similar to experimental results shown in Figure 4.9, higher coolant flow rates result in enhanced overall CFE_M, although the trend is more pronounced in the simulations.

Simulated CFE_M curves for all coolant flow rates have the same initial value. A plausible explanation is that the coolant flow near the leading edge of the porous sample is predominantly controlled by the identical main stream flow which pulls the same mass flow rate of coolant whereas the differences in coolant flow rates are pronounced downstream. However, it is assumed to be a numerical error as the initial CFE_M does not change when the blow ratio is changed in the experiments.

It was noticed that the initial CFE_M value changes based on the mesh size, which was explained in section 5.4, or by the resistance to flow movement of the PM. The latter is explained by a redistribution of coolant due to the change in PM properties.

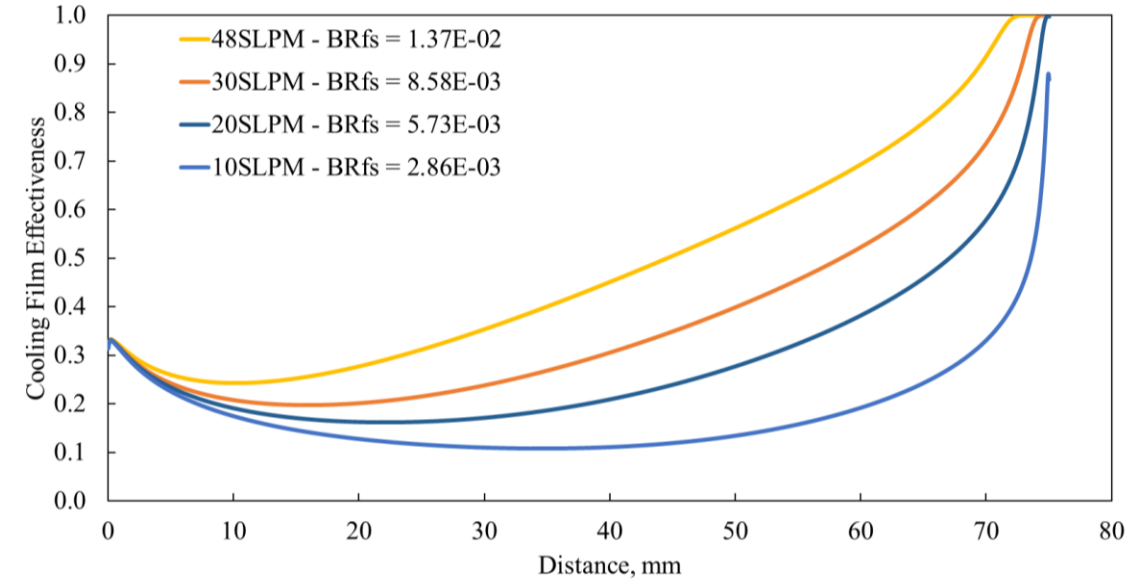

Figure 6.4 Simulated nitrogen mole fraction over the 20 PPI porous sample for all coolant flow rates, where nitrogen mole fraction is identical to theoretical minimum CFE_T by the design of the experiment [50]**.**

6.3 Comparison of experimental and numerical results

The comparisons between experimental measurements and simulated CFE_Ms for the 20 PPI porous sample at all four cooling flow rates are presented in Figure 6.5. The comparisons show reasonable agreement between experimental data and numerical simulations, with discrepancies for the 48 SLPM and 10 SLPM cases.

The material properties of porous samples reported in the literature are adopted as inputs to the simulations [46]. The lack of exact values of the permeability and inertia coefficient of the utilized samples introduces errors in simulating the coolant flow inside the porous samples, moreover the averaging method of numerical simulations does not represent the effects and randomness of varying pore size and internal structure inside real PM. In addition, the boundary conditions in the numerical simulations may not accurately capture the physical realities in the experiments; for example, the peripherals of the porous samples may not be perfectly sealed and the leakages are not quantified and simulated. Moreover, the samples may not have been perfectly flush with the channel wall, causing small discrepancies in results. However, the aforementioned leakage is unlikely to be solely responsible for the CFE_M spike near the trailing edge of the samples, as the leakage does not generate a similar spike in CFE_M at the leading edge of the samples.

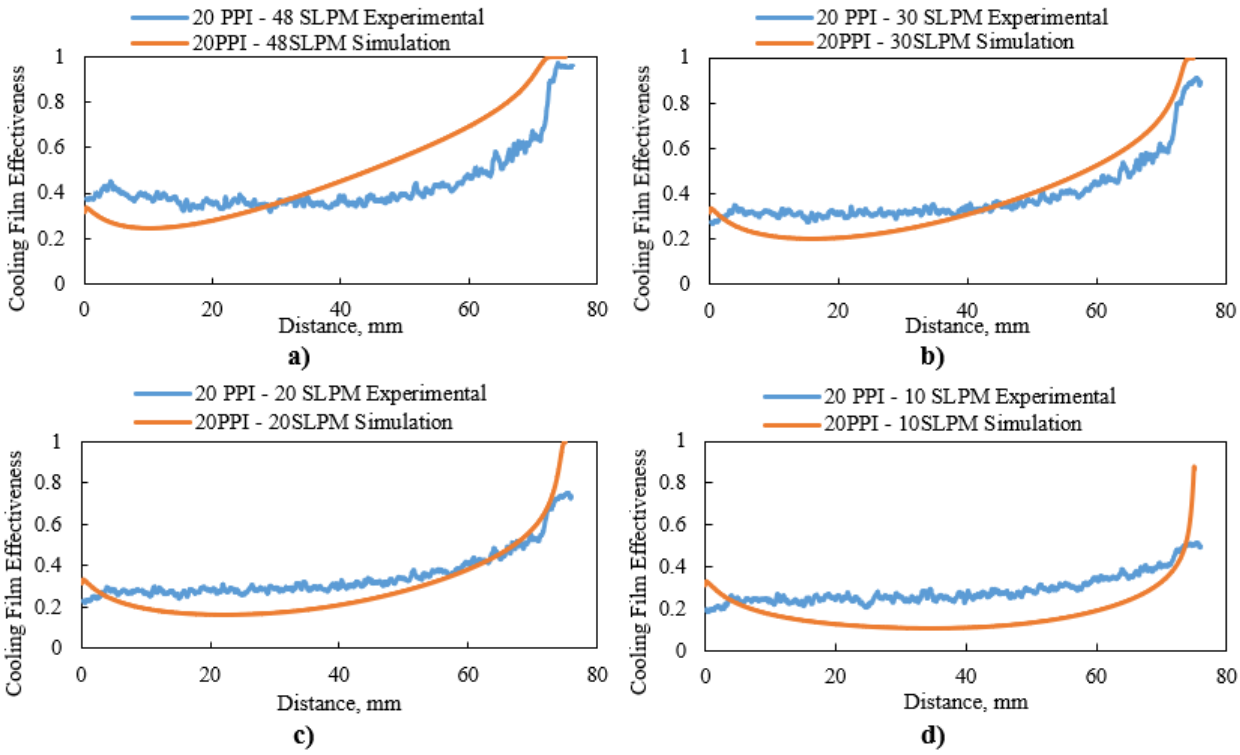

Figure 6.5 Comparisons of CFE_M values between experimental measurements and simulations for the 20 PPI sample at coolant flow rates of a) 48 SLPM or BR_{FS} = 1.37E-02 , b) 30 SLPM or BR_{FS} = 8.58E-03, c) 20 SLPM or BR_{FS} = 5.73E-03 and d) 10 SLPM or BR_{FS} = 2.86E-03 [50]**.**

6.4 Sensitivity Analyses on Cooling Film Effectiveness

To quantify the propagation of the uncertainties in porous material properties to stream-wise CFE_M profiles, sensitivity analyses are performed by varying permeability (K) or inertia coefficient (f) using values close to those found in the literature while holding all other parameters constant. The 20 PPI sample with coolant flow rate of 30 SLPM is chosen as the baseline case due to the good agreement between numerical simulations and experimental measurements.

The analysis of permeability sensitivity is presented in Figure 6.6, where CFE_M curves representing reduced permeability are illustrated by dash-doted lines and increased permeability by dashed lines. It is apparent that CFE_M curves with reduced permeability depart from the experimental measurements, which can be attributed to higher flow resistance distributing coolant more evenly. In addition, the lateral motion of coolant flow inside the porous medium is inhibited with decreasing permeability (increased resistance to flow movement) and the reverse flow near the samples leading edge is suppressed. The trends support the hypothesis that low interior flow resistance is responsible for the reverse flow as described earlier in section 6.1.

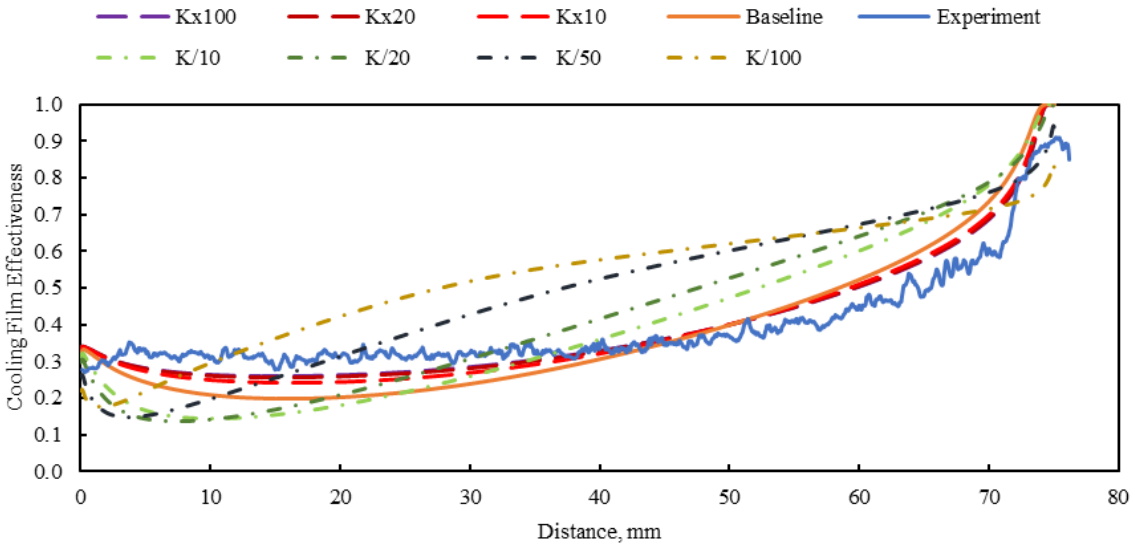

Figure 6.6 CFE_M sensitivity on porous medium permeability K, with Kx denoting a multiplication (decrease in flow resistance) and K/ denoting a division (increase in flow resistance). The analysis was performed on the baseline case of 20 PPI porous sample with a coolant flow rate of 30 SLPM, or BR_{FS} = 8.58E-03 [50].

Effects of the inertia coefficient on CFE_M are presented in Figure 6.7, with suppressed inertia coefficient (reduced resistance to flow movement) illustrated by dash-doted curves and augmented inertia coefficient (increased resistance to flow movement) by large, dashed lines. The sensitivity analysis suggests that increasing the inertia coefficient has a similar effect to decreasing the permeability and vice-versa.

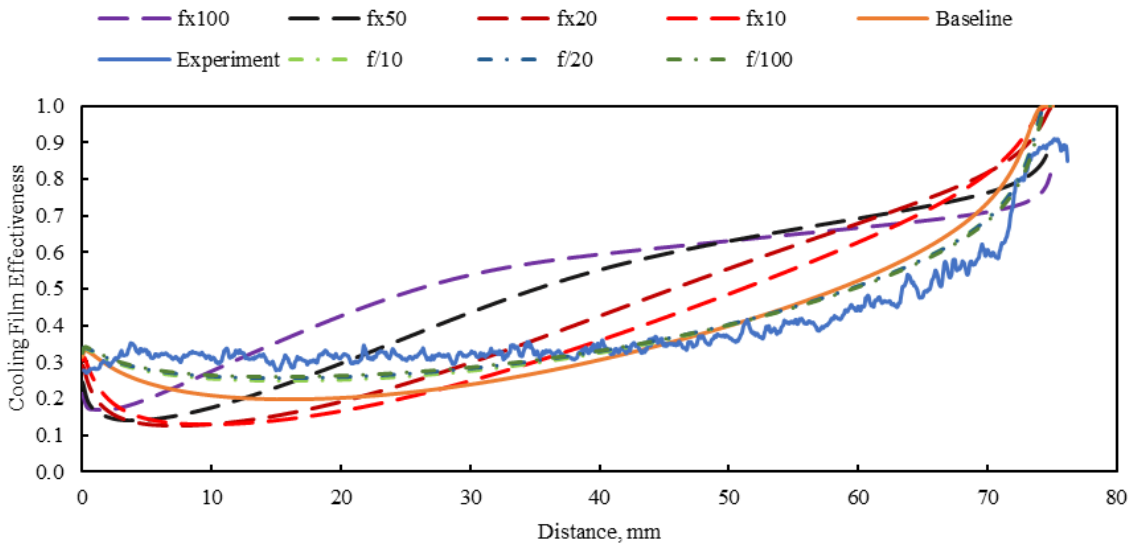

Figure 6.7 CFE_M sensitivity on porous medium inertia coefficient f, fx denoting a multiplication (increase in flow resistance) and f/ denoting a division (decrease in flow resistance). The analysis is performed on the baseline case of 20 PPI porous sample with a coolant flow rate of 30 SLPM, or BR_{FS} = 8.58E-03 [50].

Assuming isotropic porous materials, it is revealed by the sensitivity analyses that adjustments to the material property inputs to the simulations can result in better agreement between numerical simulations and experimental measurements. This is explained by either increasing the permeability or reducing the inertia coefficient, leading to less resistive samples. A comparison of K and f from different experimental studies using aluminum metal foams, showed K varying by up to four times between samples of porosities within 1% of each other and identical PPI. Whereas f varied on average by two, with the exception of one study showing two orders of magnitude smaller for their f values [48]. This supports the hypothesis that in our simulations the inertia coefficient may be too large compared to the real samples. In [48], the differences between values of different studies is justified by the multifactor determining permeability and inertia coefficient, they are compared on the basis of porosity

and PPI, however, they depend on other geometrical parameters such as fiber diameter and pore size.

Another revealing aspect of these sensitivity analyses are the results from reducing the inertia coefficient, which effectively suppresses the Forchheimer term in Eq. (5-11), resulting in the source term of the original Darcy equation. The Darcy regime is typically said to be present between a Re_K of 1-10 [44] and $Re_p < 25$ [49], see Eq. (5-12) and (5-13). Using both equations for the 20 PPI case with $\rho_{N2} = 1.138\ \frac{kg}{m^3}$, $\mu_{N2} = 17.49 \times 10^{-6}\ Pa \cdot s$ and $d_p = 0.0029\ m$ [46], results in velocity ranges of approximately $0.0462\ \frac{m}{s}$-$0.462\ \frac{m}{s}$ for Re_K and $0.133\ \frac{m}{s}$ for Re_p, for the onset of the inertial regime and Forchheimer inertial loss term to be applicable. The minimum superficial velocities for the 10 SLPM case are around $0.07\ \frac{m}{s}$, and $0.17\ \frac{m}{s}$ for the 48 SLPM case. Thus, depending on where the transition lies within these aluminum metal foams, it is possible f used is accurate but a significant part of the domain lies in the Darcy regime where the Forchheimer term should not be used.

Solving the simulations with only the Darcy loss term results in better agreement with the experiments, similar to dividing f by 100 in Figure 6.7. Simulations of all four flow rates for the 20 PPI, sample such as the comparison presented in Figure 6.5, is shown in Figure 6.8, using Darcy momentum equation instead of Darcy-Forchheimer momentum equation. Better agreement is obtained, except for the 10 SLPM case, where recirculation inside the PM occurs at the trailing edge. However, the Darcy-Forchheimer momentum equation was kept for further simulations presented in Chapters 7 and 8, as it is not confirmed if the flows are predominantly in the Darcy or inertial regime.

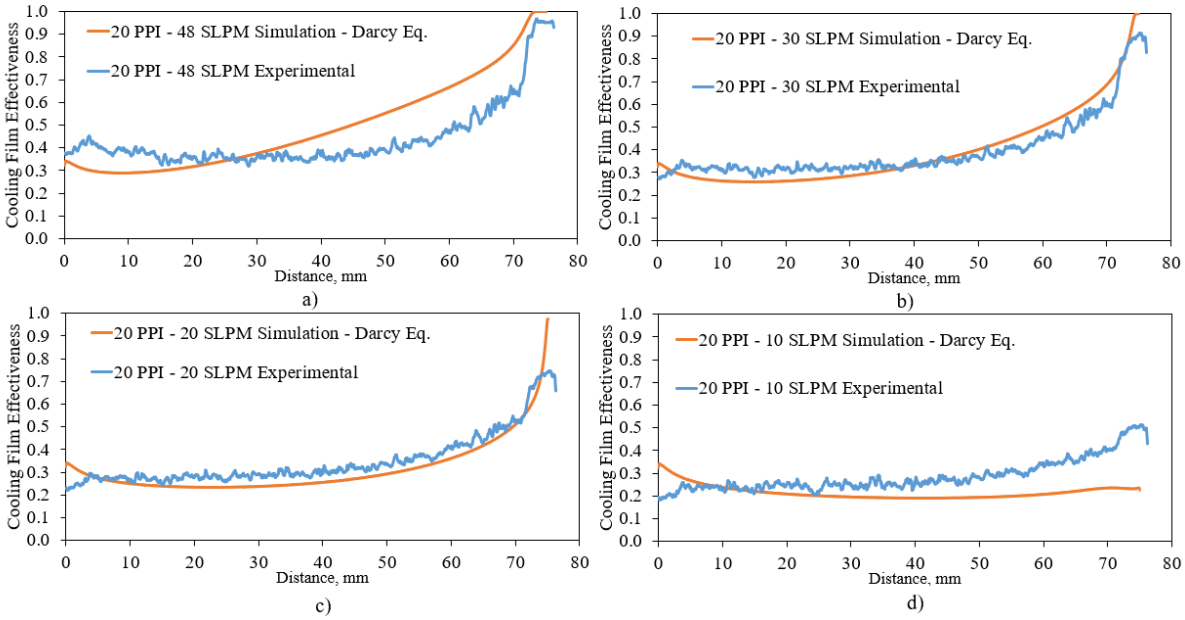

Figure 6.8 Comparisons of CFE_M values between experimental measurements and simulations using Darcy equation for the 20 PPI sample at coolant flow rates of a) 48 SLPM or BR_{FS} = 1.37E-02, b) 30 SLPM or BR_{FS} = 8.58E-03, c) 20 SLPM or BR_{FS} = 5.73E-03 and d) 10 SLPM or BR_{FS} = 2.86E-03.

7 Porous Media Design

With the sensitivity analysis performed in section 6.4 showing the effects of permeability and inertia coefficient on CFE_M, PM designs are explored in this chapter aiming to achieve ideal CFE_M. This can be defined as a constant concentration of coolant over the surface of the sample. It is hypothesized this CFE_M would produce an even heat transfer to the PM over the length of the sample, as the fluid temperature in contact with the surface would be roughly equivalent. Nevertheless, it is unlikely to produce an even temperature distribution inside the PM as other factors such as: coolant mass flux distribution, thus, local fluid heat capacity and convective heat transfer coefficient; and local conductivity coefficient in anisotropic samples have influence. These influence the propagation and removal of heat throughout the PM to different extents. The designs presented, however, aim only at achieving even coolant concentration.

7.1 Porous Media Properties

First, the sample properties of real metal foams used to produce the new designed samples are presented. These properties were taken from aluminum metal foams and compressed aluminum metal foams found in the literature [48]. Compressed aluminum metal foams have lower porosity and greater resistance to flow movement which allow for greater design range as the main factor in designed samples presented later is the resistance to flow movement. Their use also permits comparison to regular aluminum metal foams studied in chapter 4. Sample properties used in the simulations are presented in Table 7-1. All samples are from real aluminum metal foams properties except for sample 8 which is an interpolation of two foams.

Table 7-1 Aluminum metal foams physical properties [48]**.**

Sample ID		*PPI*	*Porosity*	$\boldsymbol{K(\times 10^7\ m^2)}$	$\boldsymbol{f}$
4	Not Compressed	20	0.924	0.54	0.065
5	Compressed	40	0.6	0.00924	0.383
6	Compressed	40	0.44	0.00175	0.413
7	Compressed	40	0.58	0.00606	0.471
8	Compressed	40	0.8	0.02	0.2

Aluminum would never be used as the PM material in a combustion chamber due to its low melting point. However, it is justifiable to use it as reference in this study as it aims to determine ideal surface CFE_M which is controlled by the geometrical properties of the PM: porosity, PPI, permeability, and inertia coefficient. These are uncorrelated to the thermal properties of the material.

Anisotropic profiled PM are used later in the chapter, to characterize the different combinations from Table 7-1. Ratios of porosity, permeability and inertia coefficient, are calculated using Eq. (7-1-(7-3) with the profiles presented in Table 7-2.

$$\alpha_\epsilon = \frac{\epsilon_{LE}}{\epsilon_{TE}} \tag{7-1}$$

$$\alpha_K = \frac{K_{LE}}{K_{TE}} \tag{7-2}$$

$$\alpha_f = \frac{f_{TE}}{f_{LE}} \tag{7-3}$$

With LE indicating the leading edge and TE the trailing edge, α was selected arbitrarily as variable. Likewise, the resistance ratio between trailing and leading edges can be calculated using Eq. (7-4). It was derived by dividing the trailing edge source term (Eq. (5-11)) by the leading edge source term (Eq. (5-11)).

$$\alpha_R = \alpha_f \sqrt{\alpha_K} \left(\frac{\frac{\mu_{TE}}{\rho_{TE} v_{TE} f_{TE\sqrt{K_{TE}}}} + 1}{\frac{\mu_{LE}}{\rho_{LE} v_{LE} f_{LE\sqrt{K_{LE}}}} + 1} \right) \quad \textbf{(7-4)}$$

Resistance ratios were calculated following the simulations as leading and trailing edge velocities are unknown beforehand.

Table 7-2 Property ratios of profiled PM.

Profile ID	*Leading Edge Sample ID*	*Trailing Edge Sample ID*	*Porosity Ratio,* $\boldsymbol{\alpha_\epsilon}$	*Permeability Ratio,* $\boldsymbol{\alpha_K}$	*Inertia coefficient Ratio,* $\boldsymbol{\alpha_f}$	*Resistance Ratio,* $\boldsymbol{\alpha_R}$
1	4	5	1.54	59.52	5.89	60.09
2	4	7	1.59	90.76	7.25	112.54
3	4	6	2.1	314.29	6.35	739.54
4	8	7	1.38	3.3	2.36	4.27

These ratios help compare different profiles, however, two profiles with the same resistance ratio but with different permeabilities would not give the same CFE_M curves because the flow path and distribution are also dependent on absolute resistance. The profile IDs are used to refer to designed PM from Table 7-2. Profiled PM are discussed in more details in subsection 7.2.1.1.

7.2 Porous Media Design

Before investigating methods to improve CFE_M, examples of high porosity and compressed aluminum foams are presented in Figure 7.1. As mentioned previously, low resistance to flow movement from high porosity samples cause a large amount of coolant to exit at the trailing edge, leaving the rest of the sample with little coolant. As such, uneven CFE_M occurs with low protection in the first half and very high protection in the second half. Simulation results of compressed foams with larger resistance to flow movement improve significantly on the high porosity aluminum foams by distributing coolant more evenly.

To help quantify and compare CFE_M results of two different PM, the average and standard deviation are computed. For the high porosity metal foam presented in Figure 7.1, the average CFE_M is 0.38 and the standard deviation 0.19. The compressed foam has an average CFE_M of 0.54 and a standard deviation of 0.14, an improvement over the high porosity metal foam.

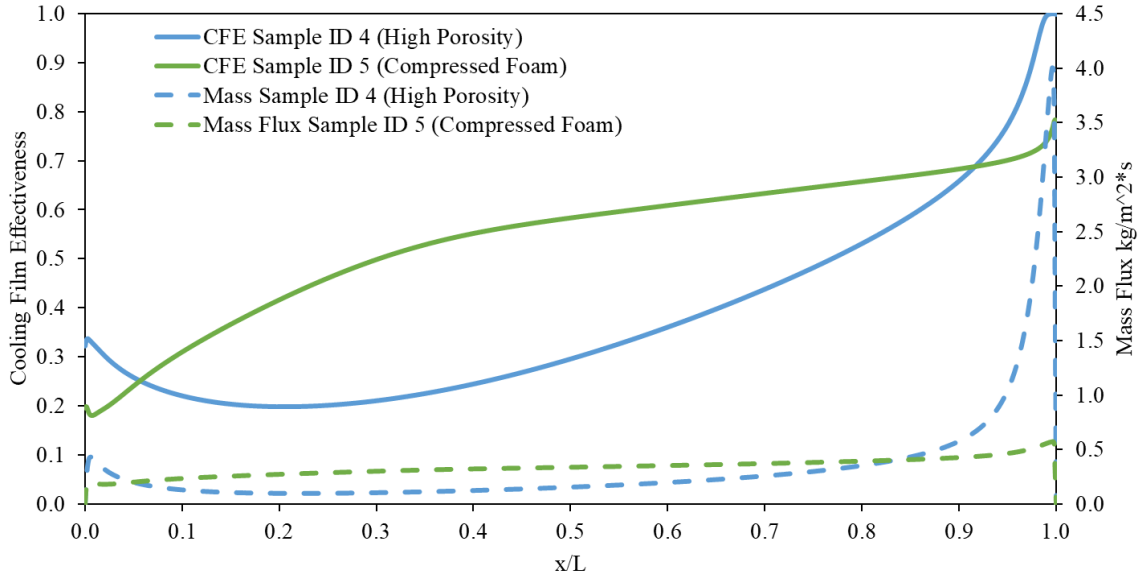

Figure 7.1 High porosity (Sample ID 4) and compressed (Sample ID 5) aluminum metal foams CFE_M and mass flux distribution for mass flow rate of 30 SLPM or BR_{FS} of 8.58E-3.

The compressed foam CFE_M results are better because high resistance to flow movement has a higher impact on the magnitude of the pressure drop across the PM relative to incremental change in velocity of the coolant, thus evening out the distribution of exiting coolant. Meaning, for every increase in velocity, the pressure gradient require to support this velocity is higher

for high resistance PM, thus encouraging more flow to distribute evenly. This means the coolant will no longer overwhelmingly exit at the trailing edge. Therefore, even distribution of exiting coolant is achievable by using very high flow resistance PM. However, they result in higher pressure drop which may prove undesirable depending on the combustion chamber design and offer uneven CFE_M as an even distribution of mass flow results in an uneven CFE_M. Note that mass flux values are taken 1 mm below the surface of the PM to prevent the capture of air present at the surface.

7.2.1 Anisotropic porous media

To achieve uniform CFE_M, more coolant needs to exit the leading edge of the PM. This could be achieved by increasing resistance to flow movement in the second half of the PM and/or reducing the resistance to flow movement in the first half of the PM, thus, requiring an anisotropic PM. The following subsections investigate various methods to achieve a uniform CFE_M using anisotropic PM.

7.2.1.1 Profiled porous media

This subsection proposes tuning the porous media properties (porosity, permeability, and inertia coefficient) to redistribute coolant towards the leading edge. This is achieved by designing a porous media with low resistance to flow movement at the leading edge and high resistance to flow movement at the trailing edge, then connecting by some function (linear, polynomial, square root, etc.) the two edges to define the resistance to flow movement in between.

The tuned porous media property values are only a function of the stream-wise direction (x direction) and are constant along the throughflow direction (y direction), i.e., the y-direction (permeability, porosity, and inertia coefficient) is equal to the x-direction permeability at any given point. The porous media properties at +dx or -dx from that point are going to be different according to the function used, but will be the same at +dy or -dy. The edge values are taken from Table 7-1 and resulting profiled (tuned) porous media are shown in Table 7-2.

Examples of the linear and square root function of the inverse of permeability over the length of the porous media for profile ID 1 from Table 7-2 is shown in Figure 7.2. Notice low inverse of permeability at the leading edge and high inverse of permeability at the trailing edge.

The inverse of permeability is a representation of the resistance offered by the Darcy term in Eq. (5-11).

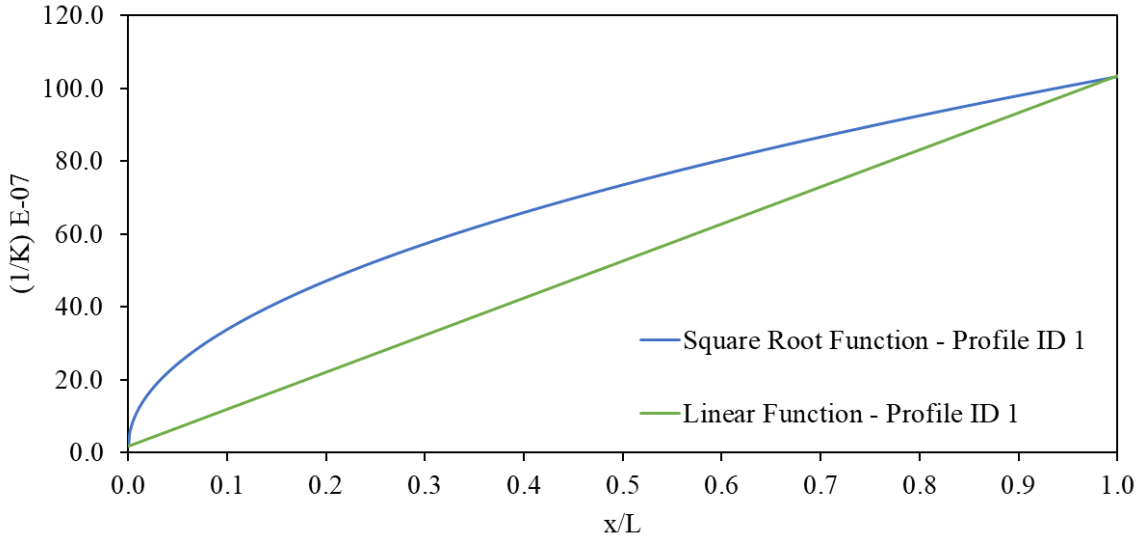

Figure 7.2 Inverse of permeability following a square root and linear function for profile ID 1, connecting the inverse of permeability of sample ID 1 at $x = 0$ and sample ID 2 at $x = L$ over the length of the sample.

Figure 7.3 compares two profiled PM with different shape functions (linear, and square root) to the isotropic compressed foam of sample ID 5 for reference. In these cases, low resistance from sample ID 4 to high resistance from sample ID 5 which represents profile ID 1 were used, giving a resistance ratio of 60.09. Both profiles result in a more uniform and higher initial CFE_M than the compressed foam. Average and standard deviation are 0.54 and 0.19, 0.56 and 0.105, and 0.56 and 0.115 for the compressed foam, squared root profile, and linear profile, respectively. Quantitative values indicate equal average CFE_M between the linear and square root profiles and slightly better standard deviation for the latter.

The redistribution of coolant is apparent in the mass flux curves of Figure 7.3, where more coolant exits the first half of the profiled samples compared to the compressed foam. Based on this comparison, future profiles in this study used a squared root function.

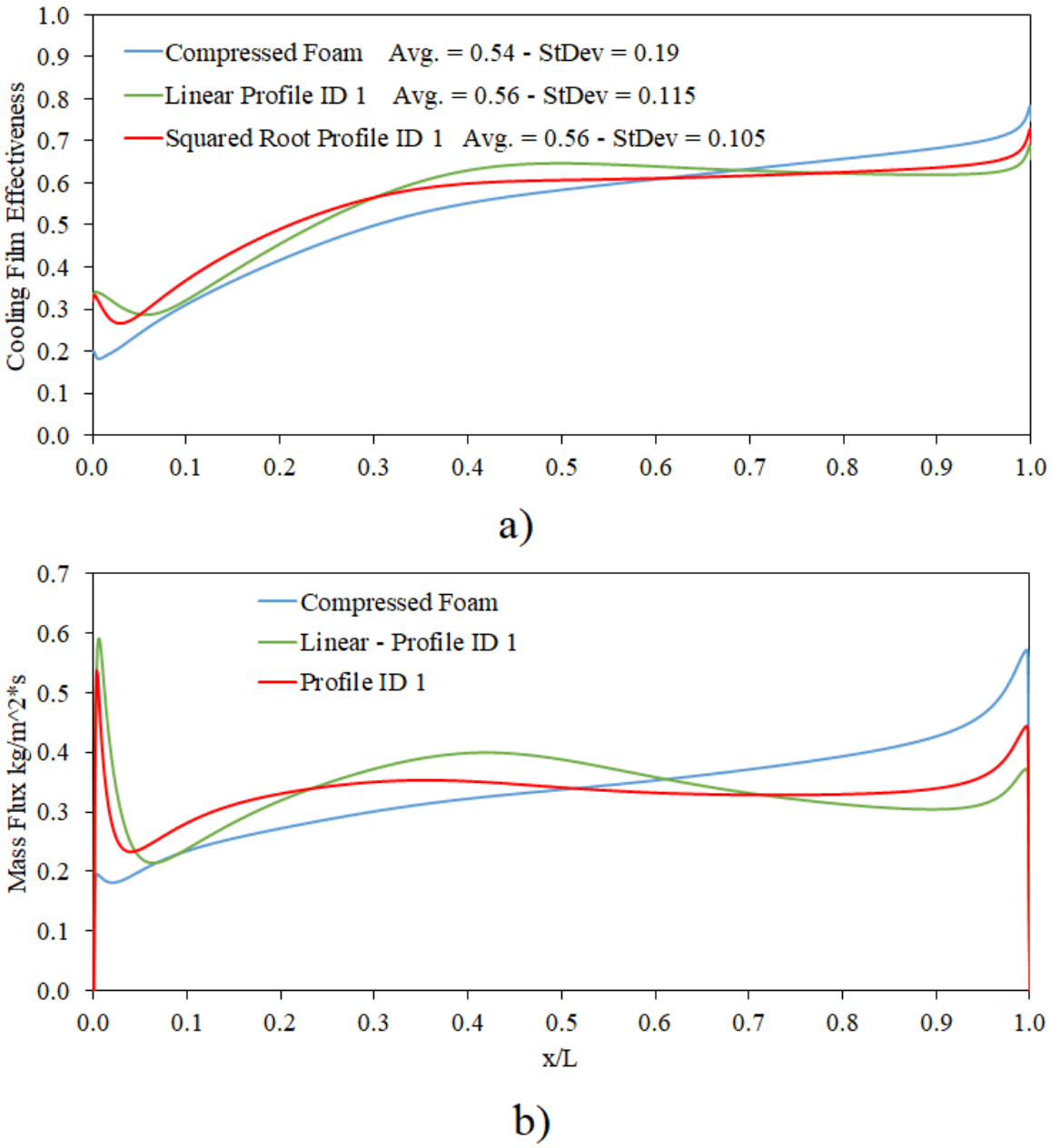

Figure 7.3 CFE_M a), and mass flux b), for a linear and square root profile of profile ID 1 (sample ID 4 to sampled ID 5) compared to a compressed foam (sample ID 5). at 30 SLPM coolant flow rate.

Square root function's smoother CFE_M over the linear function comes from the rapid increase in resistance to flow movement at the leading edge that transitions into a more gradual increase further down the PM. This allows mass flow to reduce slowly over the length of the PM, since less coolant is needed further down the sample, as discussed in section 4.2

Using various compressed aluminum foams of high flow resistance for profile IDs 1 to 3 shown in Table 7-2 resulted in significantly different CFE_M, as seen in Figure 7.4. From observation, profile ID 2 offers the smoothest protection, however, profile ID 1 and 2 lack leading edge protection which is offered by profile ID 3. Quantitative values for average and standard deviation are 0.56 and 0.105, 0.575 and 0.07 and, 0.591 and 0.05 for profile ID 1, 2 and, 3, respectively. These values would indicate profile ID 2 and 3 to offer superior protection than profile ID 1. Of importance remains the lack of protection at the leading edge. If no further designs were to be implemented, profile ID 3 would be the recommended profile as it offers protection at the leading edge. However, if improved protection to the leading edge can be achieved, profile ID 2 would be recommended as even protection is achieved past the first quarter of the PM, whereas profile ID 3 has a declining curve. Although, due to other cooling effects such as conduction in the PM and convection between the coolant and the PM, the lower concentration of coolant at the leading edge of profile ID 3 may not translate to an unacceptable temperature. The differences in CFE_M curves is directly correlated to the mass flux distribution, as shown in Figure 7.4.

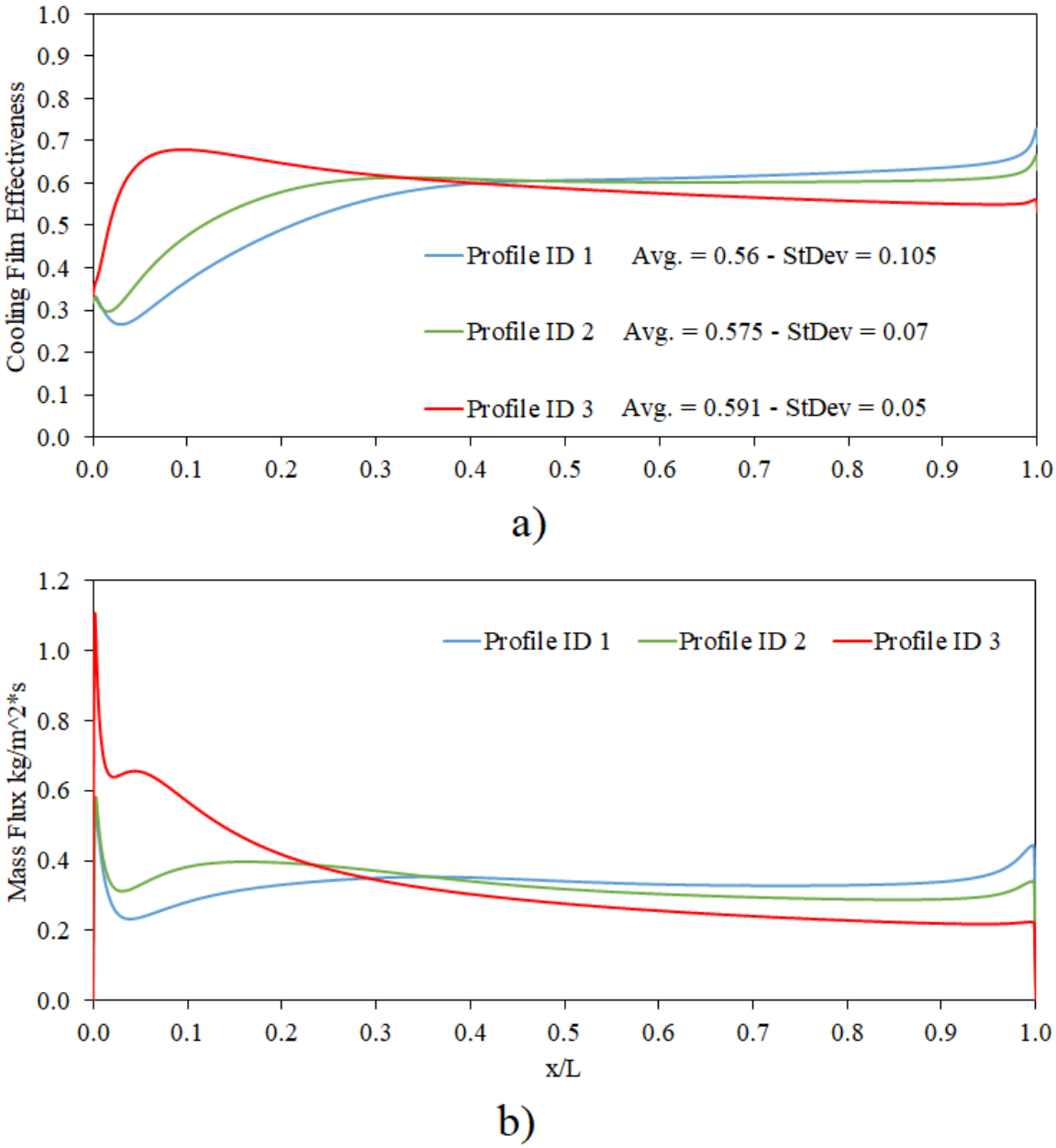

Figure 7.4 CFE_M (panel a) and mass flux distribution (panel b) for profile IDs 1 to 3 where profile ID 1 offers the lowest resistance ratio and profile ID 3 the highest resistance ratio at a coolant mass flow rate of 30 SLPM or BR_{FS} of 8.58E-3.

7.3 Leading Edge Cooling Film Effectiveness Solution

Low leading edge CFE_M indicates a lack of coolant flow rate at the leading edge of the samples, increasing it requires creating an incentive for the coolant to exit at the leading edge. Three potential solutions are investigated. One involves using a lip on the wall before the leading edge of the PM, forcing main air over the leading edge and creating a low-pressure zone, which pulls in coolant. The second proposed solution uses a small open slit before the PM which injects coolant into the channel, much like effusion cooling. The third solution removes or replaces with a high porosity PM a small section of the leading edge and uses a high resistance profiled PM afterwards. The three solutions are shown schematically in Figure 7.5, note that the lip presented in Figure 7.5a) and Figure 7.5b) is exagerated in size for easier visualization.

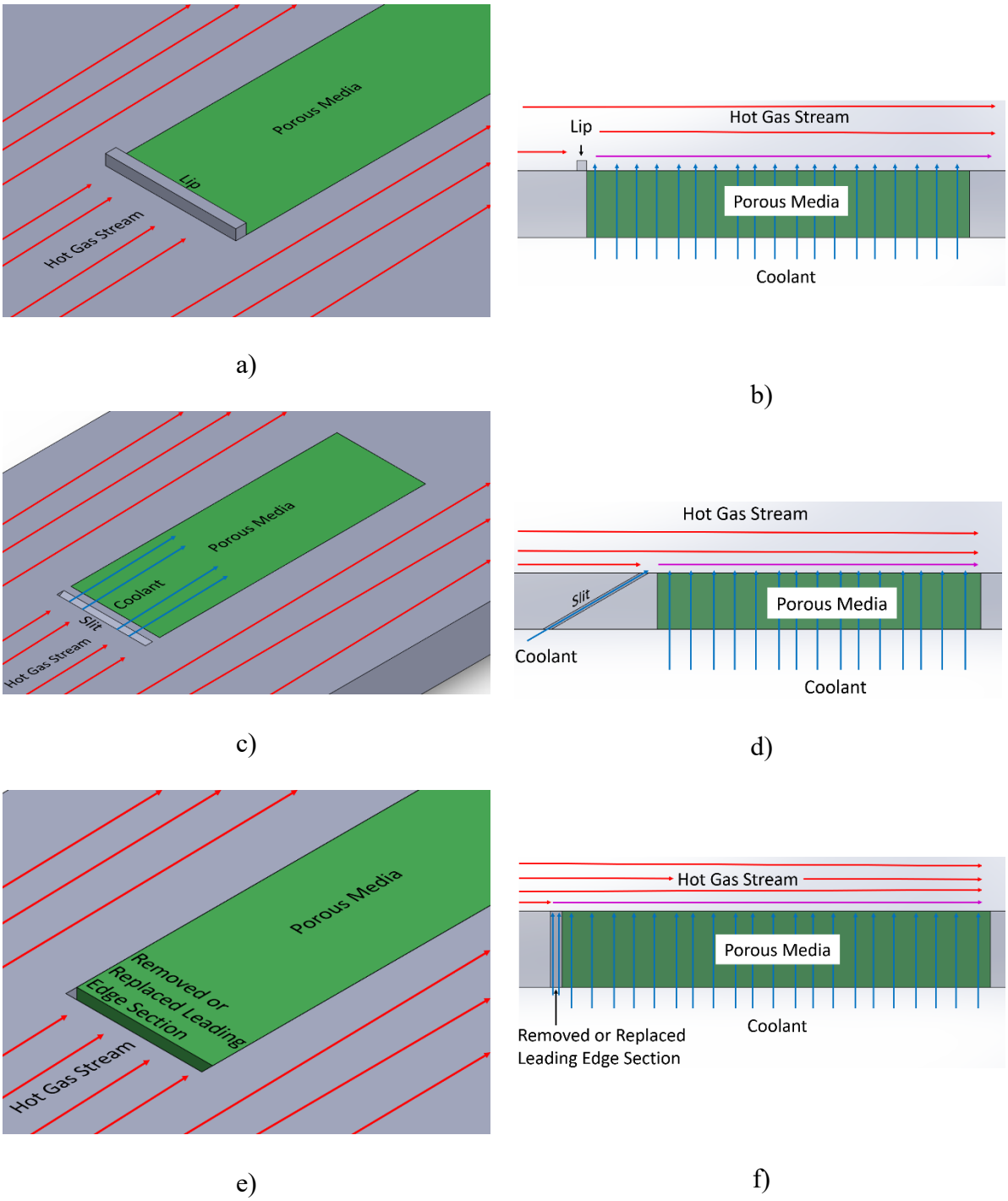

Figure 7.5 Isometric and side views of leading edge solutions investigated: using a rectangular lip (exaggerated size for easier visualization) (panels a and b), using a slit 2 mm prior to the leading edge of the porous media with a 30° exiting angle to the surface wall (panels c and d), and removing a part of the leading edge (2 mm shown) (panels e and f).

7.3.1 Leading edge wall lip

Adding a lip will prevent the main air from coming in contact with a portion of the leading edge due to being redirected away and above the PM. This creates a low-pressure zone after the lip which will pull in more coolant than it would otherwise in a case without the lip, creating a high concentration of coolant and thus high CFE_M. No recirculation is expected to occur, as a constant flow of coolant from the PM will push any fluid in this low-pressure zone into the channel. The lip investigated was square shaped and positioned directly before the leading edge of the PM. Multiple sizes were tested with results from three lip sizes shown in Figure 7.6. The modification of adding a lip to the wall was tested on Profile ID 1 as the employed porous media, as it required the largest improvement in leading edge CFE_M.

Improvements in initial CFE_M is observed in Figure 7.6a) when increasing lip size, however, using a lip size larger than half a millimeter resulted in excessive initial CFE_M relative to the CFE_M over the rest of the PM, which is undesirable as it indicates inefficient distribution of coolant. This is explained by the larger amount of coolant pulled and exiting the leading edge as the difference between the mass flux distribution between profile ID 1 without a lip to the 1 mm lip size demonstrates. Larger lips cause a larger "wake" and low-pressure area after the lip which pulls in more coolant, thus the higher exiting mass flux of coolant at the leading edge. A lip size of half a millimeter offered the best surface CFE_M out of the three sizes with high initial protection for first contact with main flow and constant protection for the rest of the PM.

The optimal size of the lip will depend on the required amount of coolant needed at the leading edge, e.g., a smaller lip would be required for profile ID 2 as its leading-edge protection already transpires more coolant than profile ID 1. Quantitative values are not presented as observations of the CFE_M was judged sufficient.

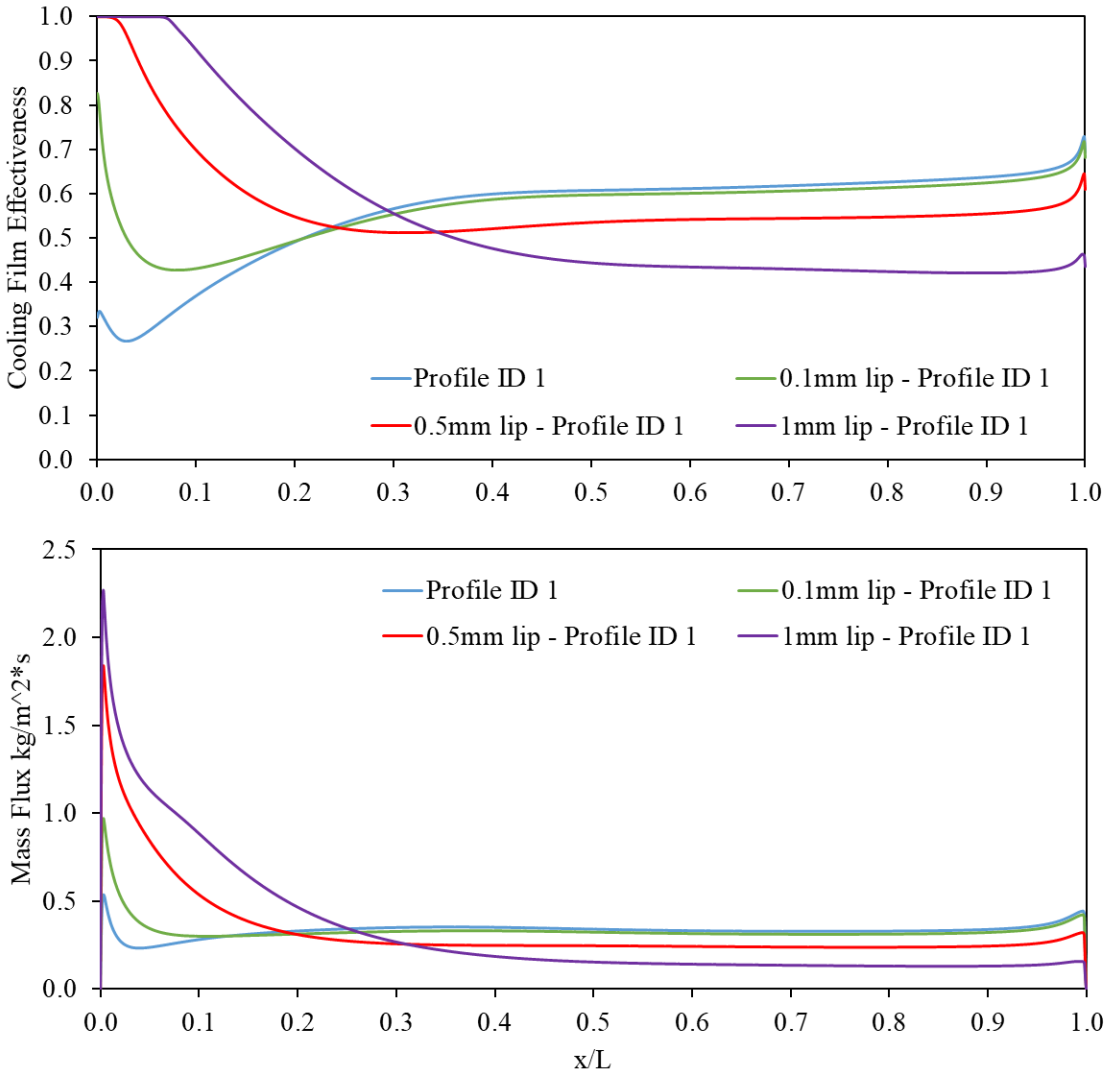

Figure 7.6 Leading edge wall lip of 1 mm, 0.5 mm, 0.1 mm, and no lip CFE_M results for profile ID 1 and coolant flow rate of 30 SLPM or BR_{FS} of 8.58E-3.

Some concerns with the feasibility of using a lip in a gas turbine chamber cannot be ignored. The lip would be subject to the same high velocity, high temperature hot gas flow as the PM, which it may not survive and become damaged or destroyed. Still, it remains interesting to consider various solutions. The square shape of the lip is also not ideal, and a smooth transition lip would be preferred.

7.3.2 Injection slit before porous media

Increasing leading edge CFE_M could be achieved by using an injection slit before the start of the PM and introducing a small amount of coolant, much like multi-hole effusion cooling. Simulations were performed where coolant was introduced 2 mm before the PM at 0.1 m/s, 0.5 m/s, 1 m/s, and 2 m/s at a 30° angle from the channel wall with a 2 mm wide injection slit. Effusion cooling injection angles are usually between 20° and 30°, thus the 30° was selected. The distance of the injection slit from the leading edge of the PM was chosen arbitrarily, though it should not be too far as to dilute the coolant film too much. Profile ID 2 was chosen as the PM as it offered the most even CFE_M in Figure 7.4. Results are presented in Figure 7.7. In these simulations the injection slit does not share coolant from the plenum.

Uniform CFE_M was achieved using this method at a velocity of 1 m/s, proving theoretically the feasibility of achieving a uniform CFE_M. As expected, increasing the velocity of coolant exiting the slit increases the leading edge CFE_M as the faster the velocity, the larger the mass flow rate. Surprisingly, increasing the slit velocity also increases the amount of coolant from the PM exiting at the leading edge, as can be seen in Figure 7.7b). This can be explained by the lower pressure at the leading edge of the PM due to a faster flow at higher injection velocity, as shown in Figure 7.8.

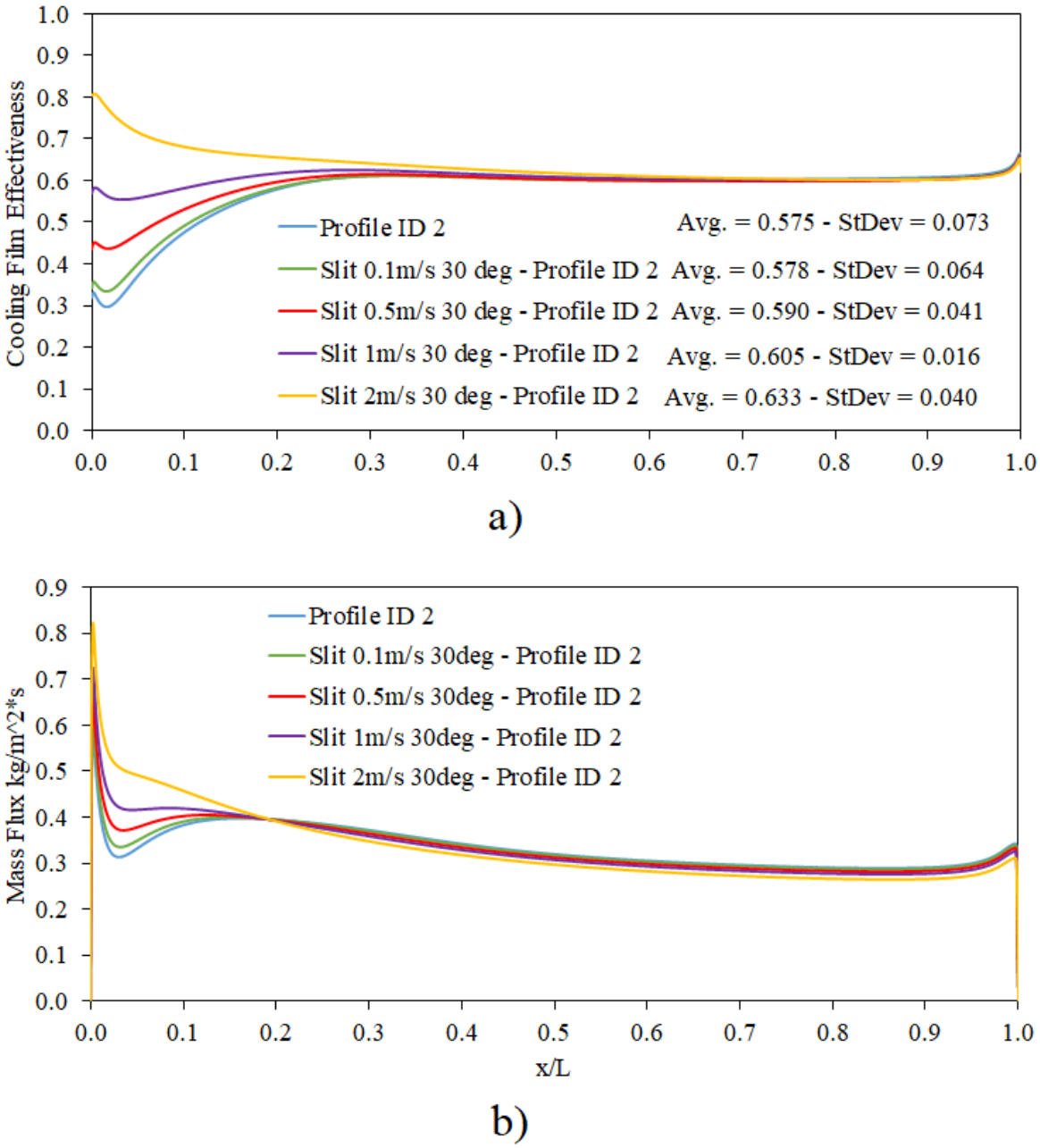

Figure 7.7 CFE_M (panel a) and mass flux (panel b) results of profile ID 2 with a 2 mm wide slit injecting coolant at 0.1 $\frac{m}{s}$, 0.5 $\frac{m}{s}$, 1 $\frac{m}{s}$, and 2 $\frac{m}{s}$ forming a 30° angle with the surface wall and located 2 mm before the leading edge. Coolant flow rate was 30 SLPM or BR_{FS} of 8.58E-3.

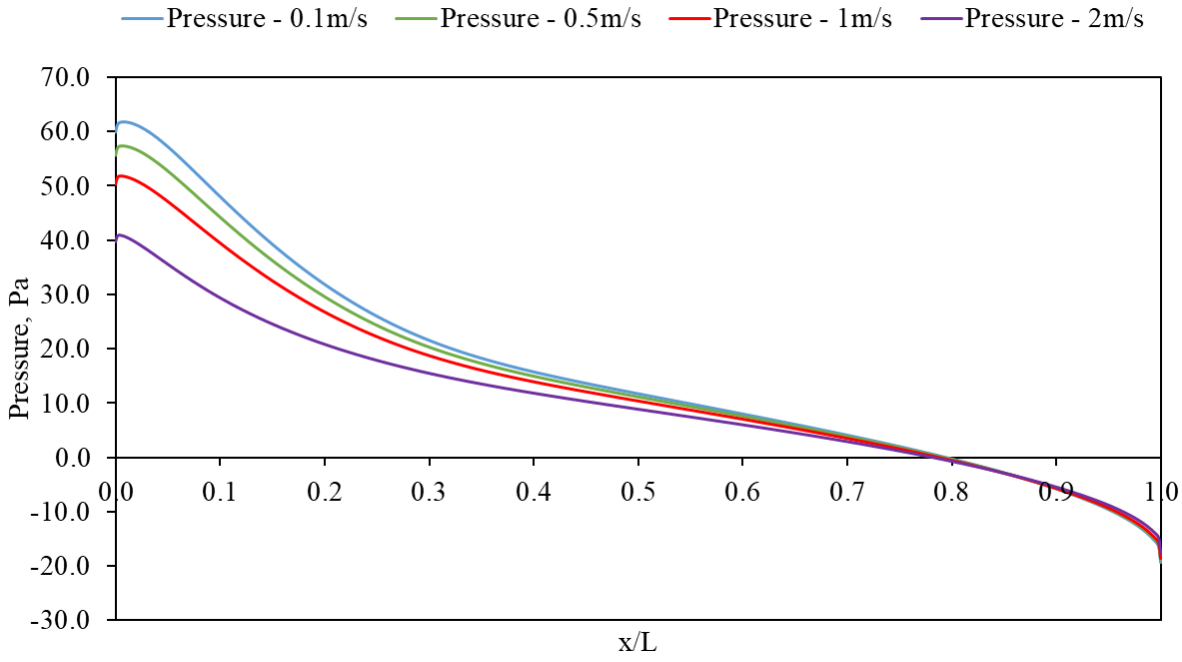

Figure 7.8 Pressure distribution on the surface of the PM for the cases with injection slit with velocities of 0.1 m/s, 0.5 m/s, 1 m/s, and 2 m/s. Profile ID 2 was the PM used and the coolant flow rate to the PM was 30 SLPM or BR_{FS} of 8.58E-3.

The CFE_M over the small 2 mm section in-between the injection slit and PM for the four velocity cases is presented in Figure 7.9. As the injection velocity increases the CFE_M of the section increases. Over the length of the section the CFE_M decreases as mixing with air dilutes the coolant. The cooling of this section may be of concern in a real application, to improve its protection the distance between the injection slit and PM could be reduced or even be zero with the injection slit ending at the leading edge of the PM.

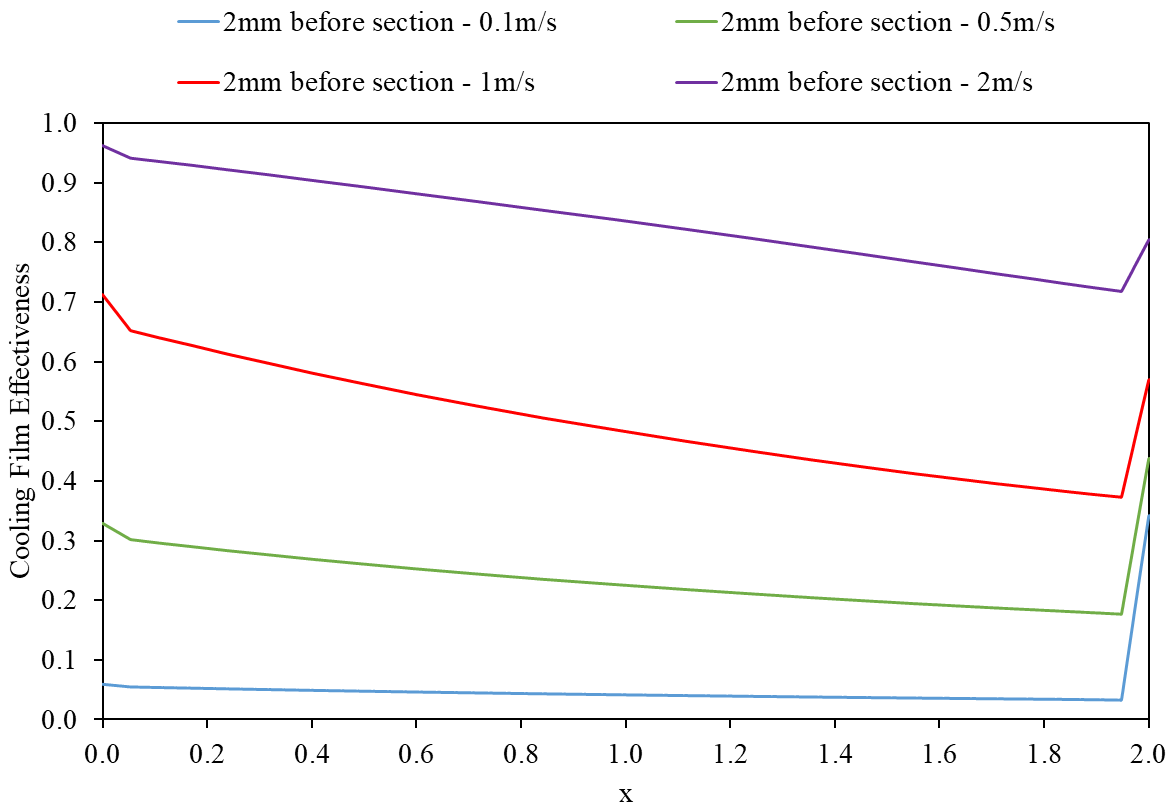

Figure 7.9 CFE_M over the 2 mm section in between the injection slit and PM for the simulation cases with injection slit at velocities of 0.1 m/s, 0.5 m/s, 1 m/s, and 2 m/s.

Due to the use of an injection slit, this method required more coolant, approximately 10% more in the case of the 1m/s velocity i.e., 33 SLPM vs 30 SLPM. Application of such method in real gas turbines may prove difficult however, as the injection slit and the PM would share the same coolant reservoir. Therefore, it may prove difficult to balance the ratio of coolant exiting the slit versus the PM. Further study on this method would be required.

7.3.3 Leading edge open section

A similar method where a small portion of the PM at the leading is removed and kept open or replaced by a low resistance PM is simulated as an alternative to the injection slit method. This is similar to the previous subsection. In the simulations performed, the PM used for the section past the leading edge is profile ID 4, a high resistance profiled PM but with a low resistance ratio. Meaning, the leading-edge resistance to flow movement of this profile is high

relative to the other profiles of Table 7-2 but the ratio between its trailing edge resistance and its leading edge resistance is smaller. In these simulations, 2 mm of the leading edge is removed or replaced and the PM used as the replacement for the leading edge is sample ID 4.

It was hypothesized that the initial section would allow enough coolant to exit and increase the leading edge CFE_M while the high resistance profiled PM section would trickle enough coolant to maintain a constant concentration. This is observed from the results presented in Figure 7.10. In this case both the removed section and the PM use the same reservoir of coolant from the plenum, removing the potential issue discussed in the previous subsection.

By observation of Figure 7.10a), a steady CFE_M curve can be seen for the great majority of the length of the PM with rapid increase in CFE_M at the leading edge for both cases. As expected, the open section case transpires more coolant at the leading edge than the case with a low resistance section. The first 2 mm of the PM with leading edge solution are not shown for the CFE_M figure as we are not concerned with their cooling, since if such a solution were to be implemented, the top section would be open space where no heat transfer to the PM could occur.

More simulations were performed where more or less of the leading edge was removed/replaced, e.g., 1 mm or 5 mm, which increased the amount of coolant leaving at the leading edge when a larger portion is removed/replaced and vice-versa.

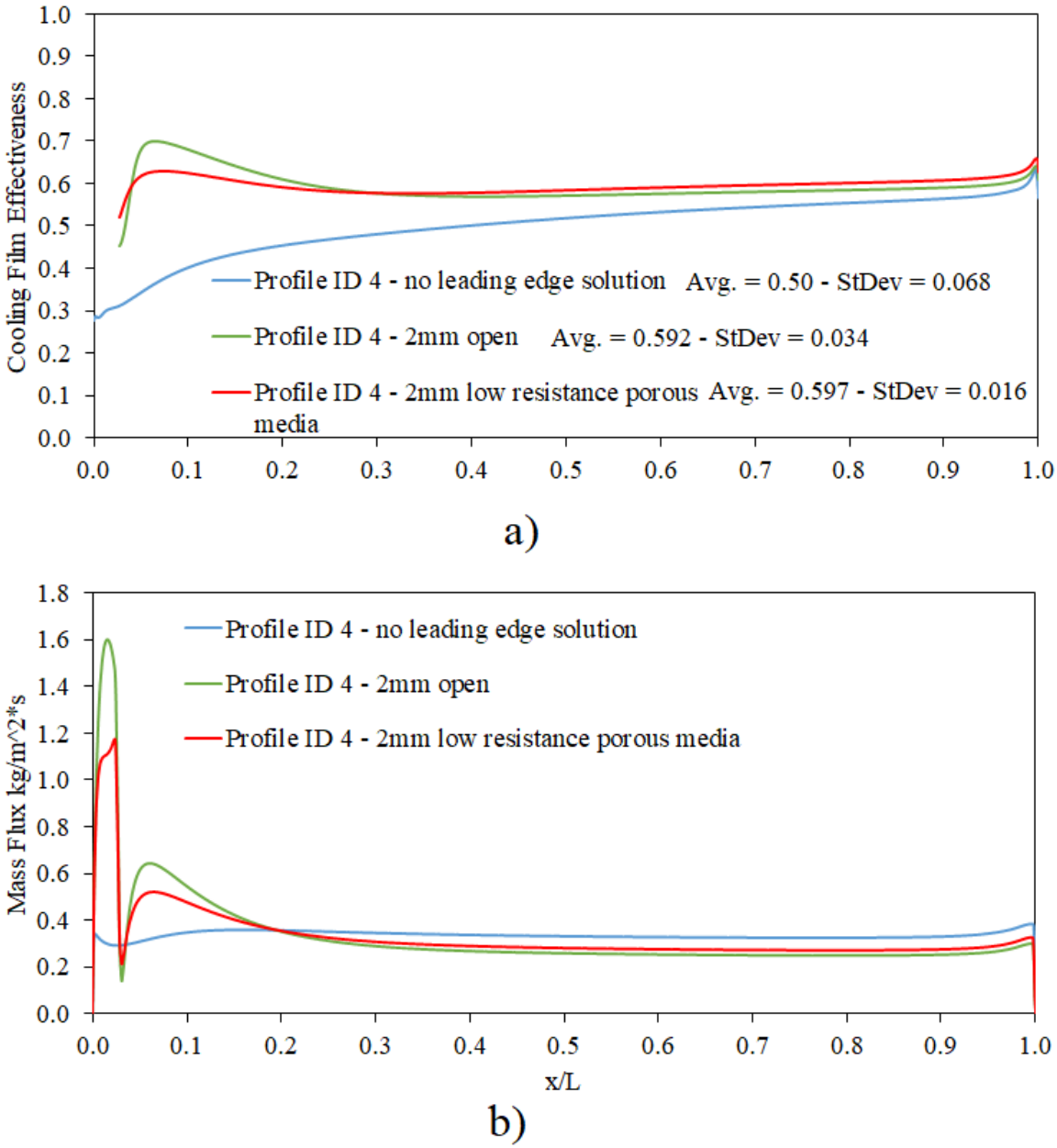

Figure 7.10 CFE_M (panel a) and mass flux (panel b) results of removed and replaced leading edge with profile ID 4 for the high resistance PM for coolant flow rate of 30 SLPM or BR_{FS} of 8.58E-3.

7.4 Porous Media Dimension Effects on Cooling Film Effectiveness

Thus far, all simulations have been performed on a PM of 13 mm in thickness and 75 mm in length. As one would expect, changing the dimensions may result in different CFE_M curves, which would indicate dependance on dimensions. This is investigated in the current section where dimension changes to the PM of the previous subsection (7.3.3) are made: doubling the length, doubling the thickness and, doubling both the length and the thickness. In cases where the length of the PM is doubled, the coolant mass rate is increased to reflect the increase in surface area, keeping the BR_{FS} constant.

Profile ID 4 is used as good results were obtained in the previous subsection. In the case where the length is doubled, the open section is also doubled to reflect the same profile ratio per nondimensional distance $\frac{x}{L}$. Results for the four dimension cases are presented in Figure 7.11.

Cases where the length of the PM was increased resulted in higher overall CFE_M curves, largely attributed to a larger accumulation of coolant, thus thickening of the boundary layer, as shown in Figure 7.12. Case where the thickness of the PM was increased saw a shift of mass flux from the trailing edge to the leading edge, causing an increase in leading edge CFE_M and lower trailing edge CFE_M. This effect was expected as increasing the thickness increases the required pressure drop for coolant to exit in the higher resistance region of the porous media more than the lower resistance region, discouraging coolant from exiting closer to the trailing edge.

Increasing the length of the PM resulted in lower leading edge mass flux because a longer PM creates more surface length resistance, encouraging more coolant to transpire closer to the trailing edge. Increasing the thickness of the PM increases the resistance to flow movement more at the trailing edge than it does at the leading edge, therefore, more coolant exits at the leading edge. This results in significantly larger initial CFE_M and lower CFE_M for the remainder of the PM.

It can thus be concluded that the profiles need to be adjusted when applied to different dimensions: slightly larger resistance ratio when increasing the length and smaller resistance ratio when increasing the thickness.

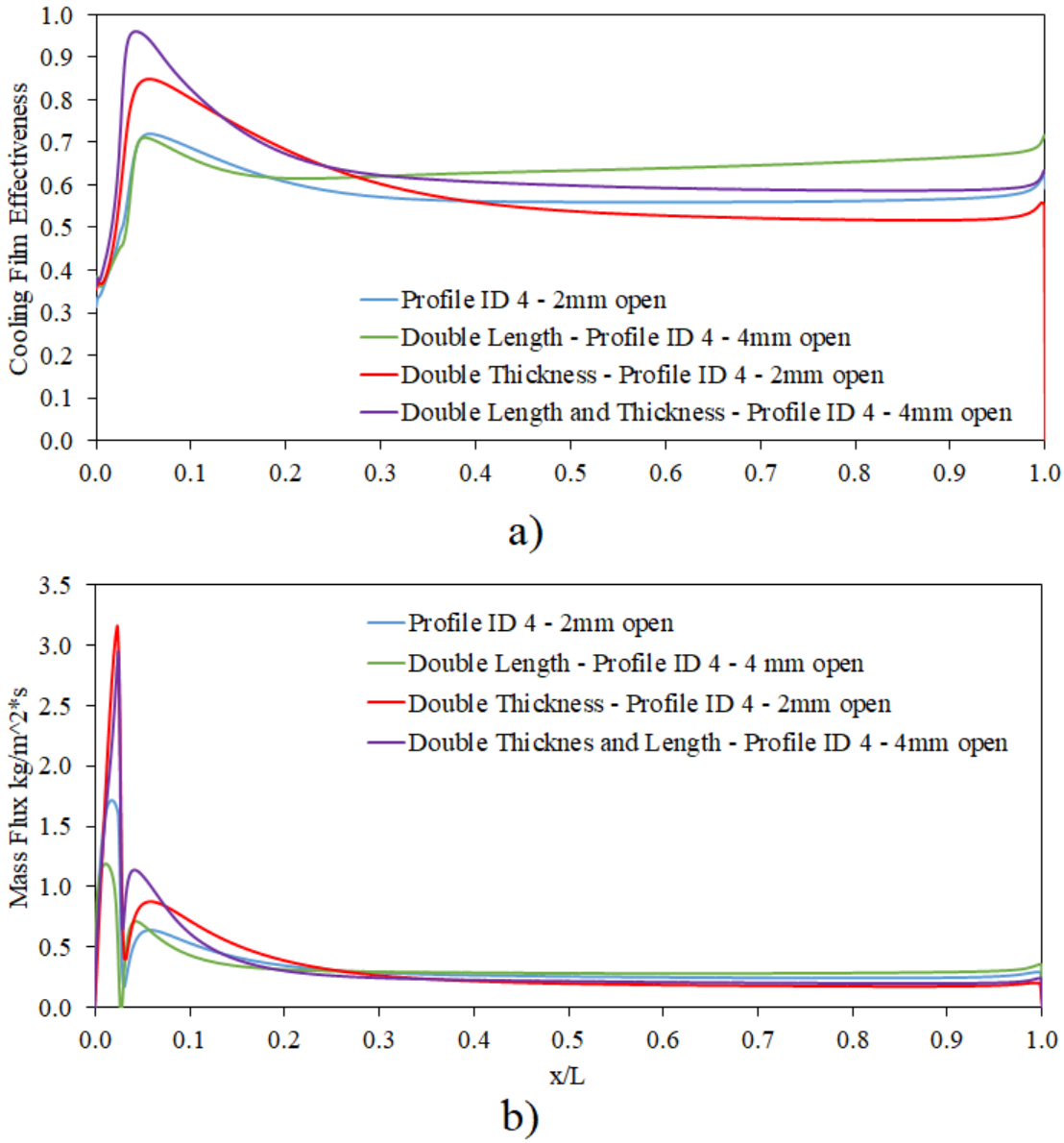

Figure 7.11 CFE_M (panel a) and mass flux (panel b) for double length, double thickness, and double thickness and length based on profile ID 4. Double length simulations have a 4 mm open section versus the regular length 2 mm. Flow rate was 30 SLPM or BR_{FS} of 8.58E-3.

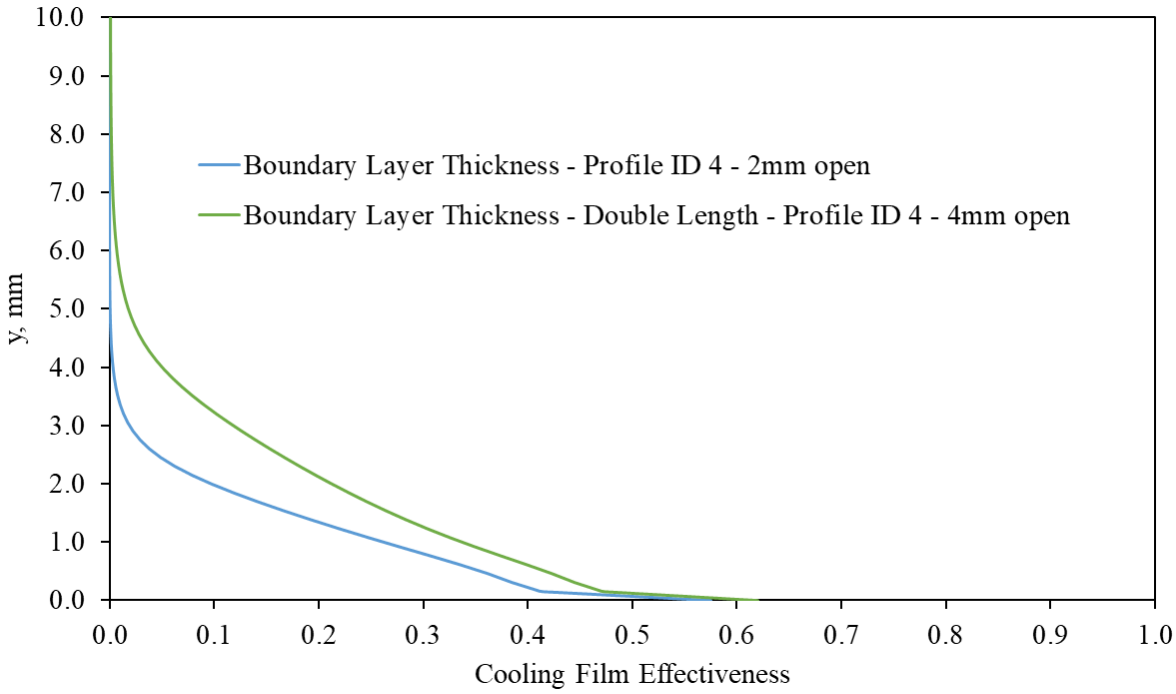

Figure 7.12 Boundary layer thickness of the cooling film for the profile ID 4 PM of "regular" size with 2 mm open leading edge section and the profile ID 4 double length with 4 mm open leading edge section at x/L = 0.3 for each. Meaning the boundary layer is taken at x = 0.5675 m for the "regular" size PM and x = 0.59 m for the double length PM.

8 Heat Transfer Analysis

In previous chapters, CFE protection measured using mass transfer analogy offered by PM have been made more uniform by modifying the PM properties and changing the distribution of coolant. In this chapter, comparisons of the surface temperature for different PM seen so far such as high porosity aluminum foams of the experiments, compressed aluminum foams, profiled porous media, and profiled porous media with leading edge solution, are performed. The heat transfer condition is simulated with the main flow at higher temperature than the coolant. The goal is to compare the CFE_M to the CFE_T and determine if CFE_M is an appropriate representation of CFE_T. The heat transfer model is presented first, followed by a validation analysis based on experimental data found in the literature and finally, the heat transfer simulations of profiled PM are performed.

8.1 Heat Transfer Model

The heat transfer model is described here. Two main heat transfer processes need to be modeled: heat transfer inside the PM which includes convection between the solid ligaments and coolant and conduction through the solid phase, described in subsection 8.1.2, and second, heat transfer between the hot gas flow and the PM's surface with cooling film effects, described in subsection 8.1.3. The radiative heat transfer inside the PM is neglected as it is assumed the temperature differences are to be small. Radiative heat transfer to the surface of the PM is also neglected even though in real gas turbine combustion chambers the radiation has an effect. The reason is to simplify the problem and enable future comparison of experiments. This assumption will result in lower overall heat transfer to the PM and lower PM surface temperatures.

8.1.1 Calculation Domain

As mentioned in section 5.4, Fluent Academic version was used to perform numerical simulations, which imposes a limit on meshes to a maximum of 512,000 cells. To solve the heat transfer inside the PM, local non-thermal equilibrium is assumed (LNTE). LNTE is the assumption that the fluid and solid phases of the PM in a cell are not at the same temperature.

This is usually true around the surface of the PM when there is large heat transfer to the PM and the convection from the coolant to the solid of the PM is not large enough to reach thermal equilibrium. The LNTE thus requires solving the first law for both the solid and fluid phases and they both carry their own equation. The mesh must reflect this by separating the PM into two domains, one for the fluid phase and one for the solid phase. This causes the number of cells in the PM to double and when using element sizes of 0.1 mm this brings the total count of elements above the threshold of 512,000 cells. To return below the available limit, the element size was increased to 0.15 mm in the higher resolution zones. A bias of 100 was also applied inside the porous media, more detail on the selected mesh is presented in subsection 8.2.3.

8.1.2 Heat transfer inside porous media

Heat transfer inside PM can be derived from the first law of thermodynamics. Two different models exist depending on the assumption that the phases (solid and fluid phases of the PM) are either in thermal equilibrium, resulting in the local thermal equilibrium model (LTE), or that they are not in thermal equilibrium, thus the local non-thermal equilibrium model (LNTE). In the simulations performed later in the chapter, it was assumed that the solid and fluid phases are not in thermal equilibrium, thus the LNTE model was used, requiring to solve the first law for both phases. The assumption of non-thermal equilibrium is justified by the large heat transfer occurring at the surface of the PM due to convection from the hot gas flow.

The first law for the solid phase is presented in Eq. (8-1), the derivation can be found in Appendix A - Heat Transfer Analysis or [65].

$$(1-\epsilon)\rho_s c_s \frac{\partial T_s}{\partial t} = \nabla \cdot (k_{se} \nabla T_s) + h_i\left(T_f - T_s\right) \tag{8-1}$$

where c_s is the specific heat capacity of the solid, k_{se} the effective conductivity of the solid, T_s the temperature of the solid, T_f the temperature of the fluid and h_i the interfacial convective heat transfer coefficient between PM ligaments and coolant. The term on the left-hand side measures the rate of change of energy in the element. The first term on the right-hand side measures the conduction in and out of the element and the second term on the right-hand side is the convective heat transfer between the solid and fluid phases.

The first law for the fluid phase is presented in Eq. (8-2), the derivation can be found in Appendix A - Heat Transfer Analysis or [65].

$$\epsilon \rho_f c_{p,f} \left(\frac{\partial T_f}{\partial t} + \frac{1}{\epsilon} v \cdot \nabla T_f \right) = \nabla \cdot \left(k_{fe} \nabla T_f \right) + h_i \left(T_s - T_f \right) \tag{8-2}$$

where $c_{p,f}$ is the specific heat capacity of the fluid at constant pressure, and k_{fe} the effective conductivity of the fluid. The second term on the left-hand side of the equation representes the convection of energy through the element, the other terms are the same as Eq. (8-2).

Both equations are coupled by the last term on the right hand side, representing convective heat exchange between the solid PM and the surrounding fluid.

When solving using finite volume method (FVM) such as in Fluent, modifications to the conductivity coefficient and heat transfer coefficient are made to represent the volume-average approximation. For thermal conductivity, the heat flux through a PM can usually be approximated by multiplying the material's thermal conductivity with the ratio of solid volume to total volume, (1-ϵ), as in the following equation [30]:

$$k_{se} = (1 - \epsilon) k_s \tag{8-3}$$

where k_s is the thermal conductivity of the solid. Accordingly, the effective fluid thermal conductivity, k_{fe}, is calculated as follows:

$$k_{fe} = \epsilon \cdot k_f \tag{8-4}$$

where k_f is the thermal conductivity of the fluid.

Heat transfer between the ligaments and the fluid is approximated by a volumetric convective heat transfer coefficient which is calculated with equation (8-5). The temperature difference between the solid and fluid in each cell is then used to calculate the heat transfer [30].

$$h_v = a_{sf} \cdot h_i \tag{8-5}$$

where a_{sf} is the specific surface area between solid and fluid phase, hence subscript sf, calculated by:

$$a_{sf} = \frac{A}{V} \tag{8-6}$$

where A is the internal surface area of the solid in the PM, and V the volume occupied by the PM. For high porosity metal foams, two empirical equations exist to determine the specific surface area [47],[66]. Equation (8-7) from [47] is used to approximate samples from which a_{sf} was not available in the literature.

$$a_{sf} = \frac{3\pi d_f}{\left(0.59 d_p\right)^2}\left[1 - e^{-\frac{(1-\epsilon)}{0.04}}\right] \tag{8-7}$$

where d_f is the average fiber diameter, fibers being the ligaments connecting the nodes inside the PM. Correlations also exist to determine the interfacial convective coefficient h_i for high porosity metal foams [47], [67]–[71]. Equation (8-8), from [47], was used and is shown below.

$$Nu_{sf} = \frac{h_i d_f}{k_f} = C_T Re_{d_f}^{0.5} Pr^{0.37} = C_T \left(\frac{u \rho_{\mathrm{f}} d_f}{\epsilon \mu_{\mathrm{f}}}\right)^{0.5} Pr^{0.37} \qquad (C_T = 0.52) \tag{8-8}$$

where Nu_{sf} is the Nusselt number between solid and fluid phase, Pr the Prandlt number of the fluid, and C_T an empirical coeffcient which was determined to be 0.52 for high porosity aluminum metal foams [47]. Equations (8-7) and (8-8) are used for high porosity metal foams, i.e. >90% porosity. For samples with lower porosities, the following correlations are used [30][72].

$$a_{sf} = \frac{6(1-\epsilon)}{d_p} \tag{8-9}$$

$$Nu_{sf} = (0.933\epsilon^2 - 0.245\epsilon + 0.0165) Re_p^{0.8} \cdot Pr^{\frac{1}{3}} \tag{8-10}$$

Plotting a_{sf} multiplied by the polynomial of porosity in the parentheses of Eq. (8-10) yields the distribution shown in Figure 8.1. This offers a proxy of h_v based on the correlations of Eq. (8-9) and (8-10). A maximum volumetric heat transfer coefficient is reached at porosities around 70%, and minimums at around 15% and approaching 100%. The porosity polynomial

was determined in [72] for sintered microporous media with all experiment value falling within 35% of predicted values.

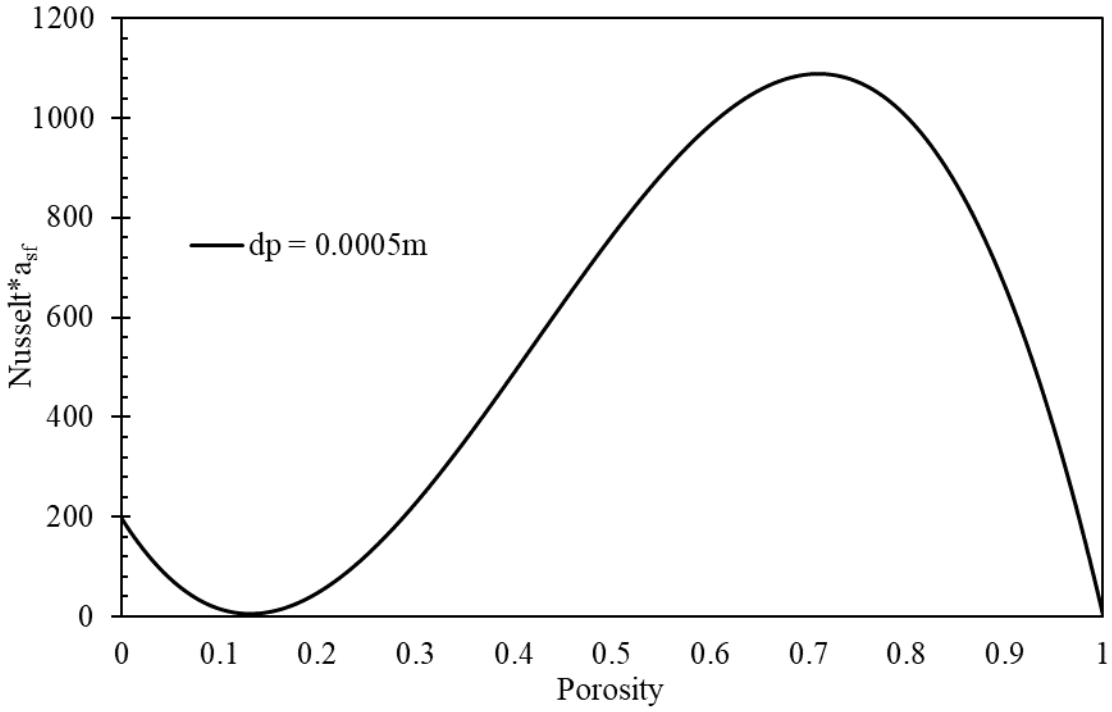

Figure 8.1 Distribution of a_{sf} multiplied by the polynomial of porosity in Eq. (8-10) for $d_p = 0.0005m$. A proxy for the volumetric heat transfer coefficient h_v.

8.1.3 Boundary conditions

Boundary conditions for the heat transfer problem are established here, with a schematic of the problem presented in Figure 8.2, where Ψ denotes boundaries. The walls Ψ_W boundary conditions are assumed to be adiabatic to simplify the problem, as any heat transfer coming from the walls in a real-life case is expected to be negligible compared to the heat transfer from the hot gas.

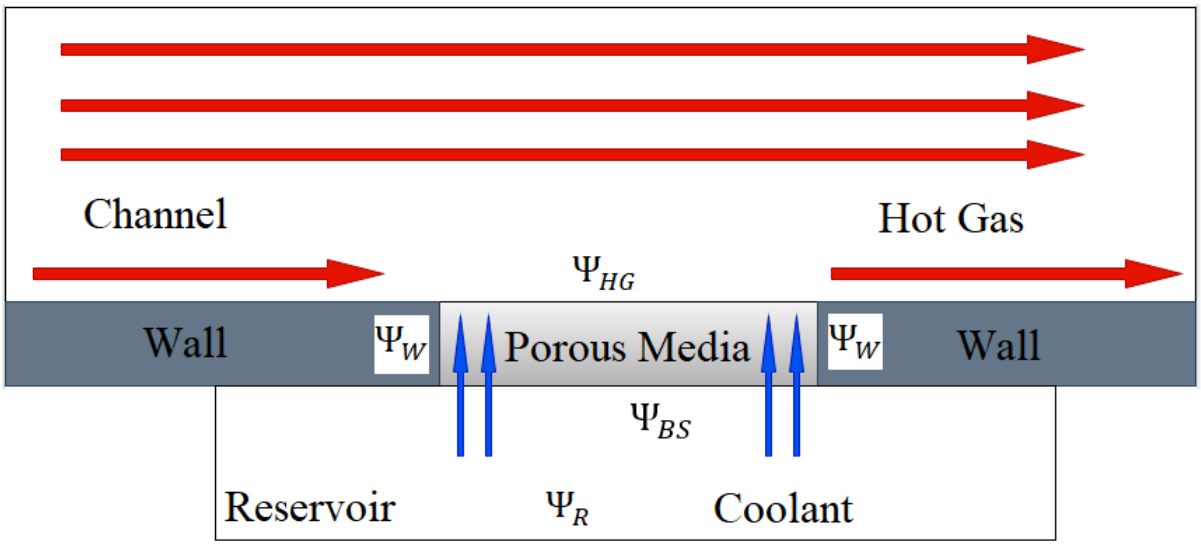

Figure 8.2 Schematic of Transpiration cooling domain with heat transfer.

In Figure 8.2, a boundary for the back side of the PM, Ψ_{BS}, and one for the reservoir, Ψ_R, are shown. These represent two possible coolant inlets, depending on whether the reservoir is modeled or not. In section 8.2, the validation model does not include the reservoir as per [31], therefore the coolant inlet boundary is Ψ_{BS}. In section 8.3, where comparisons of PM studied in this thesis are performed, the reservoir is included, therefore the coolant inlet is imposed on boundary Ψ_R. Mass flux and temperature of the coolant entering the reservoir or PM must be known and used as boundary condition on Ψ_R or Ψ_{BS}.

The heat transfer between the surface of the PM and surrounding fluid, Ψ_{HG}, can be approximated by the following sets of equations [17]:

$$q_w = h_s(T_{ge} - T_w) \tag{8-11}$$

where q_w is the heat flux applied on the surface of the PM in contact with the channel, h_s is the surface convective coefficient between the surface PM temperature T_w and hot gas effective temperature T_{ge}. For relatively low hot gas flow velocities, (Mach number < 0.3), the static temperature of the hot gas can be used, however, for flows with Mach number larger than 0.3, the recovery or total temperature is to be used as effective temperature T_{ge}.

When solving using FVM, q_w is applied to the boundary of the solid PM cells. Thus, the solid phase surface area of the PM needs to be taken into consideration. Since it is smaller than the full surface area that includes the pores and solid ligaments, it will reduce the total heat transfer. The solid phase surface area of the PM is approximated by the full area multiplied by the porosity [44]. Equation (8-11) becomes Eq. (8-12), and q_w is renamed $q_{w_{FVM}}$. It represents the heat flux applied to the cells on the boundary Ψ_{HG} of the solid phase of the porous media. Since the units of q are $\left[\frac{W}{m^2}\right]$, only the ratio of solid phase surface area to total surface area $(1-\epsilon)$ is added.

$$q_{w_{FVM}} = (1-\epsilon)\cdot h_s\left(T_{ge} - T_w\right) \tag{8-12}$$

To determine h_s, derivations found in [17] and [18] for a simplified Couette-flow model of the turbulent boundary layer in the general case of transpiration cooling are used.

The derivations from [17] and [18] relate the Stanton number of zero blowing condition, a condition with no transpiration cooling, to the condition with transpiration cooling. The Stanton number of the condition without transpiration cooling can easily be found from empirical equations. The Stanton number is a dimensionless number that measures the ratio of heat transferred into a fluid to the thermal capacity of fluid. The ratio of the Stanton number with transpiration cooling the Stanton number with zero blowing condition is calculated with the following equations [17]:

$$\frac{St}{St_O} = \frac{\frac{BR}{St_O}}{e^{\frac{BR}{St_O}} - 1} f1 \tag{8-13}$$

where St is the Stanton number with subscript O indicating zero blowing condition, and $f1$ a correction factor calculated with Eq. (8-14) [17].

$$f1 = \left[\frac{\left(e^{\frac{BR}{St_O}} - \frac{1}{\eta'}\right)}{\left(e^{\frac{BR}{St_O}} - 1\right)} + \frac{\left(\frac{1}{\eta'}\right)}{\frac{BR}{St_O}}\right]^{-1} \tag{8-14}$$

where η' is the thermal effectiveness calculated by Eq. (2-6). A full utilization of coolant thermal capacity is obtained when η' equals 1 or $T_{ce} = T_w$. Correction factor $f1$ has considerable importance for low values of $\frac{BR}{St_O}$ and represents the effect of the thermal effectiveness on the reduction in heat transfer between the hot gas and PM surface [17].
The Stanton number ratio from [18] uses a slightly modified equation:

$$\frac{St}{St_O} = \frac{\frac{BR}{St_O} r}{e^{\frac{BR}{St_O} r} - 1} \tag{8-15}$$

where r is the ratio of temperature drop across the laminar sub-layer and the temperature drop across the entire boundary layer [23], and can be related to the velocity profile [18], and calculated as follows:

$$\mathrm{r} = \frac{2.11}{\mathrm{Re}^{0.1}} \tag{8-16}$$

where Re is the Reynolds number over a flat plate. It is unknown if Eq. (8-16) applies to Reynolds number of turbulent flows in pipes and clarifications were not found. However, it is assumed to be applicable and a reasonable approximation, but may introduce a source of error.

The Stanton number for zero blowing condition can be determined by use of the empirical equations for Nusselt number of fully developed turbulent flow in a smooth duct of appropriate ranges of Pr and Reynolds number Re_{DH}.

$$Re_{DH} = \frac{\rho v D_h}{\mu} \tag{8-17}$$

where $D_h = \frac{4 \cdot A}{P}$ is the hydraulic diameter with A the area and P the perimeter of the channel. Two empirical equations are used to determine the Stanton number as two different Re_{DH} are simulated in sections 8.2 and 8.3, with correlations Dittus-Boetler Eq. (8-18) and Gnielinski Eq. (8-19), respectively. The Reynolds number for pipe flow is calculated using Eq. (8-17).

$$Nu_{DH} = 0.023 R_{e_{DH}}^{0.8} Pr^{0.4} \quad \textbf{(8-18)}$$

where Nu_{DH} is the Nusselt number for turbulent flow inside a pipe.

$$Nu_{DH} = 0.0214(Re^{0.8} - 100)Pr^{0.4} \quad \textbf{(8-19)}$$

The zero-blowing condition Stanton number is then determined with equation (8-20) and used with the correlations of Eq. (8-13) and (8-14) or (8-15) and (8-16) to approximate the convective heat transfer coefficient on the surface of the PM.

$$St_{DH} = St_O = \frac{h_O}{\rho v c_p} = \frac{Nu_{DH}}{Re_{DH} Pr} \quad \textbf{(8-20)}$$

Zero-blowing condition convective heat transfer coefficients were calculated prior to simulations and are shown in Appendix A - Heat Transfer Analysis.

As mentioned previously in subsection 2.3.2, two mechanisms are responsible for the reduction of heat transfer from the hot gas flow to the PM surface: advection away from the wall and reduction in boundary layer temperature [23]. It is assumed the heat transfer coefficient calculated using either Eq. (8-13) or (8-15) estimates the effects of advection [23]. To approximate the effects in the reduction of boundary layer temperature, T_{ge} in Eq. (8-12) is replaced by the fluid temperature in the cell directly above the boundary separating the PM and channel, and labeled T_{HG}. Therefore, Eq. (8-12) becomes:

$$q_{w_{FVM}} = (1 - \epsilon) \cdot h_s (T_{HG} - T_w) \quad \textbf{(8-21)}$$

This method was also proposed in [14], where T_{HG} is presented as $T_{\text{gas reference}}$ in Figure 8.3. Of course, using the temperature value in the cell directly above the wall is an approximation that is likely to be lower than $T_{\text{gas reference}}$. It was, however, nonetheless decided to apply this approximation due to the difficulty of implementing an average boundary layer temperature using Fluent user defined functions (UDF).

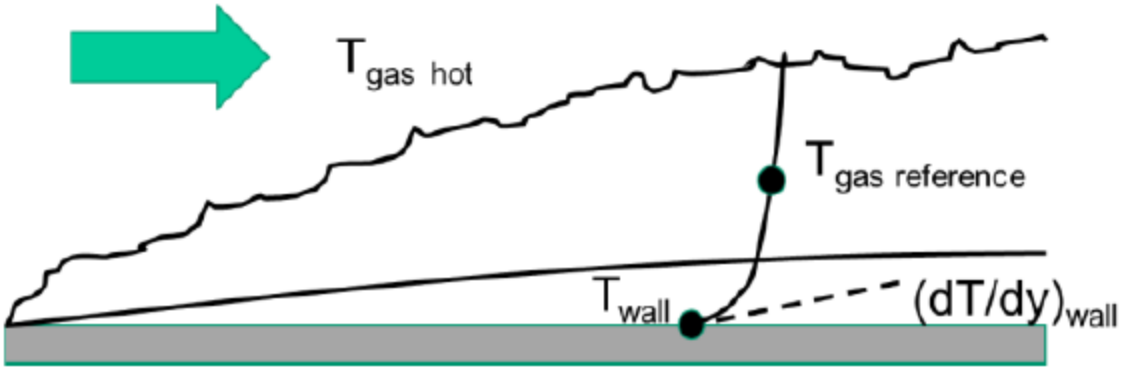

Figure 8.3 Schematic of heat transfer from hot gas to wall using a reference gas temperature inside the turbulent boundary layer [14]**.**

To apply T_{HG} in Fluent, a simple UDF was used. UDFs allow the user customizability of the simulation, filling the needs not met by the CFD software. UDFs are written separately in C++ using Fluent macros and can be implemented on boundary conditions or domains. The UDF code is shown in Appendix B - Heat Transfer Simulations UDF.

8.2 Validation of the Heat Transfer Model

Comparisons between the developed heat transfer model and numerical and experimental results from [31] are made in this subsection. The choice to compare results from this paper is justified by the similarity of application of both models: both attempt to predict the solid and fluid temperature offered by transpiration cooling in the application of a combustion chamber. The geometry in [31] is the same as Figure 8.2, except the reservoir is not modelled in [31].

In the referenced paper, transpiration cooling is evaluated for application in a rocket thrust chamber, for this reason, the velocity inside the channel is much larger than the one experienced in gas turbine combustion chambers. Air is the only fluid present.

8.2.1 Differences in heat transfer model

The model used in [31] differs from the one used in this paper, the differences and modifications are detailed below.

8.2.1.1 Domain

Modifications to the domain are implemented to reflect the experimental case [31], the channel dimensions are 80 cm x 6 cm x 9 cm (L x H x W) and the PM dimensions are 6.1 cm x 1.5 cm x 6.1 cm (L x H x D) with the PM starting at 58 cm downstream from the channel entrance. Modifications to the computational domain were made to replicate these dimensions.

8.2.1.2 Reservoir boundary conditions

Coolant flow inside the reservoir was not modeled in [31] and was therefore also not modeled during the validation step. A different boundary condition thus needed to be applied. In [31], the back side temperature of the PM on Ψ_{BS} is measured and set as a boundary condition, therefore:

$$T_s = T_b, \quad T_f = T_{f,R} \text{ on } \Psi_{BR} \tag{8-22}$$

where T_b is the measured back side temperature of the PM, and $T_{f,R}$ the fluid temperature entering the PM is determined by Eq. (8-23). In [31], the inlet fluid temperature of the coolant

on the interface between the reservoir and backside of the PM is determined by the energy balance:

$$-(1-\epsilon)(k_s \nabla T_s)\cdot n = c_{p,f}\rho_R V_y\left(T_{f,R} - Tc\right) \quad \text{on} \quad \Psi_R \tag{8-23}$$

where V_y is the inflow velocity of the coolant normal to the boundary, T_c the coolant temperature inside the reservoir, and n the normal vector. The density of the inlet coolant can be computed from the ideal gas law:

$$\rho_c = \frac{P_c}{RT_f} =: \rho_R \qquad \text{on } \Psi_R \tag{8-24}$$

where R is the ideal gas constant, and P_c the pressure of the coolant in the reservoir.

It appears wrong to apply the measured solid temperature of the back side of the PM as a boundary condition. The solid temperature should be determined by the heat balance between convection from the coolant entering from the reservoir and conduction coming through the PM. As the fluid temperature inside the reservoir is known, and no apparent heat transfer mechanism is applied on the fluid prior to entering the PM, the reservoir fluid temperature is used as the boundary condition.

In the simulations, the back side temperature of the PM is not imposed, instead it is used as reference to validate the results. As the fluid temperature inside the reservoir is known, it is applied as the fluid inlet temperature. The coolant mass flux is determined using the BR and known density and velocity of the main flow.

8.2.1.3 Heat transfer from hot gas

The heat transfer from the hot gas to the PM on Ψ_{HG} is solved differently in [31] than presented in subsection 8.1.3. They used the following equation:

$$(k_s \nabla T_s)\cdot n = c_{p,f}\rho V_{y,HG}\left(T_{HG} - T_f\right) + k_{HG}\nabla T_{HG}\cdot n \tag{8-25}$$

were $V_{y,HG}$ is the velocity of the hot gas normal and directly above the boundary, n the normal vector, and k_{HG} the conductivity coefficient of the hot gas. Overpredictions of PM surface

temperatures was obtained in [31], especially at high BR, thus the heat transfer method seen in subsection 8.1.3 was used.

8.2.2 Experimental conditions

Hot gas flow conditions inside the channel are presented in Table 8-1. At a Mach number of 0.5, the static temperature is $500\,K$ and was calculated using 1st law applied to 1D compressible flow, seen below.

$$\frac{T}{T_t} = \left(1 + \frac{\gamma - 1}{2} M^2\right)^{-1} \tag{8-26}$$

where T is the fluid static temperature, T_t the fluid total temperature, γ the specific heat constant which for air is 1.4, and M the Mach number.

Table 8-1 Hot gas flow conditions inside the channel in [31]**.**

Parameter	*Symbol*	*Value*
Mach Number	M	0.5
Density	ρ_{HG}	0.65 $\frac{kg}{m^3}$
Total temperature	$T_{t,HG}$	525 K
Pressure	ρ_{HG}	95,600 Pa

A Mach number of 0.5, defined by Eq. (8-27) with a speed of sound (c) of $448.22\ \frac{m}{s}$ calculated using Eq. (8-28) results in a gas velocity of $224.11\ \frac{m}{s}$ which is implemented as a velocity inlet for the hot gas.

$$M = \frac{v}{c} \tag{8-27}$$

$$c = \sqrt{\gamma RT} \tag{8-28}$$

where R is the gas constant equal to 287 $\frac{J}{kg \cdot K}$ for air, and T the static temperature. The PM properties used in [31] are presented in Table 8-2.

Table 8-2 PM parameters from [31]**.**

Parameter	*Symbol*	*Value*
Material		Carbon/Carbon (C/C) ceramic
Porosity	ϵ	0.116
Density	ρ_s	1.14 $\frac{kg}{m^3}$
Specific heat capacity	$c_{p,s}$	622 $\frac{J}{kg \cdot K}$
Effective heat conductivity	k_s	1.4 $\frac{W}{m \cdot K}$
Permeability	K_D	$1.196 \cdot 10^{-13}\ m^2$
Forchheimer coefficient	K_F	$8.8 \cdot 10^{-9}\ m$
Inertia coefficient	f	39.30
Heat transfer coefficient	h_i	$10^6\ \frac{W}{m^2 K}$

In the referenced paper they define the source term of the Darcy-Forchheimer momentum equation as follows:

$$S = -\mu K_D^{-1} v - \rho K_F^{-1} |v| v \tag{8-29}$$

where K_D^{-1} is the permeability, and K_F^{-1} the Forchheimer coefficient which can be related to the inertia coefficient with the following relation $f = \frac{\sqrt{K_D}}{K_F}$, from Eq. (5-11).

The PM used in the referenced study is very different from high porosity aluminum metal foams seen so far in this thesis. A Carbon/Carbon (C/C) ceramic matrix composite where both fibers and matrix are made of carbon was studied. The structure is defined by the layers of fibers in the matrix and has a small porosity of 11.6% with very high resistance to flow movement.

They mention that h_i, from Eq. (8-1) and (8-2), cannot be measured, only estimated, and the value is given without further elaboration. This presents a source of error as the interfacial convective coefficient drastically alters the temperature distribution inside the PM for the solid and fluid phases. Underpredicting the coefficient will result in higher temperature distributions and vice-versa. Having a very high internal convective coefficient can cause the heat transfer between solid and fluid phases to be so large, they become thermally equal. As Fluent uses a volumetric convective coefficient, and no specific surface area was provided in [31], an a_{sf} of one is assumed as it is understood the heat transfer coefficient given is the volumetric heat transfer coefficient.

As no relation was given for the value of h_i, it is assumed to have been chosen to match simulations to experimental results, and thus, the same method is applied in the simulations. As mentioned in 8.2.1.2, the applied boundary condition on Ψ_R with the reservoir in [31] artificially maintains the back side temperature, whereas it is determined by the balance of convection from coolant and conduction from the media in the simulations. Therefore, much smaller values of h_v are applied to achieve reasonable agreement with experimental results and varied per BR as it is expected to change with the mass flux of coolant. An assumed value as low as $14{,}000\frac{W}{m^3K}$ is applied for the $BR = 0.001$ case, compared to the constant $h_v = 10^6\frac{W}{m^3K}$ in [31]. Although there is no literature or experimental support confirming the value of 14,000 for C/C, it is judged reasonable by the author since the C/C ceramic composite sample with a porosity of 0.116 is expected to have a small specific surface area a_{sf} and a low mass flux is expected to create only a low interfacial convective coefficient h_i. In fact, h_v for PM peak at porosities around 0.7 and reach very low values around 0.15 and when approaching 1, according to [29], [30] and as discussed in subsection 8.1.2.

The density given in the paper appears wrong and unclear to the author as the density of C/C ceramic is between $1300\frac{kg}{m^3}$-$1800\frac{kg}{m^3}$ and, when multiplied by the porosity, equates to a sample density between $1149.2\frac{kg}{m^3}$-$1591.2\frac{kg}{m^3}$ and not the $1.14\frac{kg}{m^3}$ reported [73]. It may be a typo and the units are supposed to be $\frac{g}{cm^3}$. However, as the correct density of the sample is not clear, a material density of $1600\frac{kg}{m^3}$ was implemented in the model. The coolant parameters are presented in Table 8-3.

Table 8-3 Coolant parameters (air) from [31]**.**

Parameter	*Symbol*	*Value*
Specific heat capacity	$C_{p,f}$	$1010\,\frac{J}{kg \cdot K}$
Effective heat conductivity	k_f	$0.04\,\frac{W}{m \cdot K}$
Dynamic viscosity	μ	$1.7 \cdot 10^{-5}\,\frac{N \cdot s}{m^2}$

The permeability of this C/C sample is approximately six orders of magnitude smaller than aluminum metal foams, signifying a large pressure gradient is required to drive flow through the PM, as seen in Table 8-4, where the four blowing ratios studied in [31] with their parameters are tabulated.

Table 8-4 PM boundary conditions for four blowing ratios from [31]**.**

		Blowing Ratio (***BR***)			
	Symbol	0.001	0.002	0.003	0.01
Coolant reservoir pressure	P_c	326,400 Pa	448,400 Pa	544,400 Pa	1,093,400 Pa
Coolant reservoir temperature	T_c	336.3 K	319.1 K	311.7 K	296.6 K
Solid temperature, reservoir	$T_{s,R}$	403.3 K	363.4 K	342.6 K	304.1 K
Volumetric convective coefficient	h_v	$1.4 \times 10^4 \frac{W}{m^3 K}$	$2 \times 10^4 \frac{W}{m^3 K}$	$3 \times 10^4 \frac{W}{m^3 K}$	$6 \times 10^4 \frac{W}{m^3 K}$
Hot gas surface convective coefficient	h_s	$257.20 \frac{W}{m^2 \cdot K}$	$219.86 \frac{W}{m^2 \cdot K}$	$186.7 \frac{W}{m^2 \cdot K}$	$49.59 \frac{W}{m^2 \cdot K}$

The blowing ratio was defined previously in Eq. (2-4) and reservoir solid temperature was measured during their experiment. The heat transfer coefficient for the zero-blowing condition was determined to be $298.72 \frac{W}{m^2 \cdot K}$, with the calculations found in Appendix A - Heat Transfer Analysis.

8.2.3 Results and discussion

Results from simulations using Eq. (8-15), as described in subsection 8.1.3, are compared to experimental and numerical simulation data from [31] in Figure 8.4. Full simulation curves from [31] are not available and therefore only surface results are presented. However, they give a good representation of their predictions. Experimental data points have known y positions in the PM but unknown x positions, therefore, the values do not represent a linear sequence of temperature points. The coordinates x and y are the same as in Figure 5.1. However, the positions of points on the surface of the PM can be deduced by comparing their

temperatures. Three temperature probes were placed just under the surface of the samples, therefore, the highest temperature point represents the leading-edge probe and the lowest temperature point the trailing edge probe as surface temperatures are expected to reduce over the length of the sample. The same comparison is made using Eq. (8-13) in Appendix A - Heat Transfer Analysis. Results from this comparison were not as good as the ones using Eq. (8-15), therefore it was not used for further simulations in 8.3.

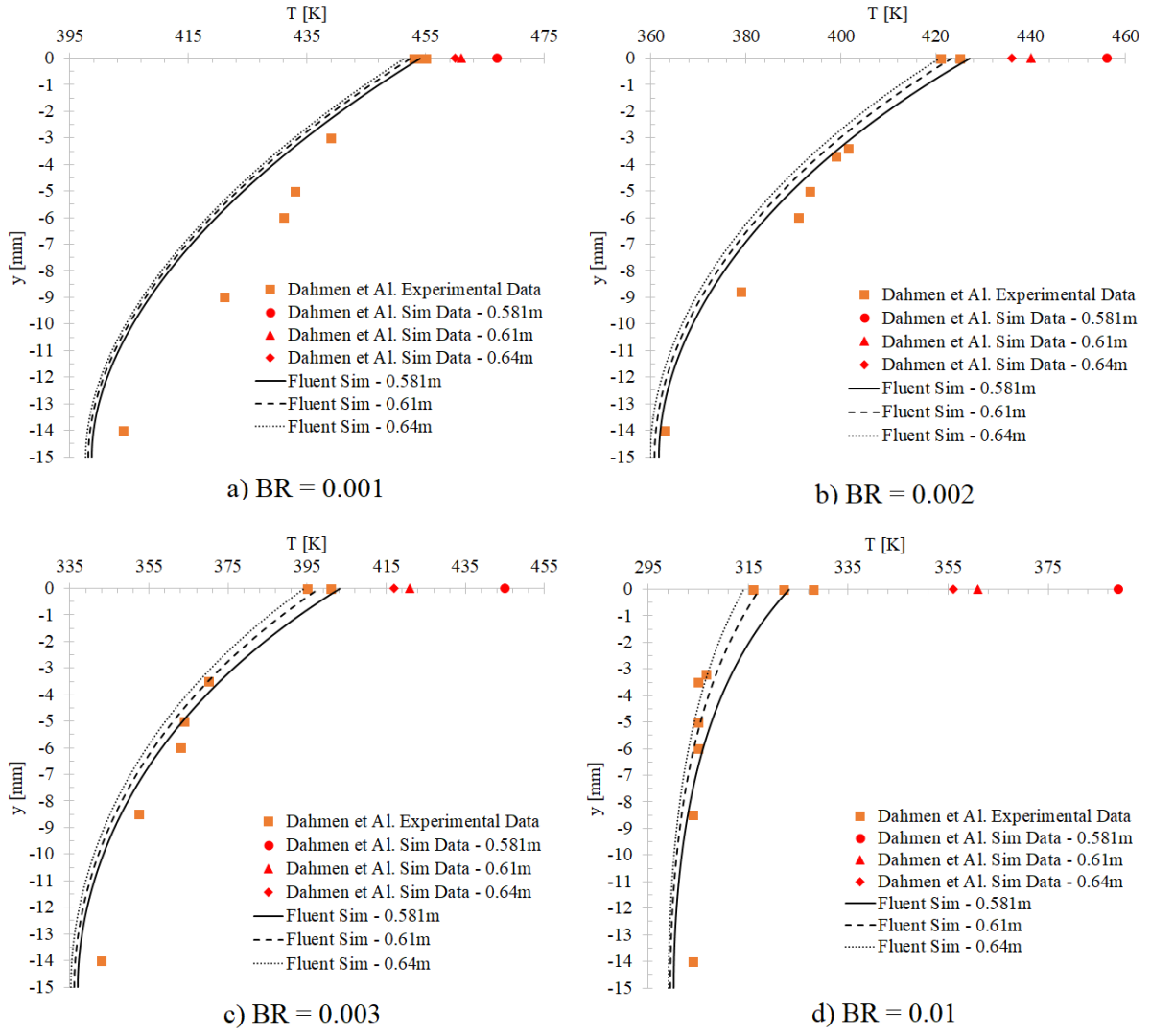

Figure 8.4 PM temperature distributions between the model of this thesis, and simulation and experimental data from [31] **at four different BR. Simulations of the current model used equation (8-15) to estimate hot gas convective heat transfer coefficient.**

Simulations show good agreement with experimental data for internal and surface temperature distributions. Small discrepancies are present at BR of 0.001 where internal temperature distribution is underpredicted and at BR of 0.01 where surface temperature is also slightly underpredicted. These differences can be explained by an incomplete heat transfer model from Eq. (8-15), where varying importance of advection and temperature distribution may not be accurately captured. Another potential explanation is the film temperature T_{HG} measured by the cell directly above the surface of the samples. A realistic measure of this temperature would depend on the boundary layer thickness, thus, a constant cell size can overpredict T_{HG} at low BR where boundary layer thickness is expected to be smaller, causing larger heat transfer and vice-versa. This helps explain the underprediction at BR of 0.01. The estimation of h_v is also a source of error.

Compared to the numerical simulations performed by [31] shown by red points in Figure 8.4, the method employed in this study obtained better agreement with experimental data. Investigating the surface heat transfer method of [31] as shown in Eq. (8-25) reveals a potential mistake. In the referenced paper, Eq. (8-25) was applied based on [17], which describes the heat transfer to the wall to be as follows:

$$\mathrm{q_w} = \mathrm{q_{0^+}} - \mathrm{q_{Layer}} \tag{8-30}$$

where q_{0^+} is the heat flux transferred from the free stream, and q_{Layer} the energy transfer from the mixing of coolant and hot gas in a transition layer causing the change in temperature [17]. A schematic of the analysis in [17] is shown in Figure 8.5. 0^+ indicates the position at the edge of the transition layer where $y = 0^+$ with $y = 0$ being the surface of the PM.

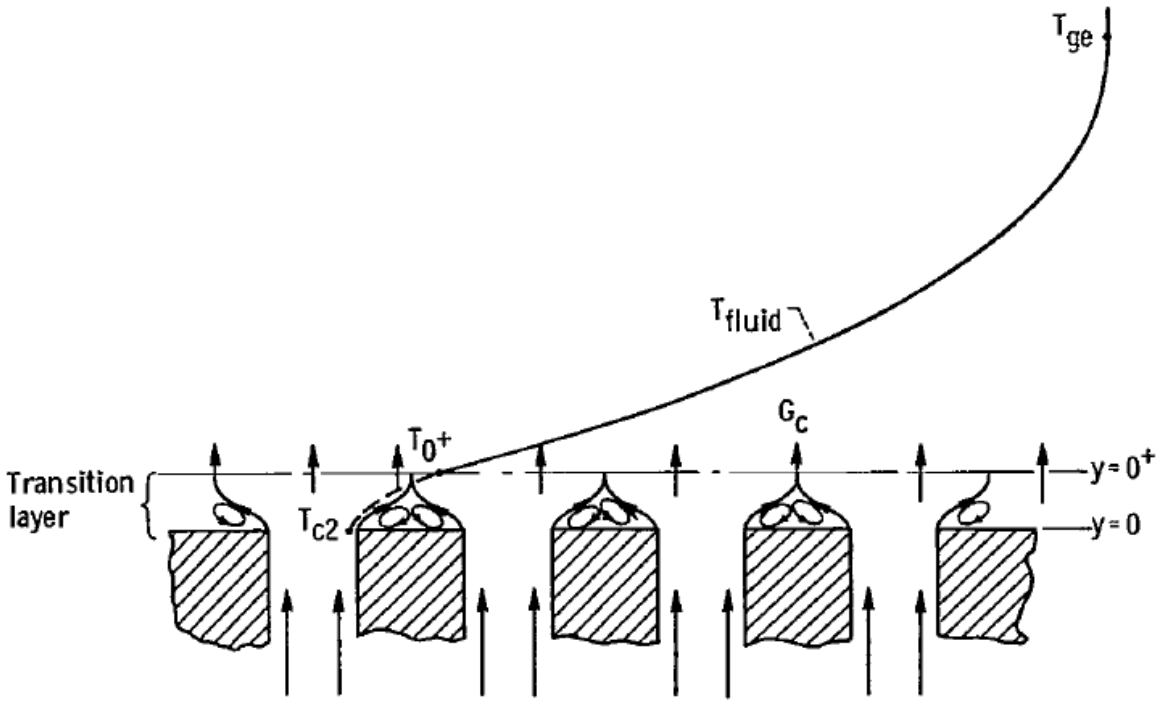

Figure 8.5 Simplified heat transfer model in the general case of transpiration cooling [17].

The two heat equations are presented below:

$$q_{0^+} = \left(k_f \frac{dT}{dy}\right)_{0^+} \tag{8-31}$$

$$q_{Layer} = \rho_{f,c} v_{y,c} Cp(T_{0^+} - T_c) \tag{8-32}$$

These two equations are used in Eq. (8-25), however, they are added together as opposed to q_{Layer} being subtracted from q_{0^+} in Eq. (8-30). No explanation is given in [31] for this change. Attempts were made in this study to apply Eq. (8-30), however, no convincing results were reached as T_{0^+} is difficult to obtain since the transition layer thickness is unknown and likely very thin. In turn, q_{Layer} was much larger than would be necessary to obtain results conclusive with experimental data from [31].

The effect of mesh refinement around the surface of the PM by applying a bias factor was investigated. Two meshes with bias were compared for $BR = 0.003$, one with a bias of 100 below the surface of the PM, and the other with biases of 100 below the surface and 10 above

the surface of the PM. The bias factor was discussed previously in section 5.4. See Appendix A - Heat Transfer Analysis for figures of the meshes. Results for the three meshes for the normalized temperature between coolant inlet temperature and hot gas temperature are presented in Figure 8.6. Refinement around the surface of the PM achieved better definition of the boundary layer, however, as the mesh is refined, the cell used for T_{HG} in Eq. (8-21), shown schematically in Figure 8.3, delivers a lower temperature value as it is closer to the PM's surface, reducing the heat transfer to the PM. This effect is like section 5.4 where changing the cell size changes the area for which the value is measured, in this case temperature. This is more pronounced further down the surface of the porous media where the boundary layer is thicker. The effect of lower heat transfer can be seen in Figure 8.7, where the surface temperature distribution of the PM is shown for the three meshes. The two meshes with no refinement above the surface of the porous media resulted in the same temperature distribution. This is because T_{HG} is relatively constant between the two.

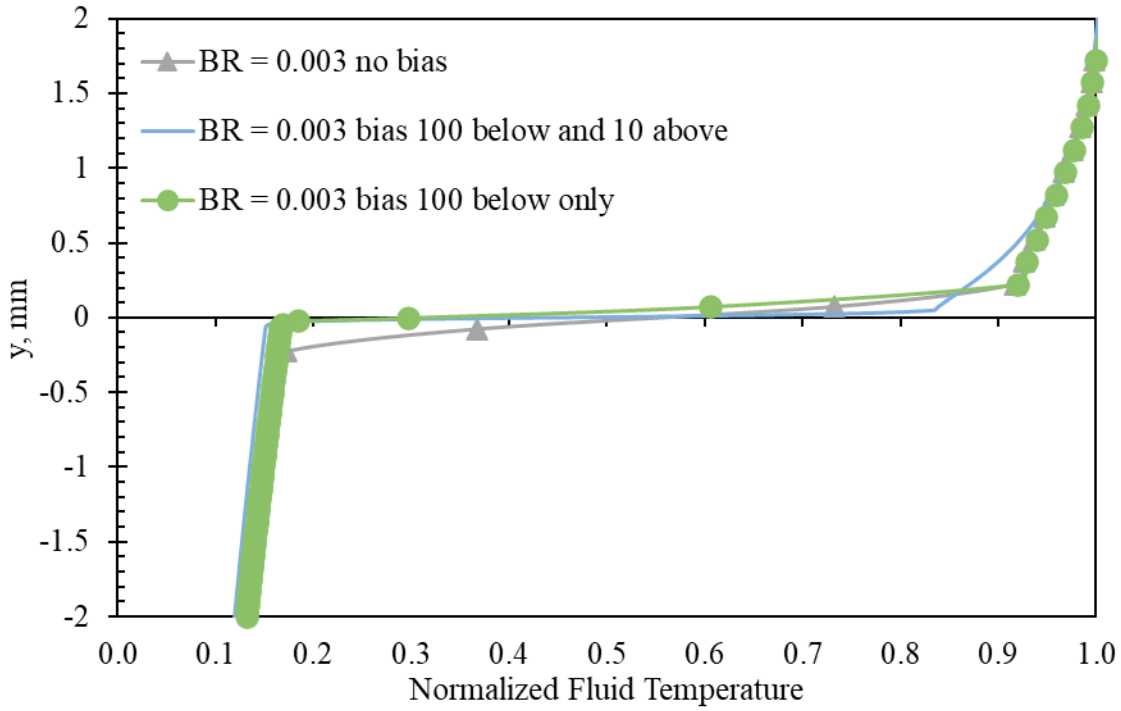

Figure 8.6 Normalized fluid temperature of $BR = 0.003$ 2 mm above and below the surface of the PM at $x = 0.61\ m$ with element size of 0.15 mm and for three cases of mesh refinement: no bias, bias of 100 below, and bias of 100 below and 10 above. The points correspond to the value at the center of cells.

Observation of Figure 8.6 shows higher fluid temperature just below the surface of the PM when no bias is applied inside the PM. Thus, to retain a relatively higher T_{HG} but more accurate fluid temperature distribution inside the PM, the bias factor of 100 below the surface of the PM and no bias factor above the surface of the PM was selected.

Ideally, a method for estimating $T_{gas\ reference}$, as seen from Figure 8.3 would be used and finer meshes could be applied without affecting the heat transfer to the PM. However, for the purpose of comparing the PM seen in this thesis, it was deemed a reasonable approximation.

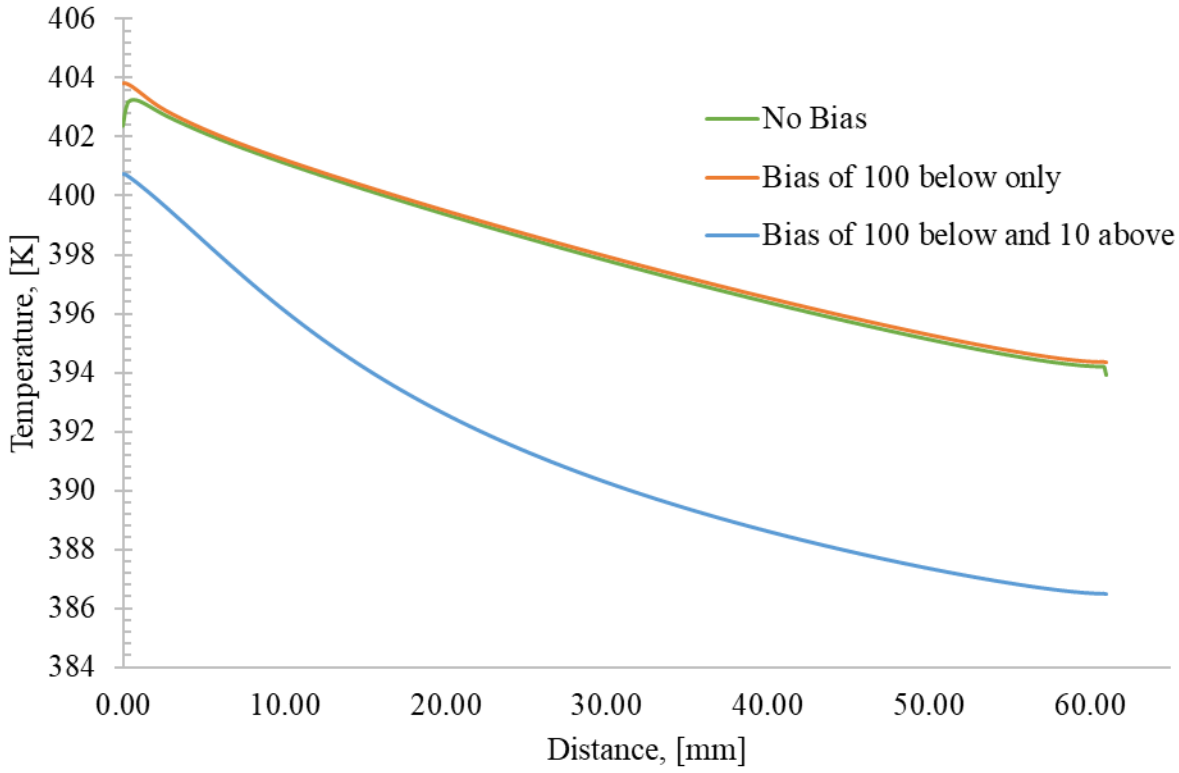

Figure 8.7 Surface PM temperature for meshes with elements size of 0.15 mm with no bias, a bias of 100 for inside the PM only, and a bias of 100 inside the PM and 10 above. The blow ratio used was 0.003, based on the experimental data from [31].

From the comparison presented in this section, reasonable results against experimental data from the literature were obtained. It can be concluded that the heat transfer method applied in this study satisfactorily predicts the temperature inside PM for the general case of transpiration cooling and is expected to be suitable for the comparison of CFE_M and CFE_T.

8.3 Porous Media Comparison

After developing and validating the numerical heat transfer model, comparison between different PM investigated in Chapter 6 and 7 can be performed to evaluate their CFE_T. CFE_M and CFE_T are also compared to determine the validity of the mass analogy. The PM are: Sample ID 2, the 20 PPI high porosity aluminum metal foam from Table 5-2; Sample ID 5 and 6, compressed foam from Table 7-1; Profile ID 2 and 4, profiled PM without leading edge solution; and Profile ID 4 with leading edge open section from subsection 7.3.3. These samples give a good representation of the different possible CFE_M of PM presented in this Thesis.

8.3.1 Numerical conditions

Simulations are performed at the 30 SLPM ($BR = 0.00858$) coolant flow rate with main flow temperature at 500K. To keep the blow ratio constant, the main flow velocity is increased from $33\frac{m}{s}$ to $55.77\frac{m}{s}$ as increasing the fluid temperature decreases the density. Hot gas flow conditions are presented in Table 8-5, coolant parameters in Table 8-6 and PM parameters in Table 8-7.

Table 8-5 Hot gas flow conditions inside the channel for the heat transfer simulations of PM seen in Chapters 6 and 7.

Parameter	*Symbol*	*Value*
Mach Number	M	0.124
Density	ρ_{HG}	$0.6969\ \frac{kg}{m^3}$
Temperature	T_{HG}	$500\ K$
Velocity	v_{HG}	$55.77\frac{m}{s}$
Pressure	P_{HG}	$100\ KPa$

Table 8-6 Coolant parameters (Nitrogen) and inlet conditions for the heat transfer simulations of PM seen in Chapters 6 and 7.

Parameter	*Symbol*	*Value*
Specific heat capacity	$C_{p,f}$	$1038\,\frac{J}{kg \cdot K}$
Effective heat conductivity	k_f	$0.026\,\frac{W}{m \cdot K}$
Dynamic viscosity	μ	$1.79 \cdot 10^{-5}\,\frac{N \cdot s}{m^2}$
Inlet Temperature	T_{fi}	$300K$
Mass Flow Rate		$0.0006253\,\frac{kg}{s}$
Blow Ratio	BR	0.00858

Table 8-7 PM parameters for the heat transfer simulations of PM seen in Chapters 6 and 7.

Parameters	*Symbol*	*High Porosity Foam – Sample ID 2*	*Compressed Foam - Sample ID 5*	*Compressed Foam - Sample ID 6*	*Profile ID 4 and 5*
Porosity	ϵ	0.9245	0.6	0.44	See Table 7-2
PPI		20	40	40	40
Aluminum Density	$\rho_s, \left[\frac{kg}{m^3}\right]$	2719	2719	2719	2719
Specific Surface Area	$a_{sf}, \left[\frac{m^2}{m^3}\right]$	956.13	1800	6720	3000-5000
Specific Heat Capacity	$c_{p,s}, \left[\frac{J}{kg \cdot K}\right]$	871	871	871	871
Solid Conductivity	$k_s, \left[\frac{W}{m \cdot K}\right]$	202.4	202.4	202.4	202.4
Permeability	$K \cdot 10^7, [m^2]$	1.1	0.00924	0.00175	See Table 7-2
Inertia Coefficient	f	0.104	0.383	0.413	See Table 7-2
Average Fiber Diameter	$d_f, [m]$	0.00035	-	-	-
Average pore diameter	$d_p, [m]$	-	0.0005	0.0005	0.0005

As opposed to section 8.2, the plenum is modeled, thus, coolant boundary conditions are applied on the reservoir boundary Ψ_R as shown in Figure 8.2. Profile IDs 2 and 4 profile the specific surface area using a square-root function like for the permeability and inertia coefficient. Aluminum properties of conductivity, density and specific heat are applied by Fluent by setting the PM material as aluminum and are presented in Table 8-7 before the effect of porosity. These values are also not varied against temperature, as the impact of temperature variation in the PM is expected to be small.

8.3.2 Results and discussion

Results of the simulations with heat transfer are presented here. First, the surface PM temperature distribution is presented in Figure 8.8. The effects of the uneven CFE_M of high porosity foam, blue curve, is apparent with the highest PM surface temperature out of all samples. The high temperature can be explained by the lack of coolant exiting the first half of the sample, resulting in a combination of lower fluid heat capacity and higher surface fluid temperature, as seen in Figure 8.9.

Large reduction in maximum solid surface temperature is obtained when changing the PM from a high porosity foam to the compressed foam of Sample ID 5, (orange curve in the figures). The reduction in temperature can be explained by the reduction in average boundary layer fluid temperature due to more evenly distributed coolant, better utilization of fluid heat capacity, and increased effective conductive heat transfer coefficient due to lower porosity.

Both profile ID 2 and 4, (gray and red curves in the figures), respectively, offered slight improvement over the compressed foam of sample ID 5, where both profiles achieved relatively uniform temperature distributions. This is largely attributable to the increase in coolant to the leading edge, reducing the fluid surface temperature, observed in Figure 8.9.

The profiles where able to achieve their design goal of offering relatively uniform temperature distributions by intentionally redistributing coolant. It should be noted that by using aluminum as material for the PM with a large conductivity diminishes the benefits of profiling the PM. This suggests profiled PM may be better suited for use in lower conductivity samples, such as a two-layer PM with a ceramic thermal barrier coating on the surface which has a low conductivity.

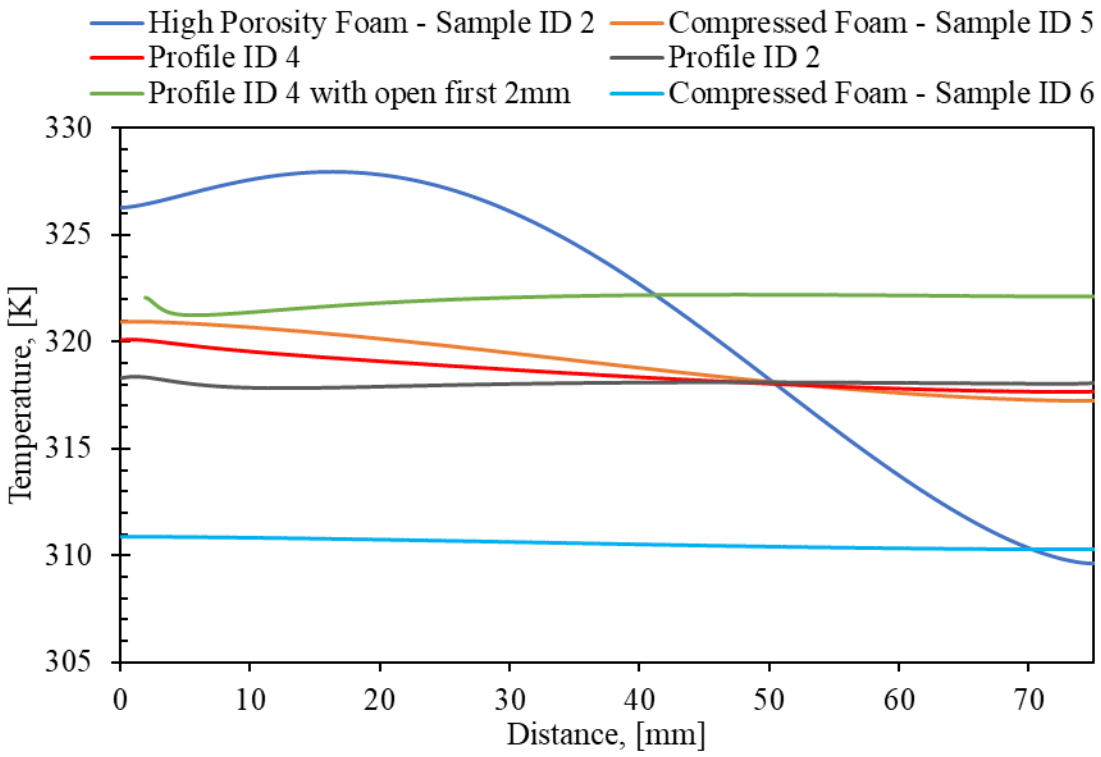

Figure 8.8 Surface wall temperature distribution for different PM investigated in this study under heat transfer condition with $BR = 0.00858$.

Profile ID 4 with leading edge solution of an open 2 mm section (green curve in the figures) performed worse than the samples without the leading-edge solution. The difference is attributable to the lower amount of heat capacity available in the PM as most of the coolant exits the leading edge. It was able to achieve lower surface fluid temperature for the first half of the sample as seen in Figure 8.9, however, it was not enough to improve the temperature distribution of the PM. The higher second half surface fluid temperature can be explained by mixing in the boundary layer and low transpiration of coolant from the PM. This comparison indicates that implementing a leading-edge solution for lower CFE_M with this method is inferior to the regular profiled samples.

The temperature profiles obtained are lower than the ones in the validation section 8.2, even though the hot gas temperature and coolant inlet temperature are roughly equal. The difference can be attributed to the difference in Reynolds number, with larger Reynolds number resulting in larger convective heat transfer coefficient h_s and the Reynolds number in

the validation section being larger than the one in this section. Larger temperature profiles due to larger Reynolds numbers has also been observed in [11].

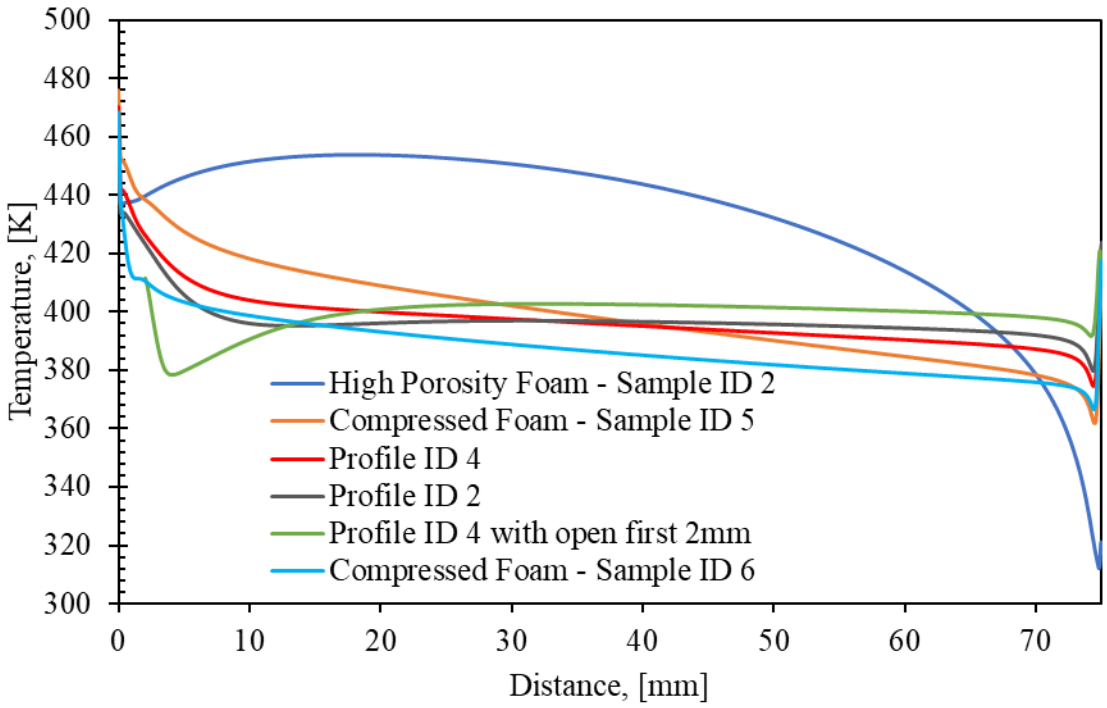

Figure 8.9 Surface fluid temperature distribution for different PM investigated in this study under heat transfer condition for $BR = 0.00858$.

Finally, the compressed foam of Sample ID 6, (teal in the figures), offered the lowest surface temperature distribution out of all samples simulated by a significant margin. Initial investigation of the problem and equations would suggest the opposite should be true as it has the lowest porosity, thus, largest surface available for heat transfer as per Eq. (8-12). In fact, it was determined by Liu et. Al [52] in their numerical simulations that decreasing the porosity resulted in higher temperature distributions in the PM. However, they did not model the hot gas flow and the heat transfer from convection. Instead, they applied a constant heat flux in all cases, thus, as the porosity decreases, so did the volumetric heat transfer coefficient per Eq. (8-9) and (8-10) and demonstrated in Figure 8.1. The surface heat flux boundary condition applied in their simulations is also significantly larger, $2 \times 10^6 \frac{W}{m^2}$ versus approximately $4500 \frac{W}{m^2}$ for a $150\ K$ temperature difference in these simulations. More on this subject in the following subsection.

The CFE_Ts are presented in Figure 8.10 and obtained significantly larger values than the CFE_Ms as shown in Figure 8.11. From the comparison of both graph it can be concluded that the mass analogy method does not predict accurately the CFE_T. However, this was expected as the mass analogy was adopted in subsection 4.1.2 under the assumption that the surface wall temperature equaled the cooling film temperature, therefore ignoring any cooling provided by the conduction into the PM from the surface wall and from volumetric convection inside the porous media. Thus, the CFE_M acts as a lower bound to the potential CFE_T, as the surface temperature of the porous media can never be lower than the temperature of the film it is in contact with, assuming radiation to be zero.

The CFE_M, in addition of providing a lower bound, is a good proxy to the shape of the CFE_T and temperature distribution curves, as best presented by the high porosity foam (sample ID 2) in the graphs presented in this subsection. However, this comparison underlines the importance of other variables in achieving high CFE_T, such as the coolant flow heat capacity for profile ID 4 with open first 2 mm. And that achieving an ideal CFE_M is not the only consideration to offer the most efficient thermal protection.

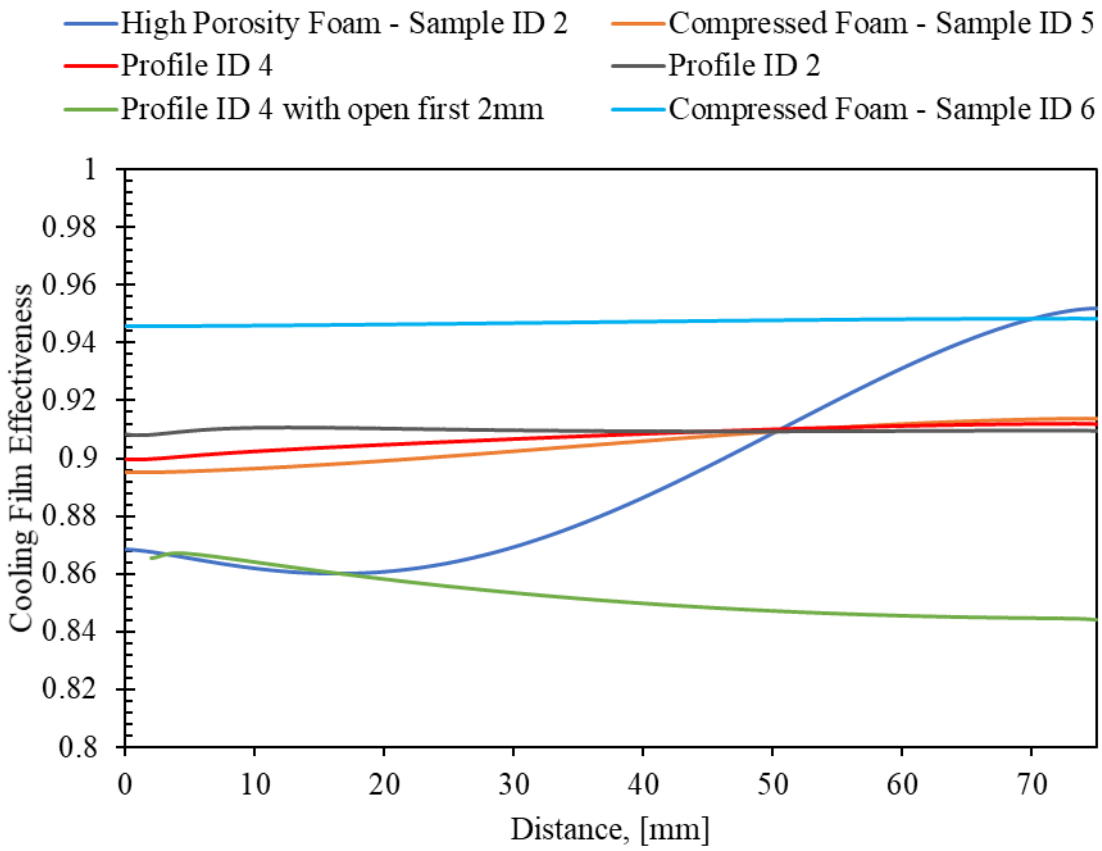

Figure 8.10 CFE_T distribution for different PM investigated in this study under heat transfer condition for $BR = 0.00858$, $T_i = 300\ K$ and $T_{HG} = 500\ K$.

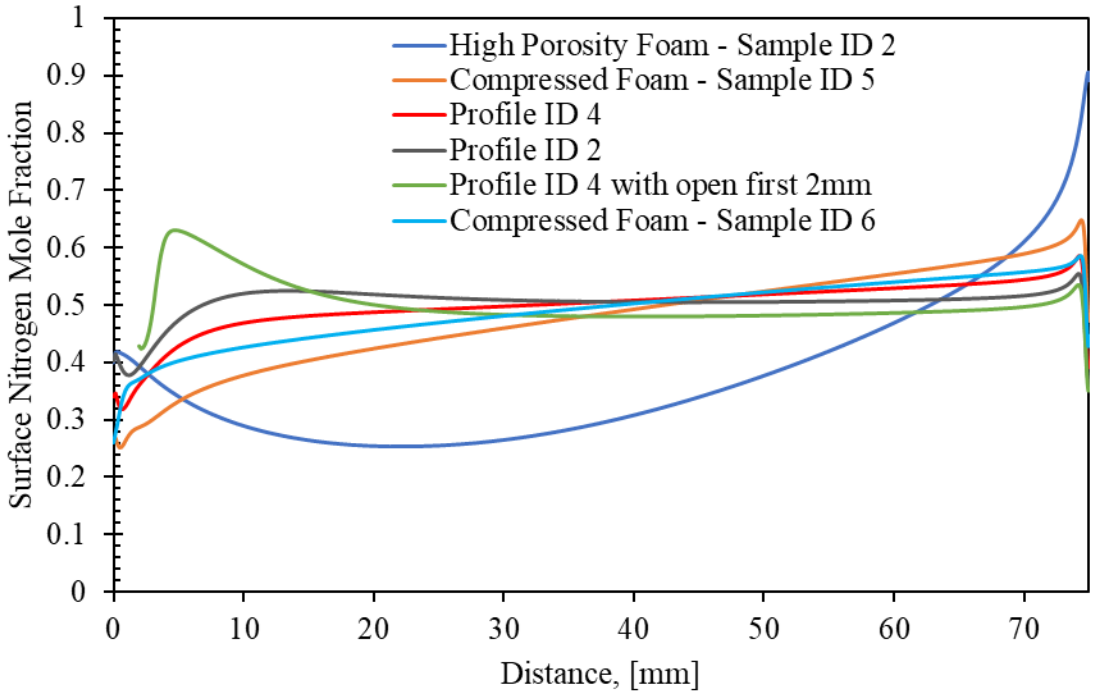

Figure 8.11 CFE_M distribution for different PM investigated in this study under heat transfer condition for $BR = 0.00858$, $T_i = 300\ K$ and $T_{HG} = 500\ K$.

8.3.3 Boundary layer penetration on heat transfer

Isolating the various variables responsible for the heat transfer to the PM revealed that reducing the porosity also reduced the temperature distribution in the PM, contrary to what was expected. Investigating the variables affected by the porosity, it was found that the reduction in volumetric convective heat transfer coefficient resulted in the lower temperatures.

A sensitivity analysis of Sample ID 6 for three different h_v with all other conditions and variables constant, shown in Figure 8.12, demonstrates the effect. The lowest h_v resulted in the lowest temperature distribution and vice-versa.

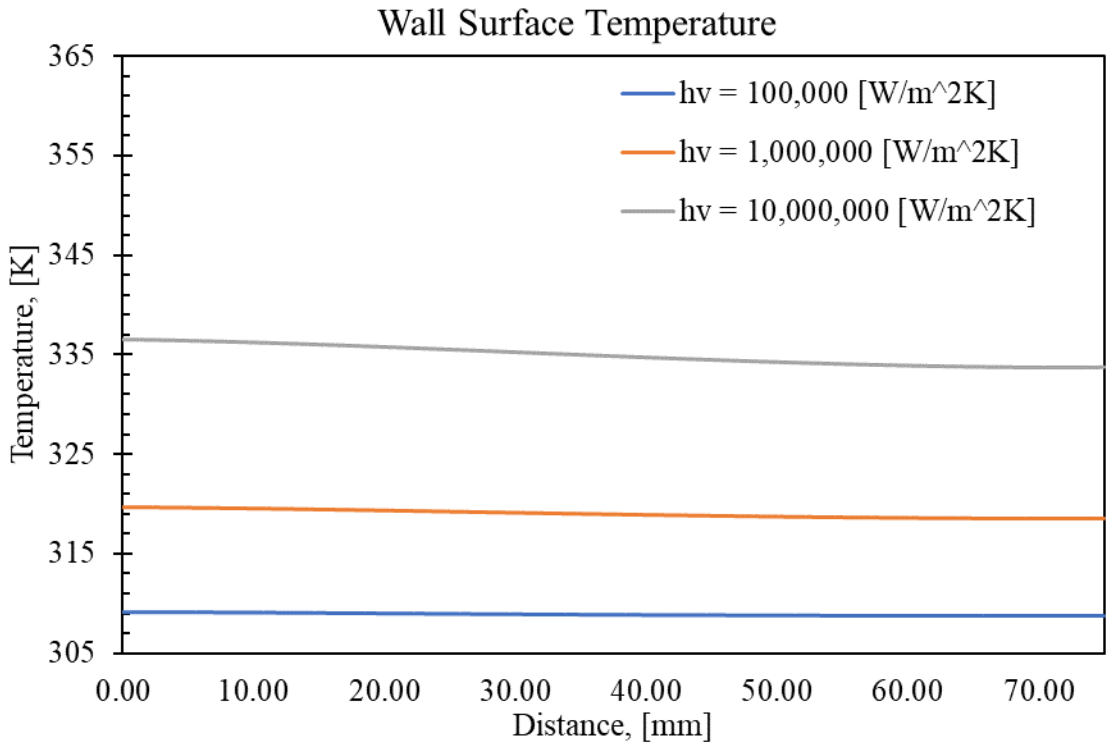

Figure 8.12 PM surface temperature based on three different volumetric heat transfer coefficient for sample ID 6 and $BR = 0.00858$.

The boundary layer has been reported of penetrating below the surface of the PM, especially for low permeability samples [36], [74], and seen in Figure 5.5. Thus, heat transfer from the hot gas can occur not only on the surface of the sample but also in a thin region inside the PM. The critical value is then h_v as it is much larger than h_s.

The air mole fraction and normalized fluid temperature based on the minimum 300 K and maximum 500 K for two millimeters above and below the surface at $x = 0.58\ m$ is plotted in Figure 8.13 for the simulations of Figure 8.8. This demonstrates air penetrating up to half a millimeter below the surface of the samples which significantly increases the temperature of the fluid in this region and causes large heat transfer. Sample ID 2 has more penetration than other samples due to low coolant mass flow rate at this location. However, the other samples show approximately the same amount of air penetration, which is not what would be expected.

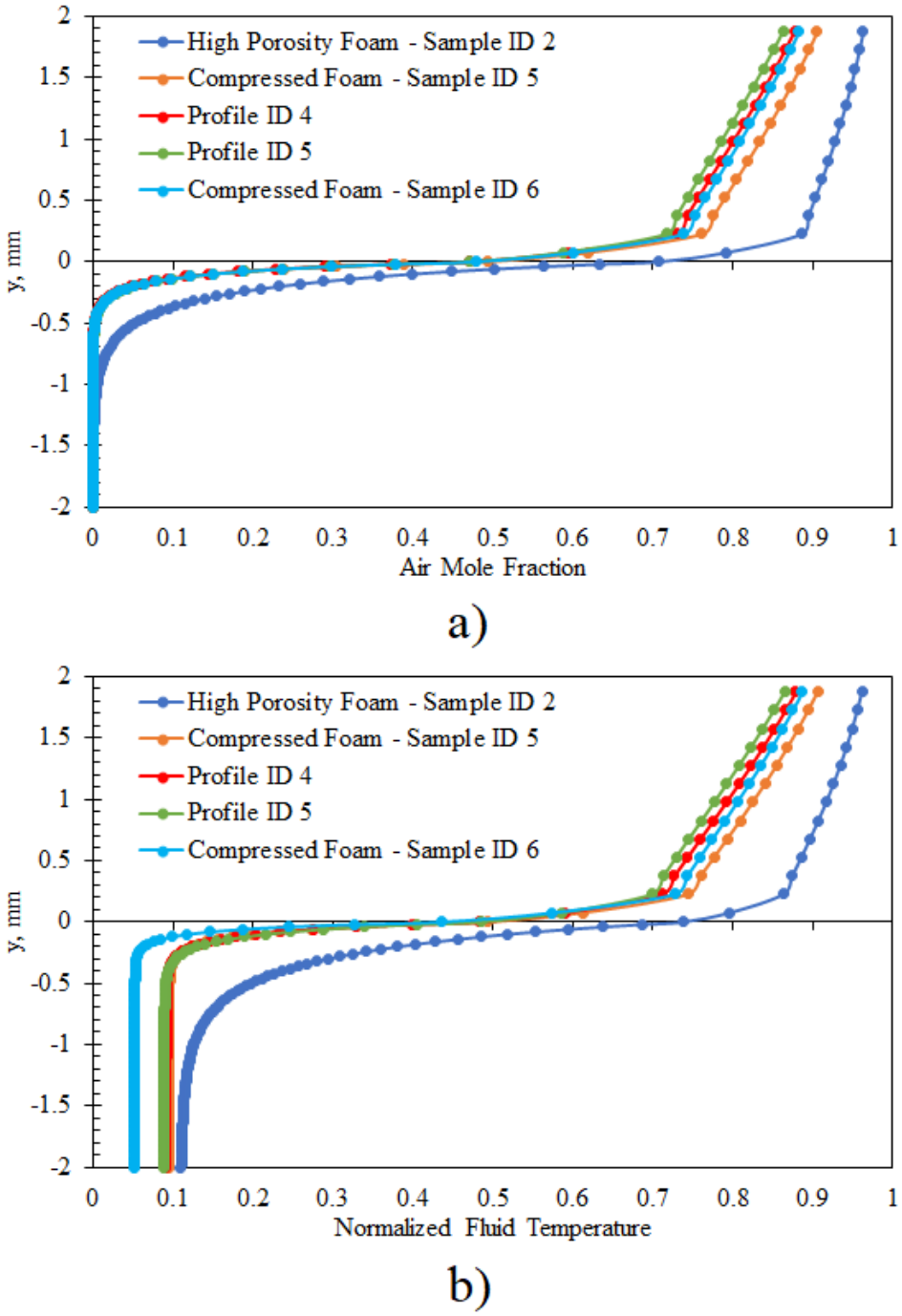

Figure 8.13 a) air mole fraction and b) normalized fluid temperature based on minimum 300 K and maximum 500 K for 2 mm above and below the surface of the simulations from Figure 8.8 at $x = 0.58\ m$ for $BR = 0.00858$.

It is unclear how accurately the simulations predict the penetration of air below the surface of the PM, which casts doubts on the validity of the heat transfer results. In the heat transfer

model validation of section 8.2, the effect of heat transfer due to flow penetration would be minimal due to the low volumetric heat transfer coefficients used. Figure 8.6 shows the normalized temperature for two millimeter above and below the surface of the C/C PM for three different meshes which indicate lower flow penetration than seen in Figure 8.13b), even though the BR is lower. This may be attributed to a higher hot gas Reynolds number or larger resistance to flow movement.

Highly permeable PM, i.e., high porosity and PPI, have more flow penetration than less permeable samples [36]. It is possible the flow penetration for a low porosity PM such as Sample ID 6 would be negligible. Experimental validation of the model based on samples with higher porosities than the ones used in section 8.2 would help determine the extent of flow penetration as a factor in transpiration cooling.

Nevertheless of the accuracy of the model on flow penetration, it can still be concluded that more uniform temperature distributions can be achieved when using profiled PM over regular compressed PM based on the results presented in Figure 8.8.

9 Profiled Porous Media CAD Design

Recent improvements in additive manufacturing of 3D printers and selective laser metal sintering (SLMS) have raised interest in producing PM using these methods. A review of PM produced by SLMS and 3D printing was presented in subsection 2.3.4. In this chapter, a method for creating CAD of profiled PM for production using AM is presented. The criteria which guided the design of the PM are established first, followed by the CAD assembly method. SolidWorks 2019 was used as the CAD software.

9.1 Porous Media Geometrical Criteria

A list of important geometrical design parameters considered in this design are presented below:

1) Structural integrity
2) High specific surface area
3) Limited possibility of fouling
4) Repeatability and ease of manufacturing

9.1.1 Structural integrity

Borrowing from the field of chromatography, a study from 2006 performed numerical simulations of silica monoliths for different porosities [75], in which each atom is connected tetrahedrally to surrounding atoms. This tetrahedral shape consists of a node with four arms at ~109.5^{o} from each other, as shown in Figure 9.1, which is assumed to offer a strong structure as it is the atomic structure of diamonds. For this reason, this structure was chosen for the profiled PM design, fulfilling criteria number one.

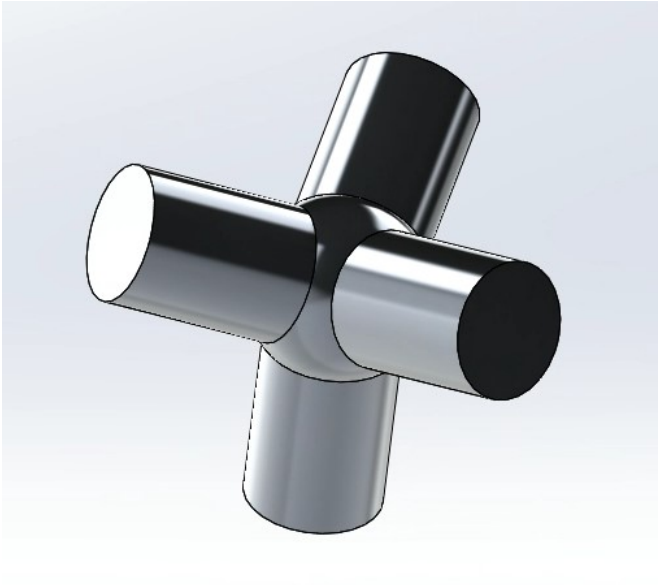

Figure 9.1 Tetrahedral shape consisting of a node with four arms at 109.5^{o} from each other. The arms are 0.3 mm from the center of the nodes. Made using SolidWorks 2019.

Another model which was considered is the Kelvin structure, a 14-faced tetradecahedron composed of six square faces and eight hexagonal faces. This structure is more representative of the metal foams structure and was used for numerical analysis in [76]. However, the aim of this chapter is not to reproduce a metal foam structure and its structural integrity is expected to be weaker than the diamond structure.

9.1.2 High specific surface area

High specific surface area will permit the maximum amount of heat transfer between the PM and the coolant. It can be fulfilled by increasing the PPI of the PM, which is accomplished by decreasing the length of the arms of the tetrahedral shape, as well as the diameter of the nodes and arms. Optimization could be achieved by determining at which porosity for certain arm and node diameters, and arm length, the maximum surface area occurs. This could help guide future designs. These optimum values are currently unknown, thus, maximizing the specific surface area will be achieved by simply reducing the PPI as much as possible.

9.1.3 Limiting fouling

Fouling can be limited by increasing the pore diameters, enabling more foreign objects to pass through without lodging themselves inside the PM. However, increasing the pore diameters goes against increasing the surface area: a balance between both would need to be reached. Although limiting fouling should take more importance over increasing specific surface area, as large increase in surface temperature can occur due to fouling, as demonstrated in [30]. The minimum passage cross-section to prevent fouling has not been studied and is thus unknown. In the design presented in this chapter the pore size was limited by the computational power available, as explained later in section 9.2.

9.1.4 Repeatability and ease of manufacturing

Pore structures must be limited to well defined and repeatable shapes, eliminating vagarious structures such as the ones found in metal foams. Depending on the manufacturing method, the arm and node diameters would be limited by the resolution of the printing machine used, to ensure the parts are manufacturable. The material used for the PM will also dictate which manufacturing method can be used, which may prove difficult for ceramic based PM. Most metals should be able to be produced using AM.

9.1.5 Porous structure selection

The tetrahedral shape was chosen as the tentative prototype for a profiled PM CAD as it has the possibility of fulfilling all four aforementioned geometrical criteria. Profile ID 2 is the profiled PM on which the CAD presented below is based on, as it offered good CFE_M protection as show in Figure 7.4 and Figure 8.8. The dimensions of the proposed CAD are the same as the ones used in the experiments of chapter 4, 7.5 cm x 1.3 cm x 2.5 cm (L x t x W). This would allow the CFE_M of the sample to be measured using the same methodology presented in chapter 4.

9.2 Profiled Porous Media CAD Methodology

Starting with the base tetrahedral shape shown in Figure 9.1, the first parameter that needs to be set is the distance between the center of the node to the end of the arms. Adjusting this length varies the PPI of the final PM. In the example here this length is set to 0.3 mm, eventually resulting in approximatively 25 PPI. Larger PPI are desirable to increase specific surface area, however, significant computational power is required to model CAD structures with many small parts, the final assembly presented here had approximately 100,000 parts. As this design was created on a home computer, with albeit decent computational power, the PPI was limited to 25 as it enables the demonstration of the methodology while remaining manageable for the computer. Base tetrahedral pore structures can then be assembled into what will be called unit cells, as seen in Figure 9.2, forming a hexagonal prism and the base to build the PM.

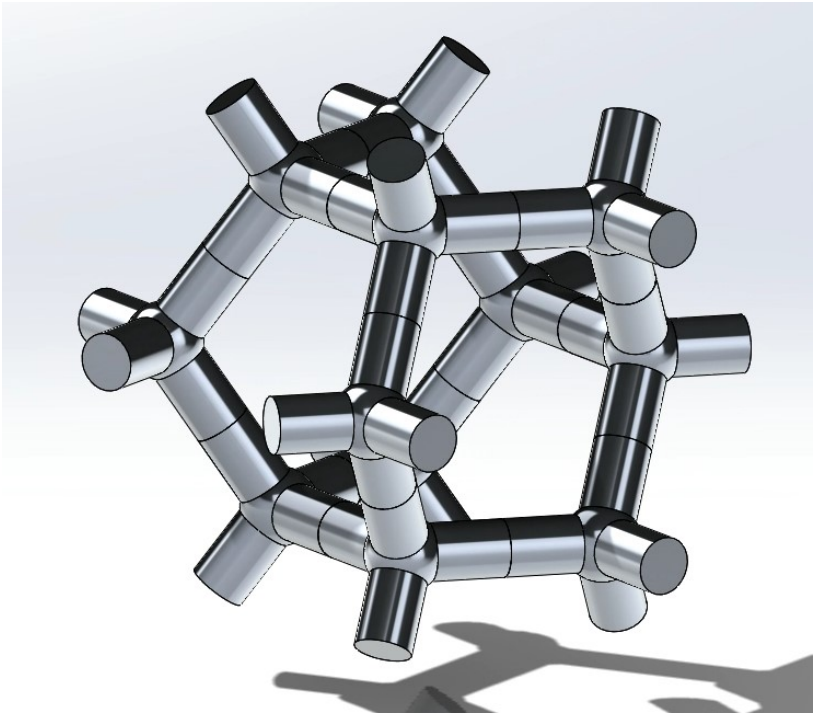

Figure 9.2 Tetrahedral unit cell for profiled PM CAD. Made using SolidWorks 2019.

This unit cell is repeatable and can be further assembled to form structured PM with clear flow paths, however, to achieve higher resistances, a staggered approach is adopted and presented in Figure 9.3. The assembly of the staggered approach finalizes a layer of the PM,

with a thickness of approximately 2.5 mm in this case. For samples of 75 mm this layer thickness corresponds to 32 layers.

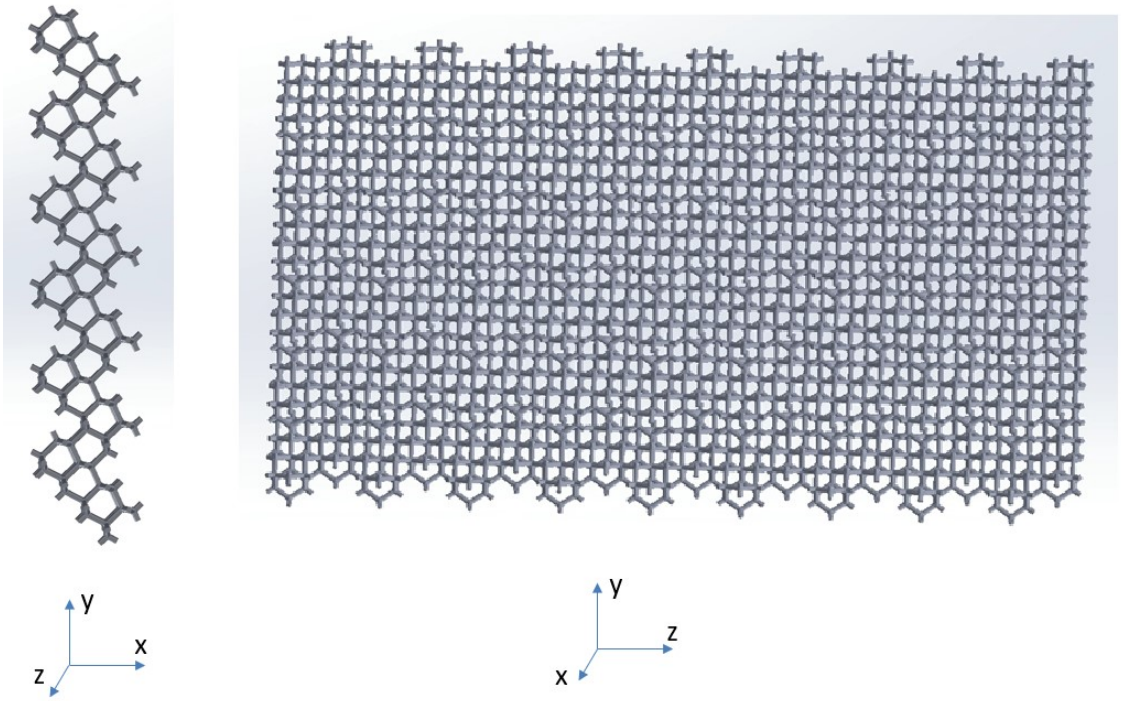

Figure 9.3 Staggered assembly of unit cells, forming a single layer of the PM. Made using SolidWorks 2019.

As mentioned previously, the diameter of the base tetrahedral shape of each layer can be modified to increase or decrease the porosity, thus, the resistance of individual layers. This can be matched to a desired resistance profile and assembled to form the PM. After assembly of all the layers, the edges of the PM are cut to offer a rectangular shape of the desired dimensions, as presented in Figure 9.4.

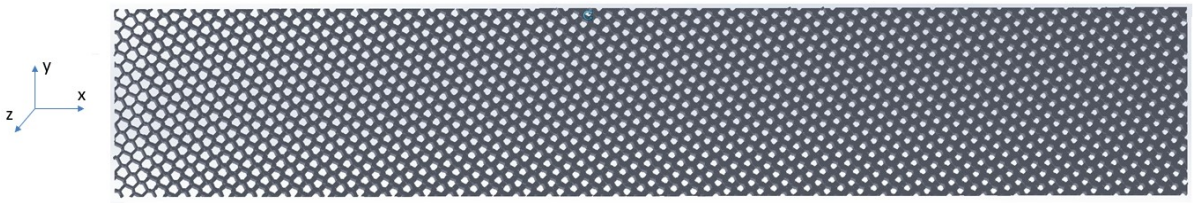

Figure 9.4 Full profiled PM CAD based on the profile ID 2 parameters. Made using SolidWorks 2019.

As the permeability and inertia coefficient relations are unknown at this time for this structure, the porosity of the layers was matched to the porosity profile of profile ID 2. Porosity

was determined in the CAD by dividing the volume the solid unit cell occupies by the estimated square volume created by the unit cell, approximately 4 mm^3 in the case presented so far. This equates to a porosity of approximatively 94% for the first layer and 60% for the final layer.

9.2.1 Profiled porous media properties using tetrahedral base shape

Since a repeatable shape would be used to produce the profiled PM, accurate empirical equations relating the porosity of a layer to the resulting permeability and inertia coefficient is possible. This could be achieved experimentally, by manufacturing multiple samples of single porosities, measuring their permeability and inertia coefficient, and relating them to porosity. Alternatively, numerical investigations of permeability and inertia coefficient of unit cells with different porosities could achieve a similar outcome. It was found in [77] that numerical simulations from microtomography of 3D printed samples can correctly estimate the real permeability of given porous medium.

10 Conclusion

The experimental work performed by Mr. Kivanc Yildiz as part of an undergraduate Thesis submitted April 2019 [12], investigated transpiration cooling as a potential replacement to multi-hole effusion cooling in gas turbine combustion liners. Comparisons to multi-hole effusion cooling revealed transpiration cooling can result in over threefold reduction in the overall surface heat transfer to the porous media. When the cooling holes/open pore areas are excluded, transpiration cooling was found to offer approximately 40% higher cooling film effectiveness (mass analogy) on average, compared to multi-hole effusion cooling, at low coolant flow rates. The advantages of transpiration cooling are more pronounced at high coolant flow rates with over 200% improvement in cooling film effectiveness (mass analogy) due to film lift-off in multi-hole effusion cooling.

Numerical simulations of the experiments using Ansys Fluent was performed and achieved good agreement. Analysis of the flow behavior inside the porous samples showed uneven distribution and lateral movement of coolant. This was attributed to low resistance to flow movement, characterized by a relatively large permeability and small inertia coefficient in the Darcy-Forchheimer momentum equation. A sensitivity study of these two parameters demonstrated a large effect on the resulting coolant distribution and cooling film effectiveness (mass analogy). Higher resistance to flow movement distributes coolant evenly throughout the sample and suppresses lateral movement.

Improvements in uniformity of cooling film effectiveness (mass analogy) was achieved by using the knowledge gained from the sensitivity analysis to design profiled porous media which distribute coolant as desired. These profiled porous media used a square root function to define and adjust the porosity, permeability, and inertia coefficient between the leading and trailing edge. Samples with a square-root profile function were observed to exhibit better results than linear profile function. This permits lower resistance to flow movement in the first half of the sample versus the second half.

Low cooling film effectiveness (mass analogy) remained an issue at the leading edge of the samples. Three solutions were proposed where adding an injection slit prior to the porous media achieved the best results. Another method which achieved good results used a low resistance sample for a small section at the leading edge, followed by a higher overall resistance profiled porous media.

Investigation on the effects of the dimensions of the profiled porous media on cooling film effectiveness (mass analogy) was performed. It was found that increasing the length increases the overall cooling film effectiveness (mass analogy) and induces more coolant to exit the trailing edge due to longer surface resistance, discouraging leading edge transpiration. Increasing the thickness transpired considerably more coolant at the leading edge and less at the trailing edge, resulting in high initial cooling film effectiveness (mass analogy) which reduced over the length of the sample. Increasing both dimensions accomplished a combination of both effects. Therefore, to maintain a cooling film effectiveness (mass analogy) curve when increasing the length of a sample, the profile resistance ratio needs to be increased slightly and increasing the thickness requires decreasing the resistance ratio.

A heat transfer model was validated using experimental data from the literature, which was then used to simulate various porous media seen in previous chapters. The high porosity aluminum metal foam showed the lowest thermal protection, as expected, due to uneven distribution of coolant and poor coolant heat capacity utilization. Compressed foams improved the protection as coolant is distributed more evenly, enabling efficient use of coolant heat capacity and reduction in surface fluid temperature. Profiled porous media with no leading-edge solution offered slight improvement over the compressed foam. The benefit of profiling porous media to reduce the temperature disparity between the leading and trailing edge is diminished when using a material with high heat transfer conductivity. They may be better suited for materials with low thermal conductivity such as ceramics, e.g., if a two-layer porous media was adopted with a ceramic in contact with the hot gas flow, the metal porous media below can be designed to direct coolant optimally and reduce temperature difference between leading and trailing edges of the ceramic. Profiled porous media with removed/replaced leading edge solution offered worse thermal protection than regular profiled samples, largely

attributed to less efficient use of coolant heat capacity as it is mostly transpired at the leading edge to decrease surface fluid temperature.

It was revealed that the cooling film effectiveness (mass analogy) significantly underestimates the cooling film effectiveness (thermal). This is due to the assumption made with the mass analogy method that the wall temperature of the porous media equals the temperature of the cooling film. This is simply not the case under heat transfer conditions due to conduction away from the wall and into the porous media and convection between the ligaments and the coolant inside the porous media, allowing the surface wall of the porous media to be significantly cooler than the cooling film temperature. Still, the cooling film effectiveness (mass analogy) and cooling film effectiveness (thermal) curves follow a similar trend, for example: if the leading edge of the cooling film effectiveness (mass analogy) is lower than the trailing edge value, then cooling film effectiveness (thermal) also has a lower leading-edge value than at the trailing edge. Therefore, it is still a good tool to help predict and design in transpiration cooling, but other important factors must be considered, such as: the conduction of the material, available heat absorption of the coolant, geometry of the porous media, etc.

It was found that reducing the volumetric heat transfer coefficient of the samples resulted in lower surface porous media temperatures. This was attributed to small hot gas penetration into the porous media which transferred more heat than the convection on the surface as the volumetric heat transfer coefficient h_v is orders of magnitude larger than the surface heat transfer coefficient h_s. However, it is unclear if the model correctly predicts the hot gas penetration, as penetration was measured to be less in higher resistance porous media but was not the case in simulations performed in this study [36]. Thus, the findings on this subject are not definitive.

Finally, a proposed method to create CAD models of profiled porous media for production using AM was made based on four criteria: structural integrity, high specific surface area, limited possibility of fouling, and repeatability and ease of manufacturing. Tetrahedral nodes were chosen due to their strong structure and capability to be assembled in a way to satisfy the other three criteria. Estimated porosity was used to relate resistance to flow movement. A CAD

model based on profile ID 2 was created which could later be used to validate the method and cooling film effectiveness (mass analogy) predictions performed numerically in Chapter 7.

10.1 Future work

While it was demonstrated numerically that profiled porous media can achieve uniform cooling film effectiveness (mass analogy), many aspects remain to be investigated and proven experimentally. Proposed CAD models can offer the possibility of studying these. Further studies which could be undertaken are listed below in no particular order:

1. Experimentally measure the cooling film effectiveness (mass analogy) using PSP of profiled porous media manufactured using AM and compare to predicted numerical results.
2. Use AM to produce profiled porous media and compare to other possible CAD models based on the design criteria listed in Chapter 9.
3. Study profiled porous media potential application in two-layer transpiration cooling.
4. Investigate the tensile strength of the designed porous media to determine the maximum porosity which can safely be used for gas turbine combustion liners.
5. Further investigate the flow penetration observed in Chapter 8, determining whether the effect found in this study is physical or purely numerical.
6. Investigate the effects of the BR on the cooling film effectiveness (mass analogy) of designed porous media.
7. Investigate porous media samples with tapered geometry as a mean of modifying the cooling film effectiveness (mass analogy).

References

[1] "Fossil and Alternative Fuels - Energy Content." https://www.engineeringtoolbox.com/fossil-fuels-energy-content-d_1298.html (accessed Jan. 11, 2021).

[2] A. Ulvestad, "A Brief Review of Current Lithium Ion Battery Technology and Potential Solid State Battery Technologies," Mar. 2018. [Online]. Available: http://arxiv.org/abs/1803.04317.

[3] G. E. Andrews and A. Asere, "Transpiration Cooling of Gas Turbine Combustion Chamber Walls," 1984.

[4] J. H. Wang, J. Messner, and M. V Casey, "Performance Investigation of Film and Transpiration Cooling," in *Turbo Expo: Power for Land, Sea, and Air*, Jan. 2004, pp. 895–907, doi: 10.1115/GT2004-54132.

[5] D. W. BAHR, *GAS TURBINE COMBUSTION—Alternative Fuels and Emissions*, Third Edit., vol. 132, no. 11. New York, NY: CRC Press, 2010.

[6] J. Linn and M. J. Kloker, "Effects of wall-temperature conditions on effusion cooling in a Mach-2.67 boundary layer," *AIAA J.*, vol. 49, no. 2, pp. 299–307, 2011, doi: 10.2514/1.J050383.

[7] G. E. Andrews, A. A. Asere, M. C. Mkpadi, and A. Tirmahi, "Transpiration Cooling: Contribution of Film Cooling to the Overall Cooling Effectiveness," *Int. J. Turbo Jet Engines*, vol. 3, no. 2–3, pp. 245–256, Jan. 1986, doi: 10.1515/TJJ.1986.3.2-3.245.

[8] R. Krewinkel, "A review of gas turbine effusion cooling studies," *Int. J. Heat Mass Transf.*, vol. 66, pp. 706–722, Nov. 2013, doi: 10.1016/j.ijheatmasstransfer.2013.07.071.

[9] Y. Sung, A. L. Dord, G. M. Laskowski, L. Shunn, G. Natsui, and J. Kapat, "Detailed Large Eddy Simulations (LES) of Multi-Hole Effusion Cooling Flow for Gas Turbines," in *Turbo Expo: Power for Land, Sea, and Air*, Jun. 2016, pp. 1–9, doi: 10.1115/GT2016-57957.

[10] C. Soares, "Gas Turbine Major Components and Modules," in *Gas Turbines*, Elsevier, 2015, pp. 173–254.

[11] M. Kilic, "A numerical analysis of transpiration cooling as an air cooling mechanism," *Heat Mass Transf. und Stoffuebertragung*, vol. 54, no. 12, pp. 3647–3662, 2018, doi: 10.1007/s00231-018-2391-6.

[12] K. Yildiz, "Investigation of Porous Media Effusive Cooling Efficiency By Means of Pressure Sensitive Paint Analysis," University of Ottawa.

[13] J. Van Wylen, E. Sonntag, and P. Desrochers, *Thermodynamique Appliqué*, 2nd ed. Montréal: John Wiley & Sons Inc., 1992.

[14] R. S. Bunker, "Evolution of turbine cooling," *Proc. ASME Turbo Expo*, vol. 1, pp. 1–26, 2017, doi: 10.1115/GT2017-63205.

[15] K. G., "Future Aero Engine Designs: An Evolving Vision," in *Advances in Gas Turbine Technology*, no. June, InTech, 2011.

[16] G. Cerri, A. Giovannelli, L. Battisti, and R. Fedrizzi, "Advances in effusive cooling techniques of gas turbines," *Appl. Therm. Eng.*, vol. 27, no. 4, pp. 692–698, Mar. 2007, doi: 10.1016/j.applthermaleng.2006.10.012.

[17] R. L. Ecuyer and R. S. Colladay, “Influence of Porous-Wall Thermal Effectiveness on Turbulent-Boundary -Layer Heat Transfer,” *Nasa Tech. Note*, vol. Nasa TN D-, 1972.

[18] E. R. . Eckert and J. N. B. Livingood, “Comparison of Effectiveness of Convection-, Transpiration-, and Film-Cooling Methods with Air as Coolant,” Cleveland, Ohio, 1954.

[19] A. V. Luikov, “Heat and mass transfer with transpiration cooling,” *Int. J. Heat Mass Transf.*, vol. 6, no. 7, pp. 559–570, 1963, doi: 10.1016/0017-9310(63)90013-9.

[20] J. Librizzi and R. J. Cresci, “Transpiration cooling of a turbulent boundary layer in an axisymmetric nozzle,” *AIAA J.*, vol. 2, no. 4, pp. 617–624, 1964, doi: 10.2514/3.2397.

[21] T. E. WALTON, B. RASHIS, and C. W. WINTERS, “Free-flight investigations of subliming ablators and transpiration cooling at hypersonic velocities,” *J. Spacecr. Rockets*, vol. 1, no. 5, pp. 498–501, Sep. 1964, doi: 10.2514/3.27687.

[22] S. Lombardo, S. L. Moskowitz, and S. A. Schnure, “Experimental results of a transpiration-cooled turbine operated in an engine for 150 hours at 2500 F turbine inlet temperature,” *Proc. ASME Turbo Expo*, vol. 1A, 1967, doi: 10.1115/67-GT-29.

[23] N. Christopher, J. M. F. Peter, M. J. Kloker, and J. P. Hickey, “DNS of turbulent flat-plate flow with transpiration cooling,” *Int. J. Heat Mass Transf.*, vol. 157, 2020, doi: 10.1016/j.ijheatmasstransfer.2020.119972.

[24] H. S. Mickley, “Heat, mass, and momentum transfer for flow over a flat plate with blowing or suction,” 1954.

[25] W. D. Rannie, L. G. Dunn, and C. B. Millikan, “A simplified theory of porous wall cooling,” Pasadena, CA, 1947. [Online]. Available: http://hdl.handle.net/2014/45706.

[26] J. Friedman, “A theoretical and experimental investigation of rocket-motor sweat cooling,” *Jour. Am. Rocket Soc*, no. 79, pp. 147–154, 1949.

[27] Y. H. Andoh and B. Lips, “Prediction of porous walls thermal protection by effusion or transpiration cooling. An analytical approach,” *Appl. Therm. Eng.*, vol. 23, no. 15, pp. 1947–1958, Oct. 2003, doi: 10.1016/S1359-4311(03)00145-5.

[28] J. Von Wolfersdorf, “Effect of coolant side heat transfer on transpiration cooling,” *Heat Mass Transf. und Stoffuebertragung*, vol. 41, no. 4, pp. 327–337, 2005, doi: 10.1007/s00231-004-0549-x.

[29] J. Shi and J. Wang, “Optimized structure of two layered porous media with genetic algorithm for transpiration cooling,” *Int. J. Therm. Sci.*, vol. 47, no. 12, pp. 1595–1601, 2008, doi: 10.1016/j.ijthermalsci.2008.01.010.

[30] Y. Q. Liu, Y. Bin Xiong, P. X. Jiang, Y. P. Wang, and J. G. Sun, “Effects of local geometry and boundary condition variations on transpiration cooling,” *Int. J. Heat Mass Transf.*, vol. 62, no. 1, pp. 362–372, 2013, doi: 10.1016/j.ijheatmasstransfer.2013.02.075.

[31] W. Dahmen, T. Gotzen, S. Müller, and M. Rom, “Numerical simulation of transpiration cooling through porous material,” *Int. J. Numer. Methods Fluids*, vol. 76, no. 6, pp. 331–365, Oct. 2014, doi: 10.1002/fld.3935.

[32] W. Dahmen, S. Müller, M. Rom, S. Schweikert, M. Selzer, and J. von Wolfersdorf, “Numerical boundary layer investigations of transpiration-cooled turbulent channel flow,” *Int. J. Heat Mass Transf.*, vol. 86, no. 86, pp. 90–100, Jul. 2015, doi: 10.1016/j.ijheatmasstransfer.2015.02.075.

[33] G. Huang, Y. Zhu, Z. Y. Liao, Z. Huang, and P. X. Jiang, “Transpiration cooling with bio-inspired structured surfaces,” *Bioinspiration and Biomimetics*, vol. 15, no. 3, 2020, doi: 10.1088/1748-3190/ab6bdf.

[34] X. Xiao, G. Zhao, W. Zhou, and S. Martynenko, “Large-eddy simulation of transpiration cooling in turbulent channel with porous wall,” *Appl. Therm. Eng.*, vol. 145, no. May, pp. 618–629, 2018, doi: 10.1016/j.applthermaleng.2018.09.056.

[35] C. Efstathiou and M. Luhar, “Mean turbulence statistics in boundary layers over high-porosity foams,” *J. Fluid Mech.*, vol. 841, pp. 351–379, 2018, doi: 10.1017/jfm.2018.57.

[36] S. A. Showkat Ali, M. Azarpeyvand, M. Szoke, and C. R. Ilário Da Silva, “Boundary layer flow interaction with a permeable wall,” *Phys. Fluids*, vol. 30, no. 8, 2018, doi: 10.1063/1.5043276.

[37] T. Furumoto *et al.*, “Permeability and strength of a porous metal structure fabricated by additive manufacturing,” *J. Mater. Process. Technol.*, vol. 219, pp. 10–16, 2015, doi: 10.1016/j.jmatprotec.2014.11.043.

[38] Z. Min, G. Huang, S. N. Parbat, L. Yang, and M. K. Chyu, “Experimental investigation on additively manufactured transpiration and film cooling structures,” *J. Turbomach.*, vol. 141, no. 3, pp. 1–10, 2019, doi: 10.1115/1.4042009.

[39] G. Huang, Z. Min, L. Yang, P.-X. Jiang, and M. Chyu, “Transpiration cooling for additive manufactured porous plates with partition walls,” *Int. J. Heat Mass Transf.*, vol. 124, pp. 1076–1087, Sep. 2018, doi: 10.1016/j.ijheatmasstransfer.2018.03.110.

[40] C. Fee, S. Nawada, and S. Dimartino, “3D printed porous media columns with fine control of column packing morphology,” *J. Chromatogr. A*, vol. 1333, pp. 18–24, 2014, doi: 10.1016/j.chroma.2014.01.043.

[41] S. Nawada, S. Dimartino, and C. Fee, “Dispersion behavior of 3D-printed columns with homogeneous microstructures comprising differing element shapes,” *Chem. Eng. Sci.*, vol. 164, pp. 90–98, 2017, doi: 10.1016/j.ces.2017.02.012.

[42] B. Munro, S. Becker, M. F. Uth, N. Preußer, and H. Herwig, “Fabrication and Characterization of Deformable Porous Matrices with Controlled Pore Characteristics,” *Transp. Porous Media*, vol. 107, no. 1, pp. 79–94, 2015, doi: 10.1007/s11242-014-0426-0.

[43] K. K. Wong and K. C. Leong, “Saturated pool boiling enhancement using porous lattice structures produced by Selective Laser Melting,” *Int. J. Heat Mass Transf.*, vol. 121, pp. 46–63, 2018, doi: 10.1016/j.ijheatmasstransfer.2017.12.148.

[44] D. A. Nield and A. Bejan, *Convection in Porous Media*, Fifth Edit. Cham, Switzerland: Springer International Publishing, 2017.

[45] H. J. Xu, L. Gong, C. Y. Zhao, Y. H. Yang, and Z. G. Xu, “Analytical considerations of local thermal non-equilibrium conditions for thermal transport in metal foams,” *Int. J. Therm. Sci.*, vol. 95, no.

February, pp. 73–87, 2015, doi: 10.1016/j.ijthermalsci.2015.04.007.

[46] A. Bhattacharya, V. V. Calmidi, and R. L. Mahajan, “Thermophysical properties of high porosity metal foams,” *Int. J. Heat Mass Transf.*, vol. 45, no. 5, pp. 1017–1031, Feb. 2002, doi: 10.1016/S0017-9310(01)00220-4.

[47] V. V. Calmidi and R. L. Mahajan, “Forced convection in high porosity metal foams,” *J. Heat Transfer*, vol. 122, no. 3, pp. 557–565, 2000, doi: 10.1115/1.1287793.

[48] N. Dukhan, R. Picón-Feliciano, and Á. R. Álvarez-Hernández, “Air Flow Through Compressed and Uncompressed Aluminum Foam: Measurements and Correlations,” *J. Fluids Eng.*, vol. 128, no. 5, pp. 1004–1012, Sep. 2006, doi: 10.1115/1.2236132.

[49] B. D. Wood, X. He, and S. V. Apte, “Modeling Turbulent Flows in Porous Media,” *Annu. Rev. Fluid Mech.*, vol. 52, pp. 171–203, 2020, doi: 10.1146/annurev-fluid-010719-060317.

[50] M. Hinse, P. Richer, B. Jodoin, K. Yildiz, S. Yun, and Z. Hong, “Numerical and Experimental Studies of Transpiration Cooling Film Effectiveness Over Porous Materials,” in *AIAA Propulsion and Energy*, 2020, pp. 1–20.

[51] Z. Lei, A. Mahallati, M. Cunningham, and P. Germain, “Influence of Inlet Swirl on the Aerodynamics of a Model Turbofan Lobed Mixer,” in *International Mechanical Engineering Congress and Exposition*, Jan. 2010, pp. 807–819, doi: 10.1115/IMECE2010-39116.

[52] Y.-Q. Liu, P.-X. Jiang, Y.-B. Xiong, and Y.-P. Wang, “Experimental and numerical investigation of transpiration cooling for sintered porous flat plates,” *Appl. Therm. Eng.*, vol. 50, no. 1, pp. 997–1007, Jan. 2013, doi: 10.1016/j.applthermaleng.2012.08.028.

[53] A. Andreini, B. Facchini, A. Picchi, L. Tarchi, and F. Turrini, “Experimental and Theoretical Investigation of Thermal Effectiveness in Multiperforated Plates for Combustor Liner Effusion Cooling,” *J. Turbomach.*, vol. 136, no. 9, p. 91003, Sep. 2014, doi: 10.1115/1.4026846.

[54] G. Wang, G. Ledezma, J. DeLancey, and A. Wang, “Experimental Study of Effusion Cooling With Pressure-Sensitive Paint,” *J. Eng. Gas Turbines Power*, vol. 139, no. 5, May 2017, doi: 10.1115/1.4034943.

[55] S. Schweikert, J. Von Wolfersdorf, M. Selzer, and H. Hald, “Experimental Investigation on Velocity and Temperature Distributions of Turbulent Cross Flows over Transpiration Cooled C / C Wall Segments,” in *5TH EUROPEAN CONFERENCE FOR AERONAUTICS AND SPACE SCIENCES*, 2013, pp. 1–12.

[56] “Turbulence intensity -- CFD-Wiki, the free CFD reference.” https://www.cfd-online.com/Wiki/Turbulence_intensity (accessed Feb. 10, 2021).

[57] “ANSYS FLUENT 12.0/12.1 Documentation.” https://www.afs.enea.it/project/neptunius/docs/fluent/index.htm (accessed Dec. 30, 2020).

[58] “ANSYS FLUENT 12.0 User’s Guide - 8.9.5 Mass Diffusion Coefficient Inputs for Turbulent Flow.” https://www.afs.enea.it/project/neptunius/docs/fluent/html/ug/node323.htm (accessed Mar. 16, 2021).

[59] W. Dahmen, V. König, S. Müller, and M. Rom, “Numerical investigation of transpiration cooling with uniformly and non-uniformly simulated injection,” 2017, doi: https://doi.org/10.13009/EUCASS2017-

476.

[60] “ANSYS FLUENT 12.0 User’s Guide - 7.2.3 Porous Media Conditions.” https://www.afs.enea.it/project/neptunius/docs/fluent/html/ug/node233.htm (accessed Jul. 13, 2020).

[61] K. Boomsma, D. Poulikakos, and Y. Ventikos, “Simulations of flow through open cell metal foams using an idealized periodic cell structure,” *Int. J. Heat Fluid Flow*, vol. 24, no. 6, pp. 825–834, Dec. 2003, doi: 10.1016/j.ijheatfluidflow.2003.08.002.

[62] “✅ Ansys Meshing - Bias Factor Tutorial - CFD.NINJA.” https://cfd.ninja/ansys-meshing/ansys-meshing-bias-factor/ (accessed Jan. 07, 2021).

[63] “ANSYS FLUENT 12.0 User’s Guide - 31.1.3 Facet Values.” https://www.afs.enea.it/project/neptunius/docs/fluent/html/ug/node981.htm (accessed Mar. 17, 2021).

[64] D. Yang, Z. Xue, and S. A. Mathias, “Analysis of Momentum Transfer in a Lid-Driven Cavity Containing a Brinkman–Forchheimer Medium,” *Transp. Porous Media*, vol. 92, no. 1, pp. 101–118, Mar. 2012, doi: 10.1007/s11242-011-9893-8.

[65] A. Bejan, *Convection Heat Transfer*. Hoboken, NJ, USA: John Wiley & Sons, Inc., 2013.

[66] J. G. Fourie and J. P. Du Plessis, “Pressure drop modelling in cellular metallic foams,” *Chem. Eng. Sci.*, vol. 57, no. 14, pp. 2781–2789, 2002, doi: 10.1016/S0009-2509(02)00166-5.

[67] S. Y. Kim, J. W. Paek, and B. H. Kang, “Flow and heat transfer correlations for porous fin in a plate-fin heat exchanger,” *J. Heat Transfer*, vol. 122, no. 3, pp. 572–578, 2000, doi: 10.1115/1.1287170.

[68] S. Y. Kim, B. H. Kang, and J. H. Kim, “Forced convection from aluminum foam materials in an asymmetrically heated channel,” *Int. J. Heat Mass Transf.*, vol. 44, no. 7, pp. 1451–1454, 2001, doi: 10.1016/S0017-9310(00)00187-3.

[69] A. Marafie and K. Vafai, “Analysis of non-Darcian effects on temperature differentials in porous media,” *Int. J. Heat Mass Transf.*, vol. 44, no. 23, pp. 4401–4411, 2001, doi: 10.1016/S0017-9310(01)00099-0.

[70] D. Y. Lee and K. Vafai, “Analytical characterization and conceptual assessment of solid and fluid temperature differentials in porous media,” *Int. J. Heat Mass Transf.*, vol. 42, no. 3, pp. 423–435, 1998, doi: 10.1016/S0017-9310(98)00185-9.

[71] W. H. Shih, W. C. Chiu, and W. H. Hsieh, “Height effect on heat-transfer characteristics of aluminum-foam heat sinks,” *J. Heat Transfer*, vol. 128, no. 6, pp. 530–537, 2006, doi: 10.1115/1.2188461.

[72] R. Xu, Y. Huang, P. Jiang, and B. Wang, “Internal heat transfer coefficients in microporous media with rarefaction effects,” *Sci. China Technol. Sci.*, vol. 55, no. 10, pp. 2869–2876, Oct. 2012, doi: 10.1007/s11431-012-4994-3.

[73] “Carbon-Carbon Composite - online catalogue source - supplier of research materials in small quantities - Goodfellow.” http://www.goodfellow.com/E/Carbon-Carbon-Composite.html (accessed Jan. 15, 2021).

[74] Y. Kuwata and K. Suga, “Direct numerical simulation of turbulence over anisotropic porous media,” *J. Fluid Mech.*, vol. 831, pp. 41–71, 2017, doi: 10.1017/jfm.2017.619.

[75] P. Gzil, J. De Smet, and G. Desmet, “A discussion of the possible ways to improve the performance of silica monoliths using a kinetic plot analysis of experimental and computational plate height data,” *J. Sep.*

Sci., vol. 29, no. 12, pp. 1675–1685, 2006, doi: 10.1002/jssc.200600180.

[76] H. Liu, Q. N. Yu, Z. G. Qu, and R. Z. Yang, "Simulation and analytical validation of forced convection inside open-cell metal foams," *Int. J. Therm. Sci.*, vol. 111, pp. 234–245, 2017, doi: 10.1016/j.ijthermalsci.2016.09.006.

[77] L. C. de S. M. Ozelim and A. L. B. Cavalcante, "Combining Microtomography, 3D Printing, and Numerical Simulations to Study Scale Effects on the Permeability of Porous Media," *Int. J. Geomech.*, vol. 19, no. 2, p. 04018194, 2019, doi: 10.1061/(asce)gm.1943-5622.0001340.

Appendix A - Heat Transfer Analysis

This appendix section shows relevant material concerning the heat transfer analysis of Chapter 8.

Derivation of the heat equation from the first law for a solid control volume.

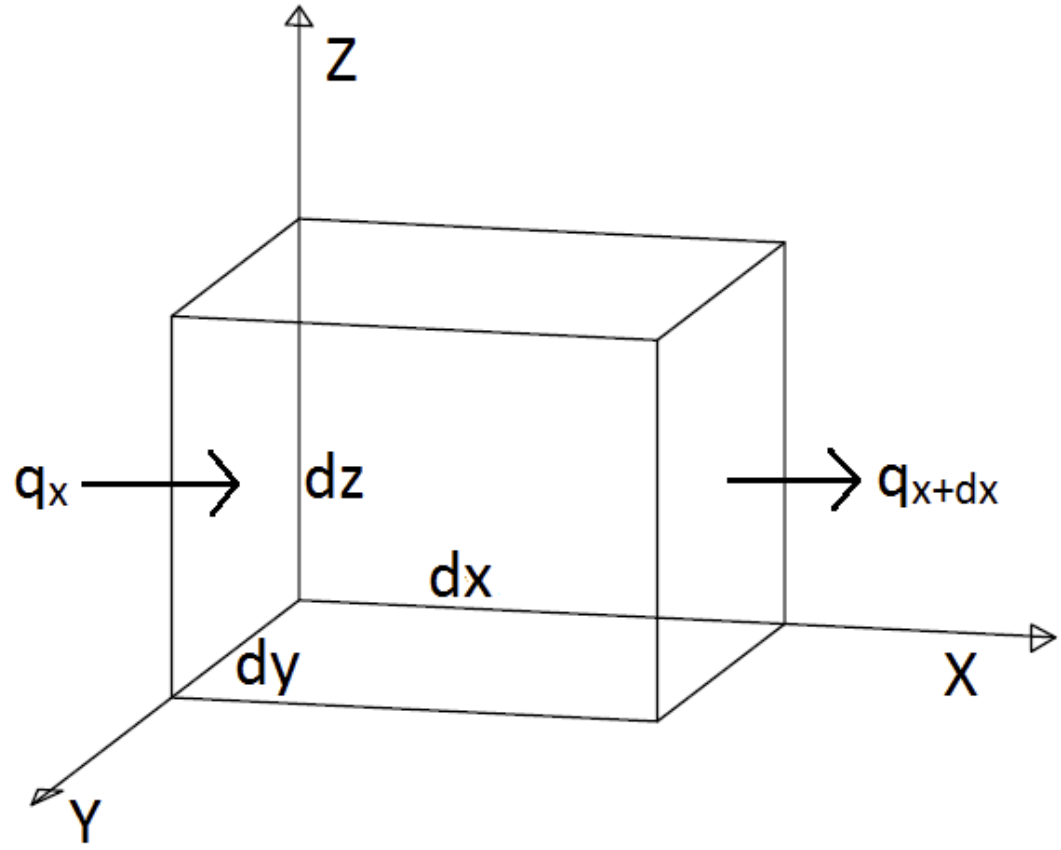

Assumptions:

1. Closed system
2. Transient
3. $\Delta E_p = \Delta E_K = 0$

4. $\dot{W} = 0$
5. Radiation = 0
6. Viscous dissipation = 0
7. Solid phase

Conservation of mass

$$\frac{\cancel{dm_{cv}}}{\cancel{dt}} = \Sigma \dot{m}_e - \Sigma \dot{m}_i \ , \qquad \times dt$$

$$\mathrm{m}_1 = \mathrm{m}_2 = m$$

First Law

$$\dot{Q_{cv}} + \cancel{\Sigma \dot{m}_i \left(h_i + \frac{v_i^2}{2} + g z_i \right)}$$

$$= \cancel{\dot{W} + \Sigma \dot{m}_e \left(h_e + \frac{v_e^2}{2} + g z_e \right)}$$

$$+ \frac{m\left(u_2 + \cancel{\frac{v_2^2}{2} + g z_2}\right) - m\left(u_1 + \cancel{\frac{v_1^2}{2} + g z_1}\right)}{\Delta t}_{cv}$$

$$\Delta Q_{cv} = m \frac{\Delta u}{\Delta t}_{cv}$$

Where u is internal energy.

For solid and liquids [13]

$$\Delta u \ \approx \ \Delta \mathrm{h}$$

Where h is enthalpy.

$$\Delta Q_{cv} = \rho \mathrm{d} \mathrm{V} c_{p,s} \frac{\partial \mathrm{T_s}}{\partial \mathrm{t}}$$

The above equation can be written down in words as follows:

(Rate of heat conduction at x,y,z) – (rate of heat conduction at x + dx, y + dy, z + dz) + (rate of heat generation inside the element) = (rate of change of energy content of the element)

The left side of the equation can be derived as follows:

$$\Delta Q_{cv} = (\dot{q_x} - \dot{q_{x+dx}}) + \left(\dot{q_y} - \dot{q_{y+dy}}\right) + (\dot{q_z} - \dot{q_{z+dz}}) + \dot{E_{gen}}$$

$$\dot{q_x} - \dot{q_{x+dx}} = -\frac{\partial}{\partial x}\left(-k_s(\partial y \cdot dz)\frac{\partial T}{\partial x}\right) \cdot dx$$

$$\dot{q_y} - \dot{q_{y+dy}} = -\frac{\partial}{\partial y}\left(-k_s(\partial x \cdot dz)\frac{\partial T}{\partial y}\right) \cdot dy$$

$$\dot{q_z} - \dot{q_{z+dz}} = -\frac{\partial}{\partial z}\left(-k_s(\partial x \cdot dy)\frac{\partial T}{\partial z}\right) \cdot dz$$

$$\dot{E_{gen}} = A \cdot h_v(T_f - T_s)$$

Divided by dV

$$\frac{\partial}{\partial x}\left(k_s\frac{\partial T_s}{\partial x}\right) + \frac{\partial}{\partial y}\left(k_s\frac{\partial T_s}{\partial y}\right) + \frac{\partial}{\partial z}\left(k_s\frac{\partial T_s}{\partial z}\right) + a_{sf} \cdot h_v(T_f - T_s) = \rho c_{p,s}\frac{\partial T_s}{\partial t}$$

Where a_{sf} is the ration of internal surface area to the total volume of the element and h_v the volumetric convective heat transfer coefficient.

$$\rho c_{p,s}\frac{\partial T_s}{\partial t} = \nabla \cdot (k_s \nabla \cdot T_s) + h_i(T_f - T_s)$$

Due to the element containing both solid and fluid phases, we need to take the portion of each into account thus:

$$(1-\epsilon)\rho c_{p,s}\frac{\partial T_s}{\partial t} = \nabla \cdot (k_{se} \nabla \cdot T_s) + h_i(T_f - T_s)$$

Derivation of the heat equation from the first law for a fluid control volume.

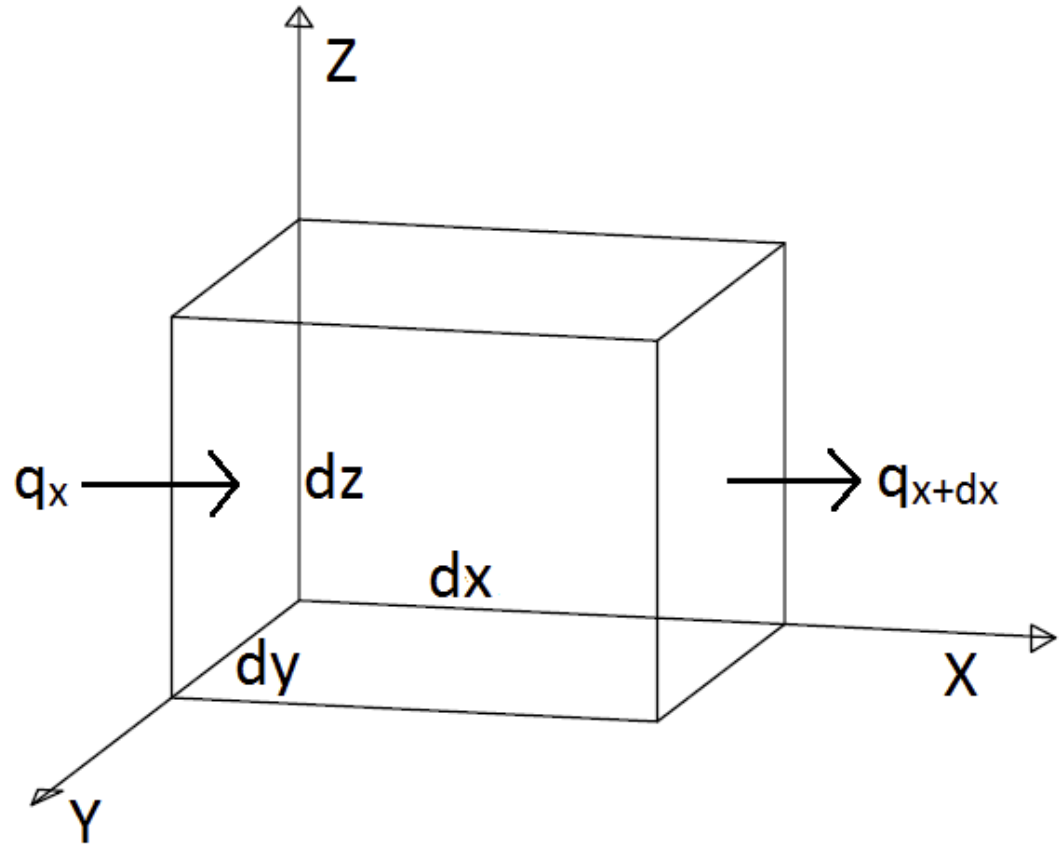

Assumptions:

1. Open system
2. Transient
3. $\Delta E_p = \Delta E_K = 0$
4. $\dot{W} = 0$
5. Radiation = 0
6. Viscous dissipation = 0
7. Fluid phase
8. Ideal gas
9. Negligible compressibility effects

Conservation of mass

$$\frac{\cancel{dm_{cv}}}{\cancel{dt}} = \Sigma\dot{m}_e - \Sigma\dot{m}_\iota \ ,$$

$$\dot{m}_e = \dot{m}_\iota = \dot{m}$$

First Law

$$\dot{Q_{cv}} + \Sigma\dot{m}_\iota \left(h_i + \frac{\cancel{v_\iota^2}}{\cancel{2}} + \cancel{gz_\iota} \right)$$

$$= \cancel{\dot{W}} + \Sigma\dot{m}_e \left(h_e + \frac{\cancel{v_e^2}}{\cancel{2}} + \cancel{gz_e} \right)$$

$$+ \frac{m\left(u_2 + \frac{\cancel{v_2^2}}{\cancel{2}} + \cancel{gz_2} \right) - m\left(u_1 + \frac{\cancel{v_1^2}}{\cancel{2}} + \cancel{gz_1} \right)}{\Delta t}_{cv}$$

$$\Delta Q_{cv} = m\frac{\Delta u}{\Delta t}_{cv} + \dot{m}(h_e - h_i)$$

$$\Delta Q_{cv} = m\frac{\Delta u}{\Delta t}_{cv} + \dot{m}c_{p,f}\left(T_{fe} - T_{fi}\right)$$

$$\Delta Q_{cv} = m\frac{\Delta u}{\Delta t}_{cv} + \rho v dA c_{pf}\left(T_{fe} - T_{fi}\right)$$

For gasses [13]

$$\Delta u \approx \Delta \mathrm{h} - \Delta(P v_m)$$

Where v_m is volume per mass or $\frac{1}{\rho}$, P is pressure.

$$\Delta Q_{cv} = \rho \mathrm{d}\mathrm{V} c_{p,f} \frac{\partial \mathrm{T_f}}{\partial \mathrm{t}} - \cancel{\rho dV} \frac{\cancel{\partial(P v_m)}}{\cancel{\partial t}} + \rho v dA c_{p,f}\left(\Delta T_f\right)$$

The above equation can be written down in words as follows:

(Rate of heat conduction at x,y,z) – (rate of heat conduction at x + dx, y + dy, z + dz) + (rate of heat generation inside the element) = (rate of change of energy content of the element) + (rate heat transport through the element from convection)

The left side of the equation can be derived as follows:

$$\Delta Q_{cv} = (\dot{q_x} - \dot{q_{x+dx}}) + (\dot{q_y} - \dot{q_{y+dy}}) + (\dot{q_z} - \dot{q_{z+dz}}) + \dot{E_{gen}}$$

$$\dot{q_x} - \dot{q_{x+dx}} = -\frac{\partial}{\partial x}\left(-k_s(\partial y \cdot dz)\frac{\partial T}{\partial x}\right) \cdot dx$$

$$\dot{q_y} - \dot{q_{y+dy}} = -\frac{\partial}{\partial y}\left(-k_s(\partial x \cdot dz)\frac{\partial T}{\partial y}\right) \cdot dy$$

$$\dot{q_z} - \dot{q_{z+dz}} = -\frac{\partial}{\partial z}\left(-k_s(\partial x \cdot dy)\frac{\partial T}{\partial z}\right) \cdot dz$$

$$\dot{E_{gen}} = A \cdot h_v(T_s - T_f)$$

Divided by dV

$$\frac{\partial}{\partial x}\left(k_s\frac{\partial T_f}{\partial x}\right) + \frac{\partial}{\partial y}\left(k_s\frac{\partial T_f}{\partial y}\right) + \frac{\partial}{\partial z}\left(k_s\frac{\partial T_f}{\partial z}\right) + a_{sf} \cdot h_v(T_s - T_f) = \rho c_{p,f}\frac{\partial T_f}{\partial t} + \rho v\frac{dA}{dV}dT_f$$

$$\frac{dA}{dV}dT_f = \frac{\cancel{dydz}dT_f}{dx\cancel{dydz}} + \frac{\cancel{dxdz}dT_f}{\cancel{dx}dy\cancel{dz}} + \frac{\cancel{dxdy}dT_f}{\cancel{dxdy}dz}$$

$$\frac{dA}{dV}dT_f = \nabla T_f$$

$$\rho_f c_{p,f}\left(\frac{\partial T_f}{\partial t} + v \cdot \nabla T_f\right) = \nabla \cdot (k_f \nabla \cdot T_f) + h_i(T_s - T_f)$$

Due to the element containing both solid and fluid phase, we need to take the portion of each into account thus:

$$\epsilon\rho c_{p,s}\left(\frac{\partial T_f}{\partial t} + v \cdot \nabla T_f\right) = \nabla \cdot (k_{fe} \nabla \cdot T_f) + h_i(T_s - T_f)$$

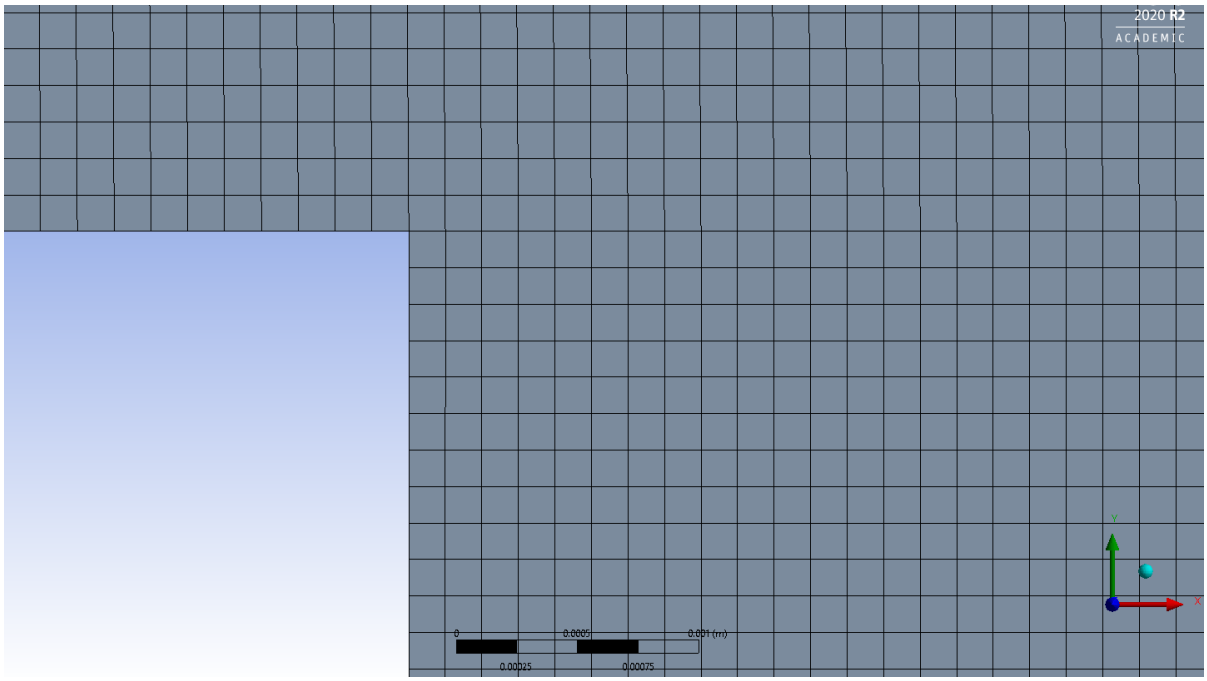

Figure A.1 Mesh around the surface for the heat transfer simulations with element sizes of 0.15mm and no bias applied.

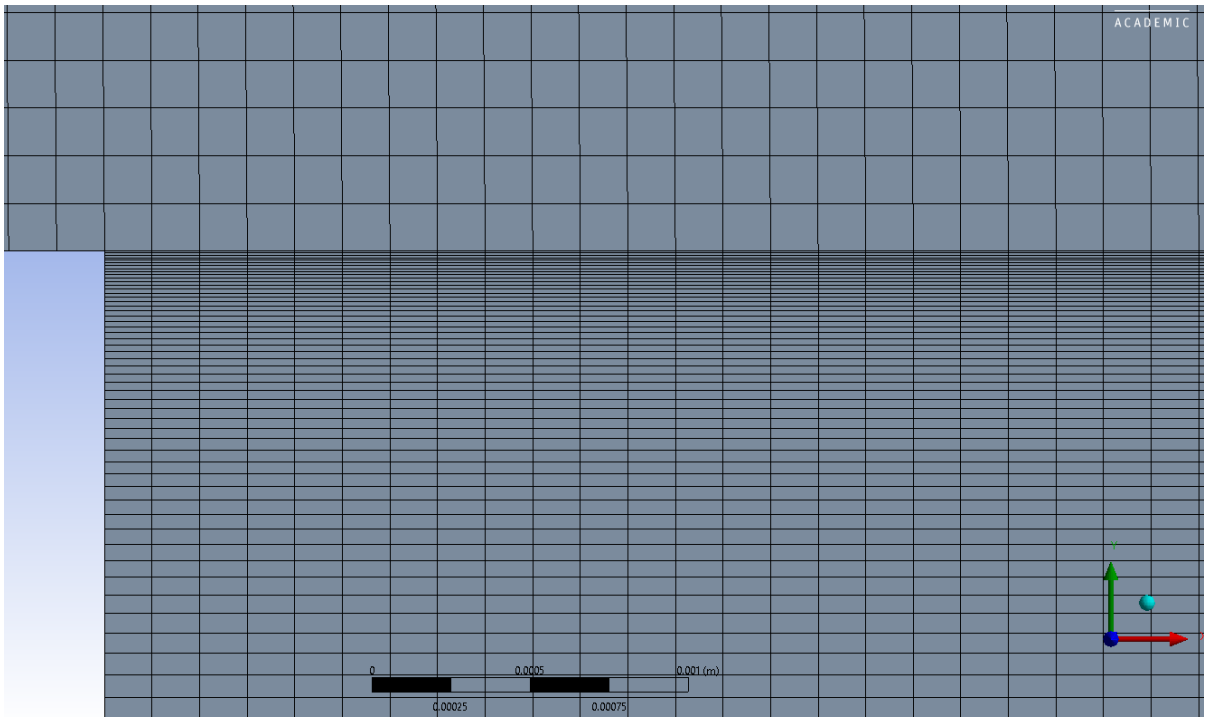

Figure A.2 Mesh around the surface for the heat transfer simulations with element sizes of 0.15mm with bias of 100 applied in the porous media.

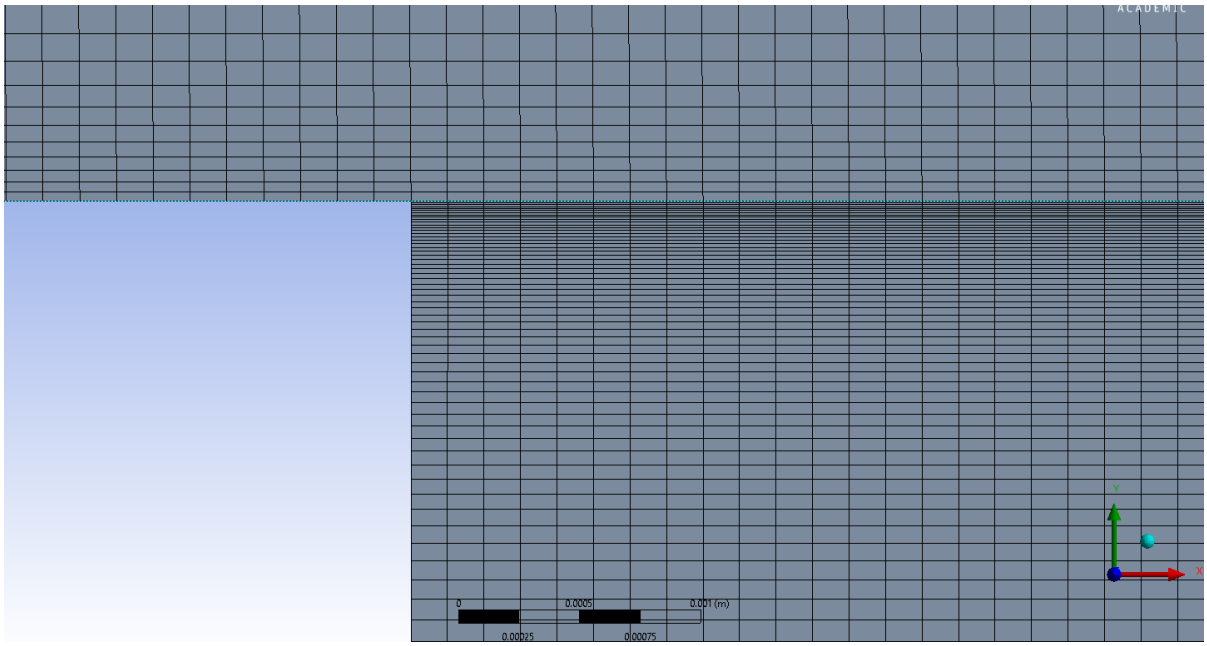

Figure A.3 Mesh around the surface for the heat transfer simulations with element sizes of 0.15mm with bias of 100 applied in the porous media and 10 above.

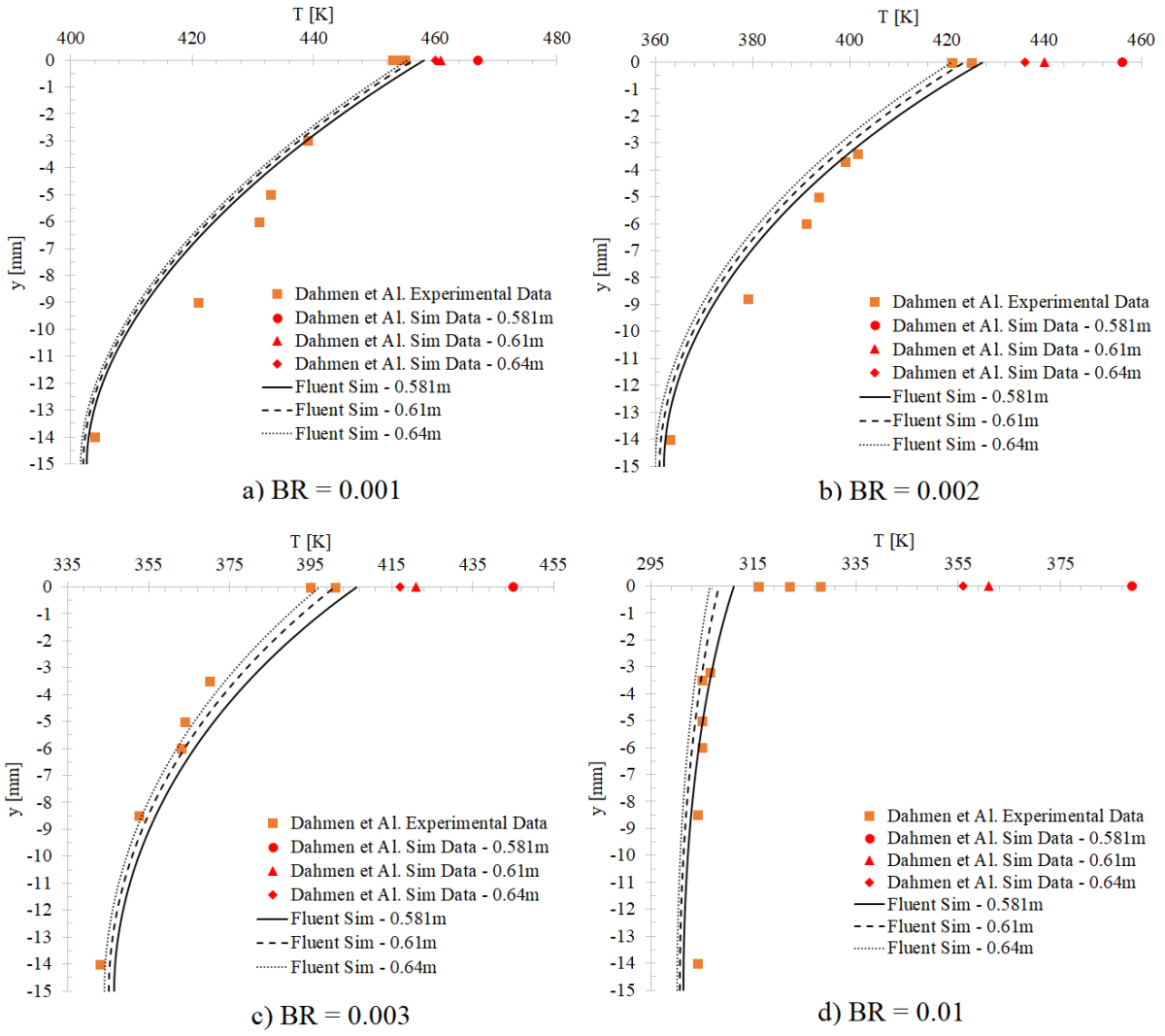

Figure A.4 Porous media temperature distribution between Fluent simulations with surface simulation and experimental data from [31] **at four different BR. Fluent simulations used equation (8-13) to estimate hot gas convective heat transfer coefficient.**

Convective coefficient calculation for zero blowing condition of the validation model in subsection 8.2:

Table A-1 Validation simulation values for computing zero blowing convection coefficient of air.

Density, $\boldsymbol{\rho}$	$\mathbf{0.65}\frac{\boldsymbol{kg}}{\boldsymbol{m^3}}$
Specific heat, $\boldsymbol{c_p}$ *at* $\mathbf{500}\boldsymbol{K}$	$1031\frac{J}{kg \cdot K}$
Velocity, $\boldsymbol{v}$	$224.11\frac{m}{s}$
Dynamic viscosity, $\boldsymbol{\mu}$ *at* $\mathbf{500}\boldsymbol{K}$	$26.72E^{-6}Pa \cdot s$
Static temperature, $\boldsymbol{T_{static}}$	$500K$
Duct dimensions, W x H	0.061 [m] x 0.09 [m]
Hydraulic diameter, $\boldsymbol{D_H}$	0.0727[m]
Prandtl number, $\boldsymbol{Pr}$	0.71

From equation (8-17):

$$Re_D = \frac{\rho v D_H}{\mu} = \frac{0.65 \cdot 224.11 \cdot 0.0727}{26.72E^{-6}} = 396{,}344$$

From (8-18):

$$Nu_D = 0.0214(Re_D^{0.8} - 1)Pr^{0.4} = 0.0214 \cdot (396344^{0.8} - 1) \cdot 0.71^{0.4} = 559.67$$

From (8-20)

$$St_{DH} = St_O = \frac{h_O}{\rho v c_p} = \frac{Nu_{DH}}{Re_{DH} Pr}$$

$$St_{DH} = St_O = \frac{559.64}{396344 \cdot 0.71} = 1.989E^{-3}$$

$$h_O = St_O \rho v c_p = 1.989E^{-3} \cdot 0.65 \cdot 224.11 \cdot 1031 = 298.72\frac{W}{m^2 \cdot K}$$

Convective coefficient calculation for heat transfer simulations of various porous media in section 8.3:

Table A-2 Validation simulation values for computing zero blowing convection coefficient of air.

Density, $\boldsymbol{\rho}$	$\mathbf{0.6969}\frac{\boldsymbol{kg}}{\boldsymbol{m^3}}$
Specific heat, $\boldsymbol{c_p}$ *at* $\mathbf{500}\boldsymbol{K}$	$1031\frac{J}{kg \cdot K}$
Velocity, $\boldsymbol{v}$	$55.77\frac{m}{s}$
Dynamic viscosity, $\boldsymbol{\mu}$ *at* $\mathbf{500}\boldsymbol{K}$	$26.72E^{-6}Pa \cdot s$
Static temperature, $\boldsymbol{T_{static}}$	$500K$
Duct dimensions, W x H	0.1 [m] x 0.1 [m]
Hydraulic diameter, $\boldsymbol{D_H}$	0.1[m]
Prandtl number, $\boldsymbol{Pr}$	0.71

From equation (8-17):

$$Re_D = \frac{\rho v D_H}{\mu} = \frac{0.6969 \cdot 55.77 \cdot 0.1}{26.72E^{-6}} = 145457$$

From (8-19):

$$Nu_D = 0.023 \cdot Re_D^{0.8} Pr^{0.4} = 0.023 \cdot 145457^{0.8} \cdot 0.71^{0.4} = 270.66$$

From (8-20)

$$St_{DH} = St_O = \frac{h_O}{\rho v c_p} = \frac{Nu_{DH}}{Re_{DH} Pr}$$

$$St_{DH} = St_O = \frac{270.33}{145457 \cdot 0.71} = 2.62E^{-3}$$

$$h_O = St_O \rho v c_p = 2.62E^{-3} \cdot 0.6969 \cdot 55.77 \cdot 1031 = 105.05\frac{W}{m^2 \cdot K}$$

Appendix B - Heat Transfer Simulations UDF

```
#include "udf.h"

DEFINE_PROFILE(top_surface_temperature,t,i)
{
  cell_t c0,c1=-1;
  Thread *t0,*t1=NULL;
  int Zone_ID_fluid = 8; /* Fluid zone ID */
  Domain *d = Get_Domain(1);
  Thread *thread_fluid = Lookup_Thread(d,Zone_ID_fluid); /* get the fluid thread on interface of the fluid zone ID given */
  face_t f;
  face_t f_fluid; /* create a face thread for the fluid */



  real f_hg_temp[1500]; /* define a matrix to store cell temperatures (hot gas side)*/
  real f_c_temp[1500]; /* define a matrix to store cell temperatures (cool side or inside the porous media)*/
  int k; /* define a counter */

  k=0;

  begin_f_loop(f,thread_fluid) /* loop over all the face threads of the fluid interface defined before*/
  {
    f_c_temp[k] = C_T(F_C1(f,thread_fluid),THREAD_T1(thread_fluid)); /* Store the cool side cell temperature value */
    f_hg_temp[k] = C_T(F_C0(f,thread_fluid),THREAD_T0(thread_fluid)); /* Store the hot side cell temperature value */
    k++;
  }
  end_f_loop(f,thread_fluid)

  k = 0;

  begin_f_loop(f,t) /* loop over all the faces of the solid interface (top surface of the porous media) */
  {
    F_PROFILE(f,t,i) = f_hg_temp[k]; /* define the value used as the free stream temperature for surface convection at each
cell */
    k++;
  }

  end_f_loop(f,t)
}
```